

First Principles Study of Magnetic Properties of Nanowires on Cu Surfaces

Dissertation

zur Erlangung des
Doktorgrades der Naturwissenschaften (Dr. rer. nat.)

Der
Naturwissenschaftlichen Fakultät II
der Martin-Luther-Universität
Halle-Wittenberg,

vorgelegt

von Herrn Hossein Hashemi
geb. am 31. August 1976 in Arak, Iran

Gutachter:

1. Prof. Dr. Wolfram Hergert (Betreuer)
2. Prof. Dr. Kalevi Kokko
3. PD Dr. Arthur Ernst

Halle (Saale), 27. Januar 2015

Abstract

The objective of this thesis is to investigate structural, electronic and magnetic properties of the one-dimensional (1D) metallic nanostructures on metallic substrate. One-dimensional transition-metal TM nanowires of single atom width can be formed on a stepped Cu(111) surface. The basic template is an embedded Fe chain at one-atom distance away from the upper edge of the monatomic surface step. Chains, consisting of 3d TM atoms from Sc to Ni can be formed on top of the embedded Fe chain. Density functional theory is applied to calculate the magnetic ground state and to describe the magnetic properties of such TM-Fe wires. The wires form different magnetic structures but are all characterized by a high local magnetic moment. Ferromagnetic Mn, Fe, Co, and Ni as well as antiferromagnetic structures Cr might be achieved using the embedded Fe wire near the step as a template. Exchange parameters are extracted from the non-collinear DFT calculations. DFT calculations including spinorbit coupling (SOC) are performed to calculate the magnetic anisotropy energies, including magnetocrystalline and shape anisotropies of TM-Fe wires in both isolated and deposited cases. A classical anisotropic Heisenberg model is used in Monte Carlo simulations to study finite temperature effects.

Contents

1	Introduction	6
2	Theoretical Background	10
2.1	The Many-Body Problem	10
2.2	Born-Oppenheimer Approximation	11
2.3	Hartree-Fock Theory	12
2.4	Density Functional Theory (DFT)	13
2.4.1	The Hohenberg-Kohn Theorems	13
2.4.2	The Kohn-Sham Method	16
2.4.3	The Exchange-Correlation Functionals	18
2.5	Electronic Structure Calculations	19
2.5.1	Plane-Wave Formulation of DFT	19
2.5.2	Augmented Plane Wave (APW) Method	24
2.5.3	Spin Systems	25
2.6	Spin System at finite temperature	27
2.6.1	Classical Heisenberg model	27
2.6.2	Monte Carlo method	27
3	Properties of the Cu substrate	31
3.1	Properties of Cu bulk crystals	31
3.2	Cu(111) surface	33
3.2.1	Surface relaxation	33
3.2.2	Surface energy	34
3.2.3	Work function	36
3.2.4	Surface states	36
4	TM nanowires on Cu surfaces	43
4.1	Experimental and theoretical background	43
4.2	Theoretical method	47
4.2.1	Setup	47
4.3	Isolated TM chains	50
4.4	Free-Standing TM-Fe wires	51
4.5	TM-Fe wires on Cu(111)	53
4.5.1	Structural and magnetic properties	53
5	First-Principles Calculation of Exchange Interactions	62
5.1	Introduction	62

Contents

5.2	Theoretical method	63
5.3	Calculation of direct exchange coupling	64
5.4	Calculation of exchange coupling: long range (RKKY) interactions	69
6	Magnetic Anisotropy Energy	73
6.1	Theoretical method	75
6.2	Spin-orbit coupling and orbital magnetic moment	76
6.3	Magnetic anisotropy energy (MAE)	78
6.4	Magnetism at Finite Temperatures	82

1 Introduction

Dimensionality is one of the most important factors in tailoring the properties of materials. Low-dimensional systems and nanostructures are of particular interest to the theoretical and experimental communities. Such systems require realistic and efficient ways to describe them. The system properties are often determined by quantum effects, which are strongly dependent on the dimension, structure, and elemental composition. Confinement of electrons in low-dimensional systems may also change the electronic and magnetic properties of the system. One-dimensional (1D) systems show unusual physical properties which make the fabrication of such systems a challenge.

These systems exhibit unique electronic structures due to enhanced intra-atomic exchange and decreased coordination number. They reveal an increased tendency towards magnetism. For instance, Pt and Pd are non-magnetic in bulk but become magnetic in atomic chains.[1, 2]

Low-dimensional systems have become a topic of intense research interest in pursuit of atomic-scale magnetic storage devices and future spintronics applications.[3, 4] The development of high density magnetic recording devices is one driving force to investigate new nanostructured magnetic materials. The idea is to develop future high-density magnetic data-storage technologies, by moving from two-dimensional (regular hard disk drive) to one-dimensional (nanowire) and zero-dimensional (single atom) magnetism. Among others one-dimensional periodic linear arrangements of atoms (chains) have been investigated from experimental[5, 6, 7, 4, 3] and theoretical points of view.[8, 9, 10, 11, 12, 13, 14, 15, 16, 17, 18] Most of the experimental investigations and possible applications seek a high packing density of such chains.

Such properties depend on the formation and morphology of the low-dimensional system, therefore modern techniques have been developed to grow tailored structures. These structures can be self-assembled or built by means of the scanning tunneling microscopy (STM).

In self-assembly, the substrate defect is used as a template for growth and offers the possibility to create nanoscale patterns with high densities. Periodic atomically stepped substrates can be used to create one-dimensional nanostructures. The main idea is to exploit the 1D symmetry provided by an array of parallel steps on a vicinal surface. Along this surface, the deposited material can nucleate via a procedure called step decoration. The stepped substrate is used to grow atomic chains by self-assembly, exploiting one-dimensional structures provided by topographic features such as step edges[3] or trenches of reconstructed surfaces. The latter has been observed for Fe chains on Ir(001)[19] and Au chains on Si(111).[20]

STM allows mapping of surface topography with atomic resolution. In this technique, an atomic chain can be formed by manipulation with the STM tip. STM also provides

a direct way to study the magnetic properties of individual chains. For instance, Serrate *et al.* demonstrated non-collinear spin alignment in linear Co chains on Mn/W(110) surface using STM[21] and Hirjibehedin and co-workers created linear Mn chains of up to ten atoms on an insulating CuN/Cu(001) surface.[4]

Chains or nanostripes usually grow on lower terraces along ascending step edges. Cu surfaces can be prepared with many atom-high steps. Surprisingly, Shen *et al.*[5, 6] have demonstrated that Fe nanostripes grow on the upper terrace of a stepped Cu(111) surface. The kinetic mechanism which leads to the formation of such structures has been a puzzle for almost a decade. Mo *et al.* investigated this system within the framework of density functional theory and explained that the growth of Fe nanowires is a two-stage process.[18] In the first stage, an embedded Fe chain is formed in the Cu stepped surface one lateral lattice constant away from the descending step. This embedded Fe chain acts as an attractor for the second row of Fe atoms in the second stage. This growth process was experimentally confirmed later by Guo *et al.*. [7] The kinetic Monte Carlo simulations on this system have also exhibited an optimal temperature and deposition flux for the formation of ordered Fe nanowires on stepped Cu(111) surfaces.[22] Only the growth of one mono-layer (ML) high stripes was assumed in these simulations. Furthermore, the Cu(111) stepped surface with the embedded Fe chain can be used as a template for the deposition of other $3d$ transition metals (TM) atoms to form a chain on top of the embedded Fe chain. It is the interplay between dimensionality, local environment, and magnetic properties which drives the intense interest in such systems.[18]

This thesis provides a systematic discussion of one-dimensional magnetic nanostructures grown on a vicinal Cu(111) surface using the above-mentioned template. This study is focused on $3d$ transition metals from Sc to Ni because they offer a wide scope of complex magnetic structures in higher dimensions some of which are bulk ferromagnets.

This thesis is organized as follows.

In chapter (2), the main concepts of many-body quantum mechanics are briefly discussed. With the introduced terminology, a description of DFT follows in relation to the implementation used in this study. Subsequently, a brief description of the finite temperature study of the system is presented.

In chapter (3), the copper bulk properties are discussed, as well as comparison with the experimental results. Subsequently, the relaxations, surface energies, and work functions of the Cu(111) surface are calculated and compared with the experimental results.

Details of growth of $3d$ TM nanowires on Cu surface are discussed in chapter (4). The presentation of the results and discussion start with an explanation of the magnetic structures. Those structures are investigated for TM-Fe wires embedded in the Cu surface and investigated for comparison to isolated free standing wires as well. A detailed compilation of the real structure data of the embedded TM-Fe wires follows. After the presentation of the ground state energies and magnetic moments, a discussion follows.

The magnetic properties of the TM-Fe wires are discussed in chapter (5) by presenting a systematic investigation of the spin couplings in magnetic TM-Fe wires by analyzing the exchange interactions. There are two magnetic coupling interactions for TM-Fe systems explored in this chapter: intrawire and interwire.

1 Introduction

In chapter (6), the magnetic anisotropy energies (MAE) are calculated, including magnetocrystalline and shape anisotropies of TM-Fe wires in both isolated and deposited cases. The TM-Fe structures are optimized for different orientations of the magnetization with respect to the crystallographic axes of the systems. The magnetic anisotropy energies and the anisotropies of spin and orbital moments are determined. Finally, the magnetic properties of TM-Fe wires at finite temperatures are discussed in Sec. (6.4).

2 Theoretical Background

To understand the material properties from a theoretical point of view, quantum mechanics provides a strong tool to study the behavior of materials at the atomic scale. By solving the quantum mechanical wave equation of the system, the properties of a system can be obtained. This turns into the Schrödinger equation for non-relativistic systems. This is practically an impossible task. Although the exact solution is not known, there are many methods to deal with many-body problems by simplifying the general Hamiltonian with the introduction of some approximations. These methods can apply to a limited number of many-body problems which are solvable. Density Functional Theory (DFT) is a conceptual improvement which leads to large simplification of the many body problem and allows practical computation of properties of materials. In principle, it is an exact theory except for few approximations used to treat the many body correlation effects. DFT is one the most favored method for the materials simulations, since most of the properties predicted by DFT find direct experimental support. The predictive ability for materials properties allows us to study more complex materials, for which experiments are still lacking. In this chapter, DFT is introduced as a method dealing with many-body systems, considering the Hohenberg-Kohn-Sham formulation of density functional theory DFT [23, 24]. Therefore, in the following section, the main concepts of many-body quantum mechanics are briefly discussed. With the introduced terminology, a description of DFT follows, in relation to the implementation used in this study. Subsequently, a brief description of the finite temperature study of the system is presented.

2.1 The Many-Body Problem

The entire information of a system of interacting electrons and nuclei is contained in the many-body wavefunction Ψ , which can be obtained by solving the Schrödinger equation. This is a starting point to investigate properties of materials. The problematic issue concerns the number of particles that are involved and the coupling and interactions of the particles (in order of 10^{23} particles). This problem can be solved using approximate methods.

The N -electron quantum system (without considering spin) is described by a function of the spatial \mathbf{r} coordinate of each electron, as well as the spatial coordinates \mathbf{R} of the nuclei, $\Psi(\mathbf{r}_1, \mathbf{r}_2 \dots \mathbf{r}_N, \mathbf{R}_1, \mathbf{R}_2 \dots \mathbf{R}_M)$. The properties of any (non-relativistic) time independent quantum system are determined by the Schrödinger equation:

$$\hat{H}\Psi(\mathbf{r}_1, \mathbf{r}_2 \dots \mathbf{r}_N, \mathbf{R}_1, \mathbf{R}_2 \dots \mathbf{R}_M) = E\Psi(\mathbf{r}_1, \mathbf{r}_2 \dots \mathbf{r}_N, \mathbf{R}_1, \mathbf{R}_2 \dots \mathbf{R}_M) \quad (2.1)$$

2 Theoretical Background

\hat{H} , Ψ and E are the Hamiltonian, many-body wave-function and total energy of the system, respectively. The Hamiltonian for the solid system in atomic units is given by

$$\begin{aligned} \hat{H} = & - \sum_{i=1}^M \frac{1}{2M_i} \nabla_{\mathbf{R}_i}^2 - \sum_{i=1}^N \frac{1}{2} \nabla_{\mathbf{r}_i}^2 + \sum_i^M \sum_{j>i}^M \frac{Z_i Z_j}{|\mathbf{R}_i - \mathbf{R}_j|} \\ & - \sum_{i=1}^N \sum_{j=1}^M \frac{Z_j}{|\mathbf{r}_i - \mathbf{R}_j|} + \sum_{i=1}^N \sum_{j>i}^N \frac{1}{|\mathbf{r}_i - \mathbf{r}_j|}, \end{aligned} \quad (2.2)$$

where, M and N are the number of nuclei and electrons in the system, M_i , Z and \mathbf{R} are the mass, charge and position of the nuclei and \mathbf{r} is the position of the electrons.

The first two terms in equation (2.2) are the kinetic energy contributions of the nuclei and the electrons respectively, and the rest are Coulombic potential energy terms representing the ion-ion repulsion, ion-electron attraction and the electron-electron repulsion respectively. Although in principle everything is known exactly, the Schrödinger equation (2.1) with this Hamiltonian is very difficult to solve directly. Hence, the quantum many-body problem is centered upon finding intelligent approximations to the Hamiltonian (2.2) and the many body wavefunction Ψ , that retain the correct physics and are computationally tractable to solve.

2.2 Born-Oppenheimer Approximation

The concept behind this approximation comes from the fact that the mass of a nucleus is much larger than the mass of an electron. Even for the simplest nuclei, a single proton, the nuclei mass is approximately 2000 times larger than electron mass. Due to this fact, the timescales of electronic and nuclear motion are different. This is the motivation for the Born-Oppenheimer approximation. The difference in the masses allows the electrons to respond almost instantly to the motion of the nuclei. This approximation was proposed in 1927, in the early period of quantum mechanics, by Born and Oppenheimer. The wavefunction can then be taken to be the product of the electronic and nuclear parts:

$$\Psi(\mathbf{r}_1, \dots, \mathbf{r}_N, \mathbf{R}_1, \dots, \mathbf{R}_M) = \Psi_e(\mathbf{r}_1, \dots, \mathbf{r}_N, \mathbf{R}_1, \dots, \mathbf{R}_M) \Psi_n(\mathbf{R}_1, \dots, \mathbf{R}_M). \quad (2.3)$$

With this approximation the electronic Schrödinger equation is solved first, yielding the wavefunction $\Psi_e(\mathbf{r}_1, \dots, \mathbf{r}_N, \mathbf{R}_1, \dots, \mathbf{R}_M)$ depending on electrons only. During this solution the nuclei are fixed in a certain configuration. Here, please note that the \mathbf{R}_i in the wave function ($\Psi_e(\mathbf{r}_1, \dots, \mathbf{r}_N, \mathbf{R}_1, \dots, \mathbf{R}_M)$) are not variables but parameters.

Solving the Schrödinger equation with this approximation is still complex in most cases, because the many-electron wave-function contains $3N$ variables. In principle, the N -body wave function of the system can be approximated by a single Slater determinant. By using a variational method, a set of N -coupled equations for the N spin orbitals can be obtained. The solution of these equations yields the Hartree-Fock wave function and

finally energy of the system. In the following section, this method will be discussed in detail.

2.3 Hartree-Fock Theory

Hartree-Fock theory is an approximate theory for solving the many-body Hamiltonian, where the true N -electron wavefunction Ψ is replaced by a product of single-particle orbitals, $\psi_i(\mathbf{r}_i s_i)$,

$$\Psi(\mathbf{r}_1 s_1, \mathbf{r}_2 s_2, \dots, \mathbf{r}_N s_N) = \frac{1}{\sqrt{N!}} \psi_1(\mathbf{r}_1 s_1) \psi_2(\mathbf{r}_2 s_2) \dots \psi_N(\mathbf{r}_N s_N), \quad (2.4)$$

where $\psi_i(\mathbf{r}_i s_i)$ is comprised of a spatial function $\phi_i(\mathbf{r}_i)$, and an electron spin function $\sigma(s_i)$ such that,

$$\psi_i(\mathbf{r}_i) = \phi_i(\mathbf{r}_i) \sigma(s_i), \quad (2.5)$$

and $\sigma = \alpha, \beta$ exhibit up-spin and down-spin electrons respectively. The wavefunction must be antisymmetric with respect to an interchange of any two electron positions. This property is required by the Pauli exclusion principle.

$$\Psi(\mathbf{r}_1 s_1, \dots, \mathbf{r}_i s_i, \dots, \mathbf{r}_j s_j, \dots, \mathbf{r}_N s_N) = -\Psi(\mathbf{r}_1 s_1, \dots, \mathbf{r}_j s_j, \dots, \mathbf{r}_i s_i, \dots, \mathbf{r}_N s_N), \quad (2.6)$$

This problem was corrected by the Hartree-Fock approximation [25] which accounts for electron exchange interactions by writing the wavefunction as an antisymmetrised product of orbitals. The Hartree-Fock wavefunction Ψ_{HF} amounts to a linear combination of the terms in (2.4), which includes all permutations of the electron coordinates with the corresponding weights ± 1 , and so fulfils (2.7). In 1951 Slater [26] realized that the Hartree-Fock wavefunction can be efficiently represented as an $N \times N$ determinant, now known as a Slater determinant:

$$\Psi_{HF} = \frac{1}{\sqrt{N!}} \begin{vmatrix} \psi_1(\mathbf{r}_1 s_1) & \psi_1(\mathbf{r}_2 s_2) & \dots & \psi_1(\mathbf{r}_N s_N) \\ \psi_2(\mathbf{r}_1 s_1) & \psi_2(\mathbf{r}_2 s_2) & \dots & \psi_2(\mathbf{r}_N s_N) \\ \vdots & \vdots & \dots & \vdots \\ \psi_N(\mathbf{r}_1 s_1) & \psi_N(\mathbf{r}_2 s_2) & \dots & \psi_N(\mathbf{r}_N s_N) \end{vmatrix}, \quad (2.7)$$

where the orbitals are the orthonormal sets,

$$\int \psi_i^*(\mathbf{r}) \psi_j(\mathbf{r}) d\mathbf{r} = \langle \psi_i | \psi_j \rangle = \delta_{ij}. \quad (2.8)$$

Shorthand notation of the Slater determinant is written as,

$$\Psi_{HF} = \frac{1}{\sqrt{N!}} \det[\psi_1(\mathbf{r}_1 s_1) \psi_2(\mathbf{r}_2 s_2) \dots \psi_N(\mathbf{r}_N s_N)] \quad (2.9)$$

The expectation value of the Hamiltonian with the above Slater determinant yields,

$$\begin{aligned} E_{HF} &= \langle \Psi_{HF} | \hat{H} | \Psi_{HF} \rangle \\ &= \sum_i^N \int \psi_i^*(\mathbf{r}) \left(-\frac{1}{2} \nabla^2 + v_{ext}(\mathbf{r}) \right) \psi_i(\mathbf{r}) d\mathbf{r} \\ &\quad + \frac{1}{2} \sum_i^N \sum_j^N \int \int \frac{|\psi_i(\mathbf{r})|^2 |\psi_j(\mathbf{r}')|^2}{|\mathbf{r} - \mathbf{r}'|} d\mathbf{r} d\mathbf{r}' \\ &\quad - \frac{1}{2} \sum_i^N \sum_j^N \int \int \frac{\psi_i^*(\mathbf{r}) \psi_i(\mathbf{r}') \psi_j^*(\mathbf{r}') \psi_j(\mathbf{r})}{|\mathbf{r} - \mathbf{r}'|} \delta_{s_i s_j} d\mathbf{r} d\mathbf{r}' \end{aligned} \quad (2.10)$$

The last term is of significant interest since it arises from the antisymmetric nature of the Hartree-Fock wavefunction - it vanishes when $s_i \neq s_j$. Consequently this term is called the exchange energy E_X . Hartree-Fock theory, by assuming a single-determinant form for the wavefunction, neglects correlation between electrons. The electrons are subject to an average non-local potential arising from the other electrons, which can lead to a poor description of the electronic structure. Although qualitatively correct in many materials and compounds, Hartree-Fock theory is insufficiently accurate to make accurate quantitative predictions.

2.4 Density Functional Theory (DFT)

Density functional theory is a very successful approach for the description of ground state properties of the solids. One approach to solve the many-electron problem is using the electron density as the central unknown variable, rather than the many-electron wavefunction. This approach was proposed initially by Thomas and Fermi in the 1920s [27, 28]. This model simplifies the problem considerably since the density contains only three degrees of freedom. In this model, the electron many-body problem is based uniquely on the electron density $n(\mathbf{r})$. Due to the severe shortcomings of this method, they probably never imagined that an exact theory could be based on the density. However, almost forty years later, Hohenberg and Kohn proved in a seminal paper [23] that this was indeed possible. In two remarkably powerful theorems they formally established the electron density as the central quantity describing electron interactions, and so devised the formally exact ground-state method known as density functional theory (DFT). The two Hohenberg-Kohn theorems are now described.

2.4.1 The Hohenberg-Kohn Theorems

The foundation of DFT was formulated and proved by two fundamental theorems. These theorems relate to any system consisting of electrons moving under the influence of an

external potential $v_{ext}(\mathbf{r})$. They are as follows:

Theorem 1

The external potential $v_{ext}(\mathbf{r})$, and therefore the total energy, is a unique functional of the electron density $n(\mathbf{r})$.

The energy functional $E[n(\mathbf{r})]$ mentioned briefly to in the first Hohenberg-Kohn theorem can be written in terms of the external potential $v_{ext}(\mathbf{r})$ in the following form,

$$E[n(\mathbf{r})] = \int n(\mathbf{r}) v_{ext}(\mathbf{r}) d\mathbf{r} + F[n(\mathbf{r})], \quad (2.11)$$

where $F[n(\mathbf{r})]$ is an unknown, but universal functional of the electron density $n(\mathbf{r})$ only. Correspondingly, a Hamiltonian for the system can be written in such a way that the electron wavefunction Ψ that minimizes the expectation value gives the groundstate energy (2.11) (assuming a non-degenerate groundstate),

$$E[n(\mathbf{r})] = \langle \Psi | \hat{H} | \Psi \rangle. \quad (2.12)$$

and the Hamiltonian of the system can be written as,

$$\hat{H} = \hat{F} + \hat{V}_{ext}, \quad (2.13)$$

where \hat{F} is the electronic Hamiltonian consisting of a kinetic energy operator \hat{T} and an interaction operator \hat{V}_{ee} ,

$$\hat{F} = \hat{T} + \hat{V}_{ee}. \quad (2.14)$$

The electron operator \hat{F} is the same for all N -electron systems, therefore \hat{H} is totally specified by the number of electrons N , and the external potential $v_{ext}(\mathbf{r})$.

The proof of the first theorem obtains with proof by contradiction. First we assume there are two different external potentials, $v_{ext,1}(\mathbf{r})$ and $v_{ext,2}(\mathbf{r})$, that give rise to the same density $n_0(\mathbf{r})$. The associated Hamiltonians, \hat{H}_1 and \hat{H}_2 , will therefore have different groundstate wavefunctions, Ψ_1 and Ψ_2 , that each yield $n_0(\mathbf{r})$. Using the variational principle [29], together with (2.14) yields,

$$E_1^0 < \langle \Psi_2 | \hat{H}_1 | \Psi_2 \rangle = \langle \Psi_2 | \hat{H}_2 | \Psi_2 \rangle + \langle \Psi_2 | \hat{H}_1 - \hat{H}_2 | \Psi_2 \rangle \quad (2.15)$$

$$= E_2^0 + \int n_0(\mathbf{r}) [v_{ext,1}(\mathbf{r}) - v_{ext,2}(\mathbf{r})] d\mathbf{r} \quad (2.16)$$

where E_1^0 and E_2^0 are the groundstate energies of \hat{H}_1 and \hat{H}_2 respectively. It is at this point that the Hohenberg-Kohn theorems, and therefore DFT, apply rigorously to the

2 Theoretical Background

groundstate only. A disparity similar expression for (2.15) holds when the subscripts are interchanged. Hence adding the interchanged disparity to Eq. (2.16) leads to the result:

$$E_1^0 + E_2^0 < E_2^0 + E_1^0 \quad (2.17)$$

which is a contradiction, and as a result the groundstate density must uniquely be determined by the external potential $v_{ext}(\mathbf{r})$ (within an additive constant). Stated simply, the electrons determine the positions of the nuclei in a system, and also all groundstate electronic properties, because as mentioned earlier, $v_{ext}(\mathbf{r})$ and N completely define \hat{H} .

Theorem 2

The groundstate energy can be obtained variationally: the density that minimizes the total energy is the exact groundstate density.

The proof of the second theorem is also straightforward: as just shown, $n(\mathbf{r})$ determines $v_{ext}(\mathbf{r})$, N and $v_{ext}(\mathbf{r})$ determine \hat{H} and therefore Ψ . This ultimately means Ψ is a functional of $n(\mathbf{r})$, and so the expectation value of \hat{F} is also a functional of $n(\mathbf{r})$, i.e.

$$F[n(\mathbf{r})] = \langle \psi | \hat{F} | \psi \rangle. \quad (2.18)$$

A density that is the ground-state of some external potential is known as v -representable. Following from this, a v -representable energy functional $E_v[n(\mathbf{r})]$ can be defined in which the external potential $v(\mathbf{r})$ is unrelated to another density $n'(\mathbf{r})$,

$$E_v[n(\mathbf{r})] = \int n'(\mathbf{r}) v_{ext}(\mathbf{r}) d\mathbf{r} + F[n'(\mathbf{r})], \quad (2.19)$$

and the variational principle states that,

$$\langle \psi' | \hat{F} | \psi' \rangle + \langle \psi' | \hat{V}_{ext} | \psi' \rangle > \langle \psi | \hat{F} | \psi \rangle + \langle \psi | \hat{V}_{ext} | \psi \rangle \quad (2.20)$$

where ψ is the wavefunction associated with the correct groundstate $n(\mathbf{r})$. This leads to,

$$\int n'(\mathbf{r}) v_{ext}(\mathbf{r}) d\mathbf{r} + F[n'(\mathbf{r})] > \int n(\mathbf{r}) v_{ext}(\mathbf{r}) d\mathbf{r} + F[n(\mathbf{r})], \quad (2.21)$$

and therefore the variational principle of the second Hohenberg-Kohn theorem is obtained,

$$E_v[n'(\mathbf{r})] > E_v[n(\mathbf{r})]. \quad (2.22)$$

In spite of the fact that the Hohenberg-Kohn theorems are extremely strong, but there is no way to compute the ground-state density of a system practically. One year after the first DFT paper by Hohenberg and Kohn, Kohn and Sham [24] invented a simple method for performing DFT calculations, that keeps the exact nature of DFT. This method is delineated next.

2.4.2 The Kohn-Sham Method

The Kohn-Sham method is based on the mapping of the full interacting system with the real potential, onto an imaginary non-interacting system in accordance with, the electrons move within an effective ‘‘Kohn-Sham’’ single-particle potential $v_{KS}(\mathbf{r})$. The Kohn-Sham formulation is still accurate because it gives the same groundstate density as the real system, but extremely promotes the calculation.

Let us consider the variational problem presented in the second Hohenberg-Kohn theorem - the groundstate energy of a many-electron system can be acquired by minimising the energy functional (2.13), subject to the constraint that the number of electrons N is conserved, which leads to,

$$\delta \left[F[n(\mathbf{r})] + \int v_{ext}(\mathbf{r})n(\mathbf{r}) d\mathbf{r} - \mu \left(\int n(\mathbf{r}) d\mathbf{r} - N \right) \right] = 0, \quad (2.23)$$

and the related Euler expression is,

$$\mu = \frac{\delta F[n(\mathbf{r})]}{\delta n(\mathbf{r})} + v_{ext}(\mathbf{r}), \quad (2.24)$$

where μ is the Lagrange multiplier connected to the limitation of constant N . The idea of Kohn and Sham was to establish a system where the kinetic energy could be determined exactly, since this was a major problem in the Thomas-Fermi theory. The corresponding groundstate wavefunction Ψ_{KS} for this type of system is given exactly by a determinant of single-particle orbitals $\psi_i(\mathbf{r}_i)$,

$$\Psi_{KS} = \frac{1}{\sqrt{N!}} \det[\psi_1(\mathbf{r}_1)\psi_2(\mathbf{r}_2) \dots \psi_N(\mathbf{r}_N)] \quad (2.25)$$

The universal functional $F[n(\mathbf{r})]$ can be divided into three terms, the first two of which are known exactly and comprise the majority of the energy, the third being an unknown quantity,

$$F[n(\mathbf{r})] = T_s[n(\mathbf{r})] + E_H[n(\mathbf{r})] + E_{XC}[n(\mathbf{r})]. \quad (2.26)$$

$T_s[n(\mathbf{r})]$ is the kinetic energy of a non-interacting electron gas of density $n(\mathbf{r})$, $E_H[n(\mathbf{r})]$ is the classical electrostatic (Hartree) energy of the electrons,

$$E_H[n(\mathbf{r})] = \frac{1}{2} \int \int \frac{n(\mathbf{r})n(\mathbf{r}')}{|\mathbf{r} - \mathbf{r}'|} d\mathbf{r} d\mathbf{r}', \quad (2.27)$$

and $E_{XC}[n(\mathbf{r})]$ is the exchange-correlation energy containing the difference between the exact and non-interacting kinetic energies and also the non-classical contribution

2 Theoretical Background

to the electron-electron interactions, of which the exchange energy is a part. In the Kohn-Sham prescription the Euler equation given in (2.26) now turns into,

$$\mu = \frac{\delta T_s[n(\mathbf{r})]}{\delta n(\mathbf{r})} + v_{KS}(\mathbf{r}), \quad (2.28)$$

where the Kohn-Sham potential $v_{KS}(\mathbf{r})$ is obtained by,

$$v_{KS}(\mathbf{r}) = v_{ext}(\mathbf{r}) + v_H(\mathbf{r}) + v_{XC}(\mathbf{r}), \quad (2.29)$$

with the Hartree potential $v_H(\mathbf{r})$,

$$v_H(\mathbf{r}) = \frac{\delta E_H[n(\mathbf{r})]}{\delta n(\mathbf{r})} = \int \frac{n(\mathbf{r}')}{|\mathbf{r} - \mathbf{r}'|} d\mathbf{r}', \quad (2.30)$$

and the exchange-correlation potential $v_{XC}(\mathbf{r})$,

$$v_{XC}(\mathbf{r}) = \frac{\delta E_{XC}[n(\mathbf{r})]}{\delta n(\mathbf{r})}. \quad (2.31)$$

The important point to realize is that equation (2.28) is precisely the same equation which would be obtained for a non-interacting system of particles moving in an external potential $v_{KS}(\mathbf{r})$. The ground-state density for this non-interacting system is obtained in practice by solving the one-electron Schrödinger equations;

$$\left[-\frac{1}{2}\nabla^2 + v_{KS}(\mathbf{r}) \right] \psi_i(\mathbf{r}) = \varepsilon_i \psi_i(\mathbf{r}), \quad (2.32)$$

where ε_i are Lagrange multipliers corresponding to the orthonormality of the N single-particle states $\psi_i(\mathbf{r})$, and the density is obtained by,

$$n(\mathbf{r}) = \sum_{i=1}^N |\psi_i(\mathbf{r})|^2. \quad (2.33)$$

The non-interacting kinetic energy $T_s[n(\mathbf{r})]$ is therefore given by,

$$T_s[n(\mathbf{r})] = -\frac{1}{2} \sum_{i=1}^N \int \psi_i^*(\mathbf{r}) \nabla^2 \psi_i(\mathbf{r}) d\mathbf{r}. \quad (2.34)$$

(2.31), (2.32) and (2.33) equations, the Kohn-Sham equations, should be solved self-consistently. Because $v_{KS}(\mathbf{r})$ depends on the density through the exchange-correlation potential.

2 Theoretical Background

N equations are solved in Kohn-Sham theory to obtain the set of Lagrange multipliers $\{\varepsilon_i\}$, in contrast to one equation that determines μ when solving for the density directly, so that we can obtain the kinetic energy exactly. The advantage of the Kohn-Sham method is that as the complexity of a system increases, due to N increasing, the problem becomes no more difficult, only the number of single-particle equations to be solved increases.

The Kohn-Sham theory is approximate in practice because of the unknown exchange-correlation functional $E_{XC}[n(\mathbf{r})]$, despite the fact that exact in principle. An implicit definition of $E_{XC}[n(\mathbf{r})]$ can be given through (2.28) as,

$$E_{XC}[n(\mathbf{r})] = T[n(\mathbf{r})] - T_s[n(\mathbf{r})] + E_{ee}[n(\mathbf{r})] - E_H[n(\mathbf{r})] \quad (2.35)$$

$T[n(\mathbf{r})]$ and $E_{ee}[n(\mathbf{r})]$ are the kinetic and electron-electron interaction energies respectively. The idea is to reduce the unknown contribution to the total energy of the non-interacting system, and this is only presented in the exchange-correlation energy, however it is still an important contribution because the binding energy of many systems is about the same size as $E_{XC}[n(\mathbf{r})]$, so an accurate description of exchange and correlation is critical for the prediction of binding properties. The current approximations for the exchange-correlation energy are not satisfactory, consequently the development of improved exchange-correlation functionals is necessary.

2.4.3 The Exchange-Correlation Functionals

As discussed in previous sections, the DFT theory based on Hohenberg-Kohn theorems is an exact theory. In practice, in the Kohn-Sham formalism, an approximation has to be adopted for treating the exchange-correlation potential.

The Local Density Approximation (LDA)

One of the approximations which was proposed by Kohn and Sham is the local density approximation (LDA) [24]. The LDA is derived from the homogeneous electron gas and can be written as

$$E_{XC}^{\text{LDA}}[n(\mathbf{r})] = \int n(\mathbf{r}) V_{XC}^{\text{LDA}}(\mathbf{r}) d\mathbf{r} \quad (2.36)$$

where V_{XC}^{LDA} is a function of density. The exchange part of the LDA is analytically given by

$$V_X^{\text{LDA}} = -\frac{3}{4} \left(\frac{3}{\pi}\right)^{1/3} \int n(\mathbf{r})^{4/3} d\mathbf{r} \quad (2.37)$$

For the correlation term in LDA, a more accurate value can be obtained from quantum Monte Carlo methods. The parametric form of correlation in this case is given as,

$$V_C^{\text{LDA}} = \begin{cases} A \ln(r_s) + B + r_s(C \ln(r_s) + D) & \text{for high density limit} \\ \frac{1}{2} \left(\frac{g_0}{r_s} + \frac{g_1}{r_s^{3/2}} + \dots \right) & \text{for low density limit} \end{cases} \quad (2.38)$$

where, r_s is related to the density as

$$\frac{4}{3} \pi r_s^3 = \frac{1}{\rho} \quad (2.39)$$

and A, B, C, D, g_0, g_1 are some parameters. The LDA exchange-correlation functionals have been used with much success, especially for metallic systems. This is because metals can be described by an effective free-electron model. Making generalization of the LDA to include electron spin, leads to the local spin-density approximation (LSDA):

$$E_{\text{XC}}^{\text{LSDA}}[n_{\uparrow}, n_{\downarrow}] = \int V_{\text{XC}}^{\text{LSDA}}(n_{\uparrow}, n_{\downarrow}) n(\mathbf{r}) d\mathbf{r} \quad (2.40)$$

Using quantum Monte Carlo, accurate formulae for the exchange-correlation energy density $V_{\text{XC}}^{\text{LSDA}}(n_{\uparrow}, n_{\downarrow})$ can be constructed.[30]

The Generalized-Gradient Approximations (GGA)

As shown above, the LDA applies the exchange-correlation energy for the uniform electron gas at every point in the system. For nonuniform charge densities the exchange-correlation energy can deviate significantly from the uniform result. This deviation can be expressed in terms of the gradient and higher spatial derivatives of the total charge density. If we take into account the gradient of the density at the same coordinate then:

$$E_{\text{XC}}^{\text{GGA}}[n_{\uparrow}, n_{\downarrow}] = \int V_{\text{XC}}^{\text{GGA}}(n_{\uparrow}, n_{\downarrow}, \vec{\nabla} n_{\uparrow}, \vec{\nabla} n_{\downarrow}) n(\mathbf{r}) d\mathbf{r} \quad (2.41)$$

For systems where the charge density is slowly varying, the GGA is an improvement over LDA. Using the GGA good results for structures and ground-state energies have been achieved. [31, 32, 33, 34] Transition metals on the other hand need gradient corrections in the LDA, commonly known as the generalized gradient approximations (GGA), for better electronic structure description because of the participation of d -orbitals which are correlated.

2.5 Electronic Structure Calculations

2.5.1 Plane-Wave Formulation of DFT

Now, the plane-wave pseudopotential formulation of DFT is described, in fact, it is used in most of the studies presented here. This method is well established within the physics community as it is particularly suited to describing infinite periodic systems such as solids.

Bloch's Theorem

Bloch's theorem states that the wavefunction of a particle (usually, an electron) $\psi_{j,\mathbf{k}}$, placed in a periodic potential, may be written as the product of a lattice periodic part $u_j(\mathbf{r})$ and a plane wave envelope function $e^{i\mathbf{k}\cdot\mathbf{r}}$,

$$\psi_{j,\mathbf{k}}(\mathbf{r}) = u_j(\mathbf{r}) e^{i\mathbf{k}\cdot\mathbf{r}}, \quad (2.42)$$

where the subscript j indicates the band index and \mathbf{k} is a vector in reciprocal space that is confined to the first Brillouin zone of the reciprocal lattice. Since $u_j(\mathbf{r})$ has the same periodicity as the direct lattice, it can be expressed in terms of a discrete plane-wave basis set with wavevectors \mathbf{G} that are reciprocal lattice vectors of the crystal, i.e.

$$u_j(\mathbf{r}) = \sum_{\mathbf{G}} c_{j,\mathbf{G}} e^{i\mathbf{G}\cdot\mathbf{r}}, \quad (2.43)$$

where $\mathbf{G} \cdot \mathbf{R} = 2\pi m$, where m is an integer, \mathbf{R} are the crystal lattice vectors and $c_{j,\mathbf{G}}$ are the plane-wave coefficients. The above results show that the electron wavefunctions can be expanded in terms of a linear combination of plane-waves,

$$\psi_{j,\mathbf{k}}(\mathbf{r}) = \sum_{\mathbf{G}} c_{j,\mathbf{k}+\mathbf{G}} e^{i(\mathbf{k}+\mathbf{G})\cdot\mathbf{r}}. \quad (2.44)$$

Plane-waves are a method of representing electron wavefunctions. They offer a complete basis set that is independent of the type of crystal and treats all areas of space equally. Plane waves are also an orthonormal complete set. Any function belonging to the class of continuous normalizable functions can be expanded with arbitrary precision in such a basis set. We thus do not have to invent a new basis set for every atom in the periodic table nor modify them in different materials. This is in contrast to some other basis sets which use localized functions such as Gaussians which are dependent on the positions of the ions.

Kohn-Sham Equations Represented in the Plane-Waves

Using the lattice periodicity and Bloch's theorem yields the one-electron wavefunctions being expressed in terms of a Fourier expansion using plane waves as a basis set. The electronic wavefunctions in periodic systems turns out a particularly simple formulation of the Kohn-Sham equations in DFT. The fact is applied that the various contributions to the local potential in the Kohn-Sham equation (2.32) may be written in the following formation,

$$v(\mathbf{r}) = \sum_{\mathbf{G}} \bar{v}(\mathbf{G}) e^{i\mathbf{G}\cdot\mathbf{r}}, \quad (2.45)$$

2 Theoretical Background

$\bar{v}(\mathbf{G})$ represents the Fourier transform of the corresponding real-space quantity, and substitutes the plane-wave expansions given by Eq. (2.45) into Eq. (2.32), leading to a reciprocal-space representation of the Kohn-Sham equations,

$$\sum_{\mathbf{G}'} \left[\frac{1}{2} |\mathbf{k} + \mathbf{G}|^2 \delta_{\mathbf{G}, \mathbf{G}'} + \bar{v}_{ext}(\mathbf{G} - \mathbf{G}') + \bar{v}_H(\mathbf{G} - \mathbf{G}') + \bar{v}_{XC}(\mathbf{G} - \mathbf{G}') \right] c_{j, \mathbf{k} + \mathbf{G}'} = \varepsilon_i(\mathbf{k}) c_{j, \mathbf{k} + \mathbf{G}}, \quad (2.46)$$

The dimension of the plane-wave basis set has to be infinite for an exact calculation. The plane-waves at the lower end of the kinetic energy range are most important, therefore a practical solution of (2.46) can be obtained by truncating the basis set to a finite number of plane-waves. This is defined by the kinetic cutoff energy E_{cut} ,

$$\frac{1}{2} |\mathbf{k} + \mathbf{G}|^2 \leq E_{cut}. \quad (2.47)$$

In principle, the accuracy of a plane-wave basis set can be systematically improved by increasing E_{cut} , and thus this fixes the highest reciprocal lattice vector \mathbf{G} used in the plane wave expansion, resulting in a finite basis set. The main disadvantage of plane-waves is that they are not efficient at describing wavefunctions with large curvature such as in the core regions of atoms, consequently such regions of space require an unreasonably large number of plane-waves to be sufficiently accurate, and so would dominate the convergence of E_{cut} . This problem can be overcome with the pseudopotential approximation.

k-point Sampling

Based on Bloch's theorem, the electrons within the unit cell can be considered at an infinite number of \mathbf{k} -points within the first Brillouin zone. This means any real-space integral over a periodic system with infinite extent can be replaced by an integral in reciprocal-space over the first Brillouin zone. This requires calculating the periodic functions at an infinite number of points in reciprocal space, referring to the \mathbf{k} -points. This is a consequence of the infinite number of electrons. This problem can be overcome by exploiting the fact that electron wavefunctions do not change appreciably over a small distances in \mathbf{k} -space, therefore the integrations can be performed as summations over a finite, but sufficiently dense, mesh of \mathbf{k} -points. Therefore, any integrated function $f(\mathbf{r})$, for example the density or total energy, can be computed as a discontinuous summation,

$$\int_{BZ} F(\mathbf{k}) d\mathbf{k} = \frac{1}{\Omega} \sum_j w_j F(\mathbf{k}_j) \quad (2.48)$$

here $F(\mathbf{k})$ is the Fourier transform of $f(\mathbf{r})$, Ω is the cell volume and w_j are weighting factors. The number of \mathbf{k} -points required for a sufficiently accurate calculation must be

2 Theoretical Background

checked by \mathbf{k} -point sampling. This is a procedure that the total energy of the system is converged with respect to increasing the number of \mathbf{k} -point.

The \mathbf{k} -points within the Brillouin zone should be distributed in such a way to result in an efficient description of a particular system. This can significantly save the computational time. Different approaches for obtaining these optimal or special \mathbf{k} -point sets have been discussed in the past [35, 36, 37]. However the calculations performed in this work employ the Monkhorst-Pack method [38], whereby the \mathbf{k} -points are distributed uniformly throughout space in rows and columns that follow the shape of the Brillouin zone,

$$\mathbf{k}_j = x_{1j}\mathbf{b}_1 + x_{2j}\mathbf{b}_2 + x_{3j}\mathbf{b}_3 \quad (2.49)$$

$\mathbf{b}_1, \mathbf{b}_2, \mathbf{b}_3$ are the reciprocal lattice vectors,

$$x_{ij} = \frac{l_i}{n_j}, \quad j = 1, \dots, n_j. \quad (2.50)$$

where l_i are the reciprocal lattice vectors lengths and n_j is the number of special points in the set.

Typically, the point-group symmetry of the crystal is used to produce a smaller subset of the full special \mathbf{k} -point set, containing points located within the irreducible part of the Brillouin zone. The values of the weighting factors w_j are adjusted according to this new \mathbf{k} -point set and the integrals (2.50) are calculated with this set. If a small number of \mathbf{k} -points is used within the Brillouin zone, a significant decreasing in the computational time can be achieved.

Pseudopotentials

DFT as described in the previous sections is computationally expensive for system sizes useful to model nanostructures. Using pseudopotentials is one significant way of achieving even more simplification of the system. It means that the core electrons are tightly bound to their host nuclei, and only the valence electrons are involved in chemical bonding. Therefore it is possible to incorporate the core states into a bulk nuclear potential and only deal with the valence electrons separately. The plane-wave basis set is not a good choice for describing electron wavefunctions since a preventively large number would be required to accurately describe the oscillations in the core regions which maintain orthogonality between valence and core electrons. This leads to an all-electron plane-wave calculation which is a huge computational expense. However understanding the electronic structure of the core-electrons be kept unchanged in different chemical environments and the problems relating to the core-electrons can be overcome by using a pseudopotential. [39, 40]

The pseudopotential approximation replaces the strong ionic potential $v_{ion}(\mathbf{r})$ in the core region, by a weaker pseudopotential $v_{ion}^{PS}(\mathbf{r})$. The corresponding set of pseudo-wavefunctions $\psi^{PS}(\mathbf{r})$ and the all-electron wavefunctions $\psi^{AE}(\mathbf{r})$ are identical outside a

chosen cutoff radius r_c and so exhibit the same scattering properties, but $\psi^{PS}(\mathbf{r})$ does not possess the nodal structure that cause the oscillations inside r_c , which means they can now be described with a reasonable number of plane-waves. A brief explanation of the pseudopotential concept is shown in Fig. (2.1)

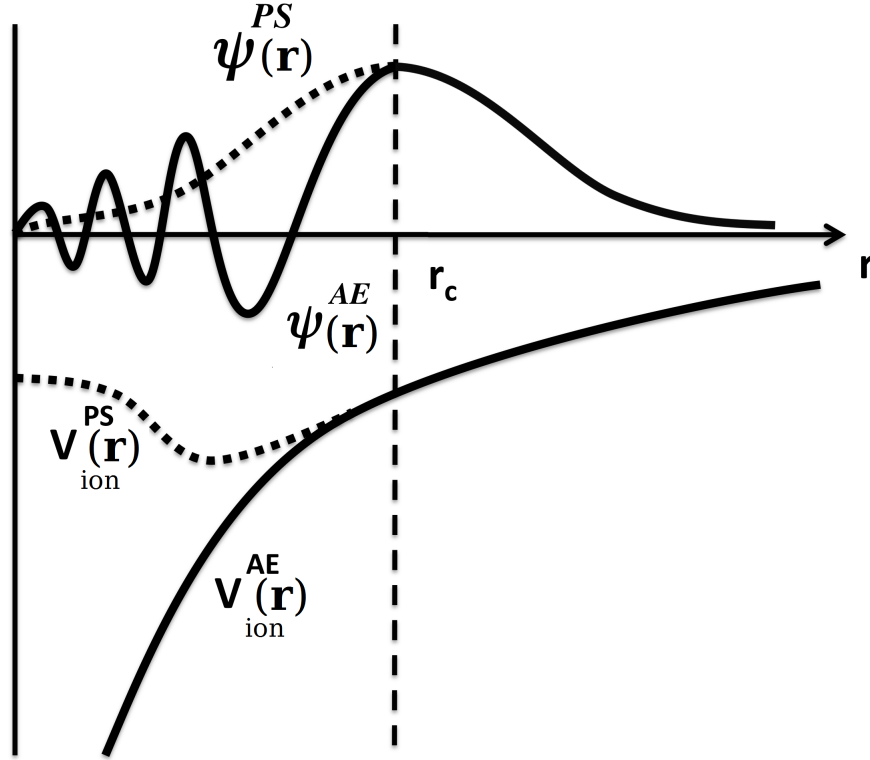


Figure 2.1: (Taken from Ref.[41]) Schematic illustration of the pseudopotential concept. The solid lines show the all-electron wavefunction, $\Psi^{AE}(\mathbf{r})$ and ionic potential, $v_{ion}^{AE}(\mathbf{r})$, while the dashed lines show the corresponding pseudo-wavefunction, $\Psi^{PS}(\mathbf{r})$, given by the pseudopotential, $v_{ion}^{PS}(\mathbf{r})$. All quantities are shown as a function of distance, \mathbf{r} , from the atomic nucleus. The cutoff radius r_c marks the point beyond which the all-electron and pseudo quantities become identical.

Pseudopotentials employed in this study

The ultrasoft pseudopotentials (US) were used in many pseudopotential calculations developed by Vanderbilt in the early 1990s [42]. These pseudopotentials reach to a much softer pseudo-wavefunction and employs fewer plane-waves for calculations of the same

accuracy. This is obtained with relaxing the norm-conservation constraint which has more flexibility in the construction of the pseudo-wavefunctions. In practice, generally the projector-augmented wave (PAW) potentials are more accurate than the ultra-soft pseudopotentials. [43, 44] Because first, the radial cutoffs are decreased comparing to the radii used for the US pseudopotentials, and second the PAW potentials reconstruct the exact valence wave function with all nodes in the core region. The disadvantages of using PAW instead of US are the required energy cutoffs and basis sets are also larger, since the core radii of the PAW potentials are smaller. If such a high precision is not required, the older US-PP can be used. The practical implementation of DFT, employed throughout this study, is mostly the Vienna ab initio Simulation Package (VASP)[45, 46], using PAW pseudo-potentials. [43] For the actual calculations in this thesis the GGA parametrization of Perdew, Burke and Ernzerhof[52] GGA is chosen for the exchange-correlation functional.

2.5.2 Augmented Plane Wave (APW) Method

An important example of a basis set is the augmented plane waves set (APW) proposed by Slater in 1937 [47]. This method has been one of the most popular methods for solving the electronic structure using the density-functional theory. But without doubt the single most important step was the linearization of the secular problem as proposed by Andersen[48].

In an APW descendent method, the space is divided into atomic centered spheres surrounded by an interstitial region. The APW basis functions consist of plane-waves in the interstitial region, augmented into radial solutions of the Schrödinger equation inside the Muffin-tin (MT) spheres. These radial functions u_l are better for describing the behavior of the Bloch eigen-functions close to atomic sites. For a system with one atom per unit cell this gives

$$\mathcal{X}_{\mathbf{G}}^{\text{APW}}(\mathbf{r}, \mathbf{k}) = \begin{cases} e^{i\mathbf{k}_{\mathbf{G}} \cdot \mathbf{r}} & \mathbf{r} \in \text{I} \\ \sum_L a_L^{\mathbf{k}_{\mathbf{G}}} u_l(r, E) Y_L(\hat{\mathbf{r}}) & \mathbf{r} \in \text{MT}, \end{cases} \quad (2.51)$$

where the MT is the Muffin-tin radius and the I is located in the interstitial region between the neighboring Muffin-tin regions, \mathbf{G} is a reciprocal lattice vector, \mathbf{k} is the crystal momentum and $\mathbf{k}_{\mathbf{G}} = \mathbf{k} + \mathbf{G}$ is the condensed angular momentum $\{l, m\}$ index and $Y_L(\hat{\mathbf{r}})$ are the spherical harmonics. The coefficients $a_L^{\mathbf{k}_{\mathbf{G}}}$ are found by expanding each planewave into Bessel functions $j_l(k_{\mathbf{G}} r)$ at the MT-spheres, $r = r_{\text{MT}}$ requiring the basis functions to be continuous at the sphere boundaries. This yields

$$a_L^{\mathbf{k}_{\mathbf{G}}} = 4\pi i^l Y_L^*(\hat{\mathbf{k}}_{\mathbf{G}}) \frac{j_l(k_{\mathbf{G}} r_{\text{MT}})}{u_l(r_{\text{MT}}, E)}. \quad (2.52)$$

The radial solutions u_l depend on the energy at which the radial Schrodinger equation is evaluated. An eigen-function $\Phi_i(\mathbf{r}) = \sum_{\mathbf{G}} C_{i\mathbf{G}} \mathcal{X}_{\mathbf{G}}(\mathbf{r}, \mathbf{k})$ can only be efficiently described by orbital solutions u_l evaluated at the eigen energy \mathcal{E}_i . A new set of APW

basis functions must therefore be evaluated for each new energy treated. As the matrix elements representing operators depend on the choice of basis set the secular equation,

$$\det[T_{\mathbf{G}\mathbf{G}'}(E) + V_{\mathbf{G}\mathbf{G}'}(E) - E\mathcal{O}_{\mathbf{G}\mathbf{G}'}(E)] = 0, \quad (2.53)$$

will be non-linear in energy. $T_{\mathbf{G}\mathbf{G}'}$ represents the kinetic energy operator, $V_{\mathbf{G}\mathbf{G}'}$ is the potential energy and $\mathcal{O}_{\mathbf{G}\mathbf{G}'}$ the overlap matrix. The procedure of evaluating the determinant for a number of different energies in order to find the energy eigenvalues makes the APW method very time consuming. Another problem is the decoupling of the basis set for energies yielding $u_l = 0$ at the MT-sphere boundary, but this is of less importance.

Linear Augmented Plane Wave (LAPW) Method

A great simplification was introduced with the so-called linear augmented plane wave (LAPW) method. In this approximation, the non-linear eigenvalue problem is overcome by performing a Taylor expansion of the radial wave function around some fixed energy. If the basis functions, and thereby the matrix elements $T_{\mathbf{G}\mathbf{G}'}$, $V_{\mathbf{G}\mathbf{G}'}$ and $\mathcal{O}_{\mathbf{G}\mathbf{G}'}$, were energy independent, the secular equation Eq. (2.53) would turn into a general eigenvalue problem. All eigen energies could then be found by diagonalizing the secular matrix once. However, such an energy independent basis set must be able to describe all eigenfunctions of the different eigen energies.

By introducing the energy derivatives $\dot{u}_l \equiv \partial u_l / \partial E$ of the radial solutions u_l , Andersen constructed an energy independent LAPW basis set [48],

$$\mathcal{X}_{\mathbf{G}}^{\text{LAPW}}(\mathbf{r}, \mathbf{k}) = \begin{cases} e^{i\mathbf{k}\mathbf{G}\cdot\mathbf{r}} & \mathbf{r} \in \text{I} \\ \sum_L R_L^{\text{LAPW}}(r) Y_L(\hat{\mathbf{r}}) & \mathbf{r} \in \text{MT} \end{cases} \quad (2.54)$$

where $R_L^{\text{LAPW}}(r) = a_L^{\mathbf{k}\mathbf{G}} u_l(r, \mathcal{E}_1) + b_L^{\mathbf{k}\mathbf{G}} \dot{u}_l(r, \mathcal{E}_1)$. The $\mathcal{X}_{\mathbf{G}}^{\text{LAPW}}$ provides a sufficient basis for eigen-functions in an energy range around the linearization energy \mathcal{E}_1 . The two coefficients $a_L^{\mathbf{k}\mathbf{G}}$ and $b_L^{\mathbf{k}\mathbf{G}}$ are determined by forcing each basis function to be continuously differentiable, i.e. continuous with continuous first derivative, at the surfaces of the MT-spheres.

2.5.3 Spin Systems

Collinear Spin System

In order to treat spin systems, the total electron density needs to be separated into the spin-up and spin-down components. A formalism to handle spin systems can be extended which has been done by von Barth and Hedin [49] in the spin-density functional theory. Formally, this is done by replacing the density $n(\mathbf{r})$ by an generalized density matrix:

$$\rho(\mathbf{r}) = \frac{n(\mathbf{r})}{2} \mathbf{1} + \frac{\mathbf{m}(\mathbf{r})}{2} \cdot \boldsymbol{\sigma} \quad (2.55)$$

Here $\mathbf{1}$ is the 2×2 unit matrix, $\mathbf{m}(\mathbf{r})$ the magnetization density and $\boldsymbol{\sigma} = (\sigma_x, \sigma_y, \sigma_z)$ are the Pauli spin matrices.

2 Theoretical Background

In fact each one-electron state is represented as a spinor function:

$$\psi_i(\mathbf{r}) = \begin{pmatrix} \alpha_i(\mathbf{r}) \\ \beta_i(\mathbf{r}) \end{pmatrix}, \quad (2.56)$$

where α_i and β_i are the two spin projections. Moreover, all operators need to be represented as 2×2 matrices. The explicit form of the charge and magnetization density is then:

$$n(\mathbf{r}) = \sum_{i=1}^N |\psi_i(\mathbf{r})|^2, \quad \text{and} \quad \mathbf{m}(\mathbf{r}) = \sum_{i=1}^N \psi_i^\dagger(\mathbf{r}) \boldsymbol{\sigma} \psi_i(\mathbf{r}), \quad (2.57)$$

and the density matrix has the form:

$$\rho(\mathbf{r}) = \sum_{i=1}^N \begin{pmatrix} |\alpha_i(\mathbf{r})|^2 & [\alpha_i^*(\mathbf{r})\beta_i(\mathbf{r})]^* \\ [\alpha_i^*(\mathbf{r})\beta_i(\mathbf{r})] & |\beta_i(\mathbf{r})|^2 \end{pmatrix}. \quad (2.58)$$

In the case of collinear spin system, a unique global magnetization axis can be defined in, for instance, the z-direction. Then the density matrix and operators reduce to diagonal form. The two spin projections have different potentials and can be solved independently of each other and the density matrix is completely described by the scalar quantities $n = n_\uparrow + n_\downarrow$ and $m_z = n_\uparrow - n_\downarrow$.

Non-collinear Spin System

A global spin quantization axis does not exist in a collinear system while it does for a non-collinear spin system[50]. In the non-collinear magnetic system the spinor formalism should be kept and we should work with 2×2 matrices for the operators. Considering inter-non-collinearity, that is, within each muffin-tin sphere there is a unique quantization axis (which is not equal for different spheres) is an approximation, which can be lifted by treating the magnetization density as a vector field. A local frame of reference defined by the Euler angles θ_ν and ϕ_ν with respect to some global frame of reference, is then introduced in each sphere labeled by ν so the density matrix and effective potential matrix are diagonal in that local frame. By using the standard spin- $\frac{1}{2}$ rotation matrix [51]:

$$\mathbf{U}(\theta, \phi) = \begin{bmatrix} \cos\left(\frac{\theta}{2}\right) \exp\left(\frac{i\phi}{2}\right) & \sin\left(\frac{\theta}{2}\right) \exp\left(-\frac{i\phi}{2}\right) \\ -\sin\left(\frac{\theta}{2}\right) \exp\left(\frac{i\phi}{2}\right) & \cos\left(\frac{\theta}{2}\right) \exp\left(-\frac{i\phi}{2}\right) \end{bmatrix}, \quad (2.59)$$

the effective potential matrix in the global frame of reference can be obtained by an unitary transformation:

$$\mathbf{v}_{eff}(\mathbf{r}) = \mathbf{U}^\dagger(\theta, \phi) \begin{bmatrix} v_{eff}^\uparrow(\mathbf{r}) & 0 \\ 0 & v_{eff}^\downarrow(\mathbf{r}) \end{bmatrix} \mathbf{U}(\theta, \phi) \quad (2.60)$$

Here $v_{eff}^\uparrow(\mathbf{r})$ and $v_{eff}^\downarrow(\mathbf{r})$ are the components of the effective potential matrix in the local frame of reference. Now the solution to the Kohn-Sham equation can be obtained as discussed earlier, in previous sections.

2.6 Spin System at finite temperature

2.6.1 Classical Heisenberg model

Many aspects of magnetic behavior involve magnetic moments that are strongly coupled. A model that captures the physics of such systems is the so called classical Heisenberg spin model. This model consists of interacting spins on lattice sites, \mathbf{S}_i , with \mathbf{S} denoting a spin variable and i the lattice point where it resides. A pair of spins at lattice sites i and j interact by the so called exchange term J_{ij} , which depends on the relative distance between the spins. The classical Heisenberg spin model Hamiltonian is:

$$H = - \sum_{i \neq j} J_{ij} \mathbf{S}_i \cdot \mathbf{S}_j \quad (2.61)$$

where J_{ij} are exchange interactions between atom i and j whose moments lie in the direction of the unit vectors \mathbf{S}_i and \mathbf{S}_j , respectively. The magnetic moments are included in J_{ij} . If the exchange constant J_{ij} is positive, then the model describes ferromagnetic order because the spins will tend to be oriented in the same direction to give a positive value for $J_{ij} \mathbf{S}_i \cdot \mathbf{S}_j$, as this minimizes the energy. In the opposite case, a negative value for J will lead to antiferromagnetic order, where nearest neighbor spins will tend to be oriented in opposite directions.

Anisotropic Heisenberg model

One may note that in the case of ferromagnets the above Heisenberg Hamiltonian predicts the parallel alignment of atomic spins, but does not specify a preferential direction of alignment. Thus in such case the Heisenberg Hamiltonian is called the isotropic Heisenberg Hamiltonian. However, in real solids the isotropy is broken by decreasing dimensions of the system (i.e. from bulk to surface) or other magnetic effects that were neglected in the original Hamiltonian, like the dipolar interactions and spin-orbit coupling. Also an external magnetic field can be applied so that the isotropy is broken by introducing a certain direction (the direction of the field). Then the anisotropic Heisenberg Hamiltonian is written as:

$$H = - \sum_{i \neq j} J_{ij} \mathbf{S}_i \cdot \mathbf{S}_j - K \sum_i (S_i^z)^2 - \mu_s \mathbf{B} \cdot \sum_i \mathbf{S}_i \quad (2.62)$$

where K is the uniaxial anisotropy constant represents the on-site anisotropy. μ_s is the absolute value of the magnetic moment which for an atomic moment is of the order of a Bohr magneton. The external magnetic field, \mathbf{B} , can be applied in any relative orientation with respect to the axis of anisotropy.

2.6.2 Monte Carlo method

Monte Carlo simulations is one of the main approaches in computer simulations. Because of its confidence on reiterated computation of random numbers, this method is

very suited to calculation by a computer and tend to be used when it is unfeasible or impossible to compute an exact result with a deterministic algorithm. The aim of using this method is to study equilibrium and non equilibrium thermodynamic systems by stochastic computer simulations. Computer simulations allow for studies of complex systems where analytical solutions are not possible. Computer simulations have some advantages in experiments, for instance one can calculate and study properties that are difficult to obtain in experiments, for example, correlations between different atoms.

Monte Carlo (MC) simulations in statistical physics is based on the use of random numbers to generate a stochastic trajectory through the phase space of the model considered, and to calculate thermal averages if equilibrium properties are desired. The first simulation was carried out by Metropolis *et al.* [52] in 1953. It is possible to perform simulations of good quality even on personal computers but in the case of required high accuracy and/or large systems the simulations have to be performed on supercomputers. MC simulations can be applied to many fields like: diffusion processes in solids, fluid, surface and plasma physics, properties of alloys, crystal growth kinetics, quantum many-body problems, critical phenomena in magnetic systems, kinetics of adsorption on surfaces and thermal properties of disordered systems. For a more complete survey of MC simulations in statistical physics, see Refs. [53, 54].

Random Number Generators

The basic random number generators make floating point or integer random numbers with uniform distributions. It is very important to use random numbers with high quality in order to perform an accurate MC simulations. A digital computer can only produce pseudo random numbers which are generated in the computer by some suitable algorithm, for instance, linear congruential method, shift register methods and lagged Fibonacci generators. Since the sequence is started with a seed, these pseudo random number sequences are exactly reproducible. There are some requirements on the pseudo random numbers: they must be uniformly distributed in the interval $[0,1]$, the sequence must be as less correlated as possible and they must be generated fast. A limitation due to the finite word length of computers is that the pseudo random numbers have a finite period. For instance, on a 32-bit processor the period is $2^{31} \approx 10^9$ numbers only.

Thermodynamic Averages

A thermodynamic quantity can be averaged over by the values for the sequence of states generated in the MC simulations. Usually, a number of Monte-Carlo steps before starting to do any averaging is carried out. This is to guarantee that the system is in thermodynamic equilibrium while the averaging is carried out. The magnetic field \mathbf{B} can also be included as a additional thermodynamic coordinate. Now each particle i is described by a set of dynamical variables which is spin of particle i in our system. $\{S_i\}$ corresponds to the spin vector \mathbf{S}_i . Let \mathbf{S}_ν be a point in phase space Ω . Then \mathbf{S}_ν becomes:

2 Theoretical Background

$$\mathbf{S}_\nu = \{\{S_1\} \{S_2\}, \dots, \{S_N\}\}, \quad (2.63)$$

where \mathbf{S}_ν fully describes the configuration of the system. The interactions between the particles are described by a Hamiltonian, $H(\mathbf{S}_\nu)$. The probability density P_{eq} of the point \mathbf{S}_ν to lay in a differential volume element is given in equilibrium statistical mechanics as:

$$P_{\text{eq}}(\mathbf{S}_\nu) = \frac{1}{Z} \exp[-H(\mathbf{S}_\nu)/k_B T] \quad (2.64)$$

where Z is the partition function, k_B Boltzmann's constant and T the temperature. $A(\mathbf{S}_\nu)$ denotes a thermodynamic observable. The thermal average of $A(\mathbf{S}_\nu)$ is obtained by [55]:

$$\langle A \rangle_T = \frac{1}{Z} \int_{\Omega} d\mathbf{S}_\nu A(\mathbf{S}_\nu) \exp[-H(\mathbf{S}_\nu)/k_B T] \quad (2.65)$$

Importance Sampling and Metropolis Algorithm

Many functions have a pronounced weight in some specific regions. For example, most of the contributions to an integral of a simple Gaussian are located near the central peak. In a simple Monte Carlo integration scheme, points are sampled uniformly, wasting considerable effort sampling the tails of the Gaussian. Techniques for overcoming this problem act to increase the density of points in regions of interest and hence improve the overall efficiency. These techniques are called importance sampling. Calculation the phase space integrals in Eq. (2.65) is main idea behind MC simulations. Using standard numerical integration methods lead to the high dimensionality of the integration space Ω . Another problem is that the exponential factor (Boltzmann factor) in Eq. (2.64) and Eq. (2.65) is almost vanishingly small for most of the configurations. This means that a very few number of configurations will contribute to the expectation value of A . Metropolis et al. [52] introduced in 1953 a sampling algorithm. In this algorithm a configuration \mathbf{S}_ν is not chosen completely at random but with a probability $P_{\text{eq}}(\mathbf{S}_\nu)$ that is proportional to its Boltzmann factor. Then the average of A over M phase space points \mathbf{S}_ν :

$$\langle A \rangle \approx \bar{A} = \frac{\sum_{\nu=1}^M \exp[-H(\mathbf{S}_\nu)/k_B T] A(\mathbf{S}_\nu) P^{-1}(\mathbf{S}_\nu)}{\sum_{\nu=1}^M \exp[-H(\mathbf{S}_\nu)/k_B T] P^{-1}(\mathbf{S}_\nu)} \quad (2.66)$$

reduces to a simple arithmetic average:

$$\langle A \rangle = \frac{1}{M} \sum_{\nu=1}^M A(\mathbf{S}_\nu) \quad (2.67)$$

The probability $P_{\text{eq}}(\mathbf{S}_\nu)$ is not explicitly known though. This was solved by Metropolis who proposed a method to generate a sequence of states $\mathbf{S}_\nu \rightarrow \mathbf{S}_{\nu+1} \rightarrow \mathbf{S}_{\nu+2} \rightarrow \dots$, where each step has a transition probability $W(\mathbf{S}_\nu \rightarrow \mathbf{S}_{\nu+1})$. This kind of sequence is

2 Theoretical Background

called a Markov chain. From the theory of Markov chains in probability theory, one can show that $P(\mathbf{S}_\nu) \rightarrow P_{\text{eq}}(\mathbf{S}_\nu)$ as $M \rightarrow \infty$, if the condition of detailed balance is fulfilled:

$$P_{\text{eq}}(\mathbf{S}_\nu)W(\mathbf{S}_\nu \rightarrow \mathbf{S}_{\nu'}) = P_{\text{eq}}(\mathbf{S}_{\nu'})W(\mathbf{S}_{\nu'} \rightarrow \mathbf{S}_\nu) \quad (2.68)$$

A simple choice for W fulfilling the above condition is given in terms of the energy change $\Delta E = H(\mathbf{S}_{\nu'}) - H(\mathbf{S}_\nu)$, as proposed by Metropolis:

$$W(\mathbf{S}_\nu \rightarrow \mathbf{S}_{\nu'}) = \begin{cases} 1 & \Delta E < 0 \\ \exp(-\Delta E/k_B T) & \Delta E > 0 \end{cases} \quad (2.69)$$

Calculation of the Critical Temperature

The critical temperatures of the magnetic phase in system can be modeled by the classical Heisenberg model Eq. (5.2). The average magnetization and magnetic susceptibility and specific heat can be obtained from the expectation values as,

average magnetization \mathbf{M} ,

$$\mathbf{M} = \frac{1}{N} \sum_{i=1}^N \mathbf{S}_i, \quad (2.70)$$

magnetic susceptibility χ ,

$$\chi = \frac{N^2}{k_B T} \left(\langle \mathbf{M}^2 \rangle - \langle \mathbf{M} \rangle^2 \right), \quad (2.71)$$

and specific heat C_v ,

$$C_v = \frac{N^2}{k_B T^2} \left(\langle E^2 \rangle - \langle E \rangle^2 \right), \quad (2.72)$$

With analyzing the dependence of specific heat C_v and magnetic susceptibility χ to the temperature the critical point of a phase transition can be determined. Working with the specific heat can be more difficult because it incorporates the effect of all the terms contributing to the Hamiltonian (the Hamiltonian we considered is rather more simple with only magnetic contribution), susceptibility analysis would give information about the magnetic critical temperature. In the Hamiltonian considered in this thesis, both the specific heat and the magnetic susceptibility are studied.

3 Properties of the Cu substrate

Electronic structure calculations are widely applied to the complex systems such as nanostructured metals. But, it is fundamentally important to correctly determine the basic properties of the system under study. For instance, in nanostructures such as self assembled monolayers or atomic islands grown on a metal substrate, the underlying metal work function and Fermi energy are crucial to determine interfacial phenomena.[56] Thus, a clear understanding of the fundamental properties of the surfaces is essential. Here, the physical properties such as surface energies, structural relaxations, and work functions of the Cu(111) surface have been studied within the framework of DFT.

This section is organized as follows: In the next section, the computational details are described. Then, the bulk properties are discussed, as well as comparison with the experimental results. Subsequently, the relaxations, surface energy, and work function of the Cu(111) surface are calculated.

Methodology

The calculations are performed within the framework of spin-polarized density functional theory, using the Vienna ab initio simulation package (VASP) [45, 46]. The frozen-core full-potential projector augmented-wave method (PAW) is used [43], applying the generalized gradient approximation of Perdew and Wang (PW91-GGA) [57].

In fact, the VASP with the PAW method and the PW91-GGA functional are employed for the most of the calculations reflected throughout this thesis. To avoid repetitions, this fact will not be mentioned anymore, unless a different method is used.

The cutoff energy of 270 eV for the plane wave basis sets is applied. A Gaussian smearing ($\sigma = 0.1$ eV) of the eigenstates is used to improve convergence. Structural relaxations are performed using the conjugate gradient algorithm, and stopped when the forces acting on all the unconstrained ions dropped below 0.01 eV/Å. During structural relaxations, the bottom three layers of the six-layer slab are fixed at their ideal bulk positions. The system itself is modelled by six layers of Cu separated by 15Å of vacuum. The convergence of the calculated properties with respect to number of k-points and supercell size was carefully checked. A $(21 \times 21 \times 21)$ k-points mesh is used for the integration over the Brillouin zone for the bulk Cu.

3.1 Properties of Cu bulk crystals

A surface is directly connected to the underlying bulk, which means that the properties of the bulk material will most probably influence the properties and behavior of the

3 Properties of the Cu substrate

Table 3.1: Calculated lattice parameters and bulk moduli of Cu considered in this study compared with experimental values. Refs: (a) Present study, (b) [59], (c) [60]

	a_0 (Å)	B_0 (Mbar)	E_{coh} (eV)
GGA	3.633 ^a	1.51 ^a	-3.30 ^a
Exp.	3.61 ^b	1.37 ^c	-3.49 ^c

surface. This chapter is therefore devoted to the investigation of the bulk structure, in order to study its equilibrium atomic structure, relative stability, electronic properties. The results are then used to obtain the surface energy and formation energy of films at the surface. Additionally, it is the basis for comparing the theoretical results with experimental data. The starting point of any investigation is the determination of the theoretical lattice parameter.

The lattice parameters and bulk moduli for Cu have been calculated. The calculations are performed for the total energy of the bulk system for a range of lattice parameters a . The total energy data are fit with the Murnaghan equation of state [58] to obtain the bulk moduli. The volumes at zero pressure (equilibrium volume), bulk moduli calculated at the equilibrium volume, and the cohesive energies are obtained using Murnaghans equation of state,

$$E(V) = E_0 + \frac{B_0 V}{B'_0} \left(\frac{(V_0/V)^{B'_0}}{B'_0 - 1} + 1 \right) - \frac{B_0 V_0}{B'_0 - 1} \quad (3.1)$$

where V_0 is the equilibrium volume at zero temperature, $E(V_0)$ is the minimum energy of the system, B_0 is the bulk modulus, defined as

$$B_0 = -V \left(\frac{\partial P}{\partial V} \right)_T. \quad (3.2)$$

The cohesive energy of a bulk material is the energy which is required to break the atoms of the bulk material into isolated atomic species, i.e,

$$E_{coh} = E_{bulk} - \sum_n E_n^{isolated} \quad (3.3)$$

where n represents the number of different atoms that constitute the bulk. The bulk cohesive properties calculated with the GGA functional, as well as experimental results are summarized Table (3.1).

Electronic properties

The calculated density of states (DOS) and band structure for GGA functional at its equilibrium volume are shown in Fig. (3.1) and Fig. (3.2), subsequently. The DOS and band structure of Cu bulk are calculated in order to document the performance of our

numerical approximations and to compare the obtained results with different choices for the exchange-correlation functionals such as LDA, GGA. However the LDA DOS and band structure are not shown here, but, using this exchange-correlation functional leads to a visually similar to GGA DOS and band structure, as reported in Ref. [61]. The LDA tends to over-bind the system resulting in a somewhat lower lattice constant. There are numerous publications on the Cu band structure (Ref. [62] and references therein) it is well-known that the structure and energetics of the Cu bulk crystal are best described within the GGA.

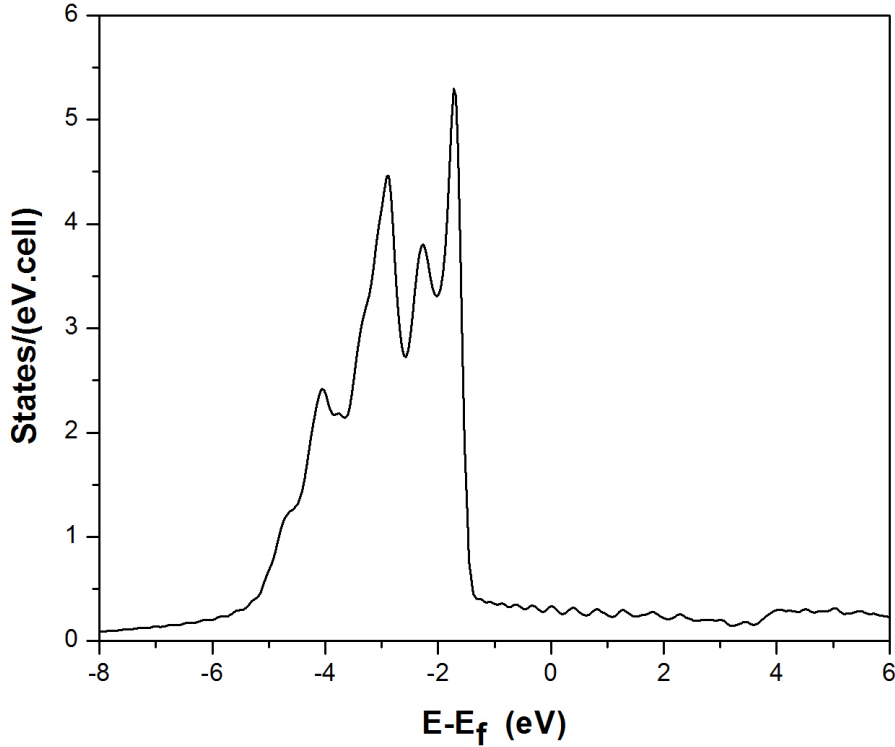


Figure 3.1: Density of states of bulk Cu at equilibrium volume with a $(21 \times 21 \times 21)$ k-point grid in the Brillouin-Zone using GGA functional. The Fermi energy defines the zero point on the energy scale.

3.2 Cu(111) surface

3.2.1 Surface relaxation

The interlayer relaxation is one of the surface properties which is accessible experimentally. The atomic structure can be obtained with high accuracy using quantitative low-energy electron diffraction (LEED) intensity analysis [63, 64]. First-principles calculations also give an accurate description [65, 66, 67, 68]. Surface relaxations can arise from the creation of a new surface which leads to a smoothing of the charge density at

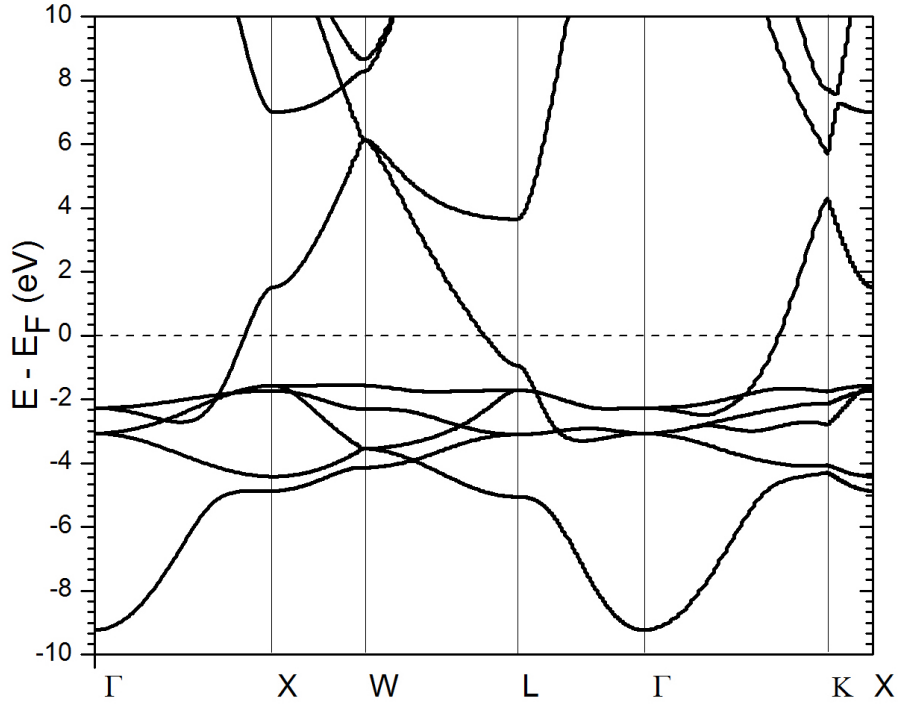


Figure 3.2: Band structure of face center cubic copper at equilibrium volume using GGA functional, plotted along the Γ –X in the Brillouin zone. The Fermi energy defines the zero point on the energy scale.

the newly formed surface, which causes a net force on the outermost surface layer of ions pointing into the bulk. It is assumed that a pure unit cell of the unreconstructed surface, using a slab supercell model, within DFT calculations, can be effectively used to study these surface layer relaxations.

In Table (3.2), the top three surface layer relaxations for 6-layer slab Cu(111) are shown. As expected, the relaxation of the surface layers is related to the density of packing, with larger relaxation for the less-densely packed surfaces, with patterns of multilayer relaxation that become noticeable. Comparison to low-energy electron diffraction (LEED) experimental values shows that our values are in agreement with the experimentally observed values. Surface relaxation is characterized as the percent change Δd_{ij} of the spacing between layers i and j versus the equilibrium layer spacing d_0 . For the (111) surface d_0 is $a_0/\sqrt{3}$.

3.2.2 Surface energy

As mentioned earlier, it is important to have a clear understanding of the fundamental properties of the metal surfaces such as work functions. Since the mentioned physical properties play a role in determining the behavior of solid metal surfaces when used in various applications. The direct experimental measurements of the surface energy are

3 Properties of the Cu substrate

Table 3.2: Surface relaxations for the top three layers. Reported are the values for a 6-layer slabs, compared to experimental values from the literature. Refs: (a) Present study, (b) [69]

Surface	$\Delta d_{12}(\%)$		$\Delta d_{23}(\%)$		$\Delta d_{34}(\%)$	
	GGA	Exp.	GGA	Expt.	GGA	Exp.
(111)	-0.8^a	-0.7 ± 0.5^b	-0.58^a	-	-0.15^a	-

difficult to perform and subject to various uncertainties, e.g., presence of impurities. In addition, in most of the experiments, a surface tension measurement in the liquid phase should be done to extrapolate to zero temperature [70], which does not provide the orientation dependence of the surface energy. Therefore an accurate first-principle calculation plays an important role. The surface energy is the energy required to create a new surface, and as mentioned earlier, it is difficult to determine it experimentally. In our calculations the surface energy σ can be determined by taking the energy difference between the total energy of a slab and an equivalent bulk reference amount, as seen in the following expression [71]:

$$\sigma = \lim_{N \rightarrow \infty} \frac{1}{2} (E_{\text{slab}}^N - N E_{\text{bulk}}) \quad (3.4)$$

where E_{slab}^N is the total energy of an N-atom slab, E_{bulk} is the total energy of the bulk per atom, and the factor $\frac{1}{2}$ accounts for the two surfaces in the slab unit-cell. In the limit of large N , one can rewrite Eq. (3.4) as:

$$E_{\text{slab}}^N \approx 2\sigma + N E_{\text{bulk}} \quad (3.5)$$

If the total energy of the slab depends linearly on slab thickness N , the bulk energy term E_{bulk} can be taken as the slope and used in Eq. (3.4), thereby avoiding a calculation on a separate bulk system. In practice, it has been shown that divergence can be avoided when large and matching \mathbf{k} -point samplings are used for the slab and bulk calculations.[72]

Table 3.3: Surface energies for 6-layer slabs in fully relaxed geometries reported here in (eV/atom). Experimental values compared with the surface energy of the relaxed surfaces reported here in units of (J/m²). Refs: (a) Present study, (b) [70]

Surface	σ (eV/atom)	σ (J/m ²)	$\sigma_{Exp.}$ (J/m ²)
Cu (111)	0.71^a	1.95^a	1.83^b

The surface energies, the theoretical as well as the experimental values, are summarized in Table (3.3).

Table 3.4: Work functions calculated for 6-layer slabs of Cu(111) surface. All values in eV.

	Surface	Φ	$\Phi_{Exp.}$
Cu	(111)	4.82	4.94

3.2.3 Work function

The work function is the minimum energy (usually measured in electron volts) needed to remove an electron from the bulk of a material through a surface to a point outside the material. In principle, this is the energy required at 0 K to remove an electron from the Fermi level of the metal to the vacuum potential. Calculations of work function using DFT employ this definition and determine the Fermi energy and vacuum potential from calculations of the metals in slab-supercell geometries.

The minimum energy needed to remove an electron from the bulk of a material through a surface to a point outside the material can be written as:

$$\Phi = V_{\text{vacuum}} - E_F. \quad (3.6)$$

Note here that the window for macroscopic averaging is the unrelaxed equilibrium layer spacing. All of the potentials discussed here (both from the slab and the bulk reference) refer to the electrostatic part of the total potential. This part of the potential tails off more rapidly in the vacuum region of the slab-supercell when compared to the full Kohn-Sham potential including the exchange-correlation potential.

The calculated work functions of Cu(111) slabs are presented in Table (3.4), along with experimental values. In general the results for the work function are in good agreement with experimental values.

3.2.4 Surface states

The electronic states localized at the surface of the solids are called surface states. They are created due to the sharp transition from solid material that terminates with a surface and are found only at the atom layers closest to the surface. The electronic band structure is changed from the bulk material to the vacuum, due to the termination of a material with a surface. In the weakened potential at the surface (see Fig. 3.3), new electronic states can be formed.

As discussed in Sec. (2.5.1), solutions of the Schrödinger equation with a periodic potential are Bloch waves. $\psi_{j,\mathbf{k}}(\mathbf{r})$ is a function with the same periodicity as the crystal, j is the band index and \mathbf{k} is the wave number. By applying the Born–von Karman cyclic boundary conditions, these allowed wave numbers for a given potential can be obtained.[60] At the surface, the termination of a crystal causes deviation from perfect periodicity. Consequently, in the direction normal to the surface, solutions of the

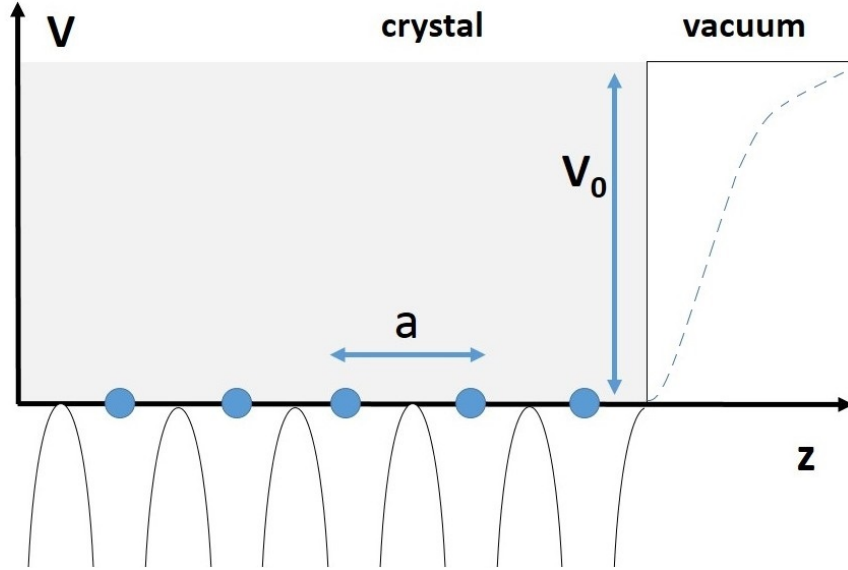


Figure 3.3: Schematic model of a one dimensional periodic crystal potential terminating at an ideal surface. The potential jumps to the vacuum at the surface. The dashed line represents the potential reaching the vacuum level over some distance. a is the lattice parameter of the crystal, V_0 is the height of the finite step potential and V is the potential.

Schrödinger equation will be changed. Since, the cyclic boundary conditions are abandoned. A simplified model of the crystal potential in one dimension can be sketched as shown in Fig. 3.3. The potential jumps to the vacuum value at the surface. The dashed line represents the exponentially decaying tail of the potential which reaches into the vacuum.

Surface states in metals

A semi-infinite periodic chain of identical atoms can be modeled to derive the basic properties of states at a metal surface.[73] The termination of this atomic chain represents the surface, where the potential attains the value V_0 of the vacuum in the form of a step function. (See Fig. 3.3) Within the crystal the potential is assumed periodic with the periodicity a of the lattice. The Shockley states [74] are then found as solutions to the one-dimensional single electron Schrödinger equation:

$$\left[-\frac{\hbar^2}{2m} \frac{d^2}{dz^2} + V(z) \right] \Psi(z) = E\Psi(z), \quad (3.7)$$

with the periodic potential:

$$V(z) = \begin{cases} V(z + la) & \text{for } z < 0 \\ V_0 & \text{for } z > 0 \end{cases}, \quad (3.8)$$

where l is an integer. The solution must be obtained independently for the two domains $z < 0$ and $z > 0$, where at the domain boundary ($z=0$) the usual conditions on continuity of the wave function and its derivatives is applied. Since the potential is periodic deep inside the crystal the electronic wave functions must be Bloch waves. The solution in the crystal is then a linear combination of an incoming and a wave reflected from the surface. For $z > 0$ the solution will be required to decrease exponentially into the vacuum:

$$\Psi(z) = \begin{cases} Bu_{-k}e^{-ikz} + Cu_k e^{ikz} & \text{for } z < 0 \\ A \exp\left[-\sqrt{2m(V_0 - E)}\frac{z}{\hbar}\right] & \text{for } z > 0 \end{cases}, \quad (3.9)$$

The wave function for a state at a metal surface is qualitatively shown in Fig. 3.4. It is an extended Bloch wave within the crystal with an exponentially decaying tail outside the surface. The consequence of the tail is a deficiency of negative charge density just inside the crystal and an increased negative charge density just outside the surface, leading to the formation of a dipole double layer. The dipole perturbs the potential at the surface leading, for example, to a change of the metal work function.

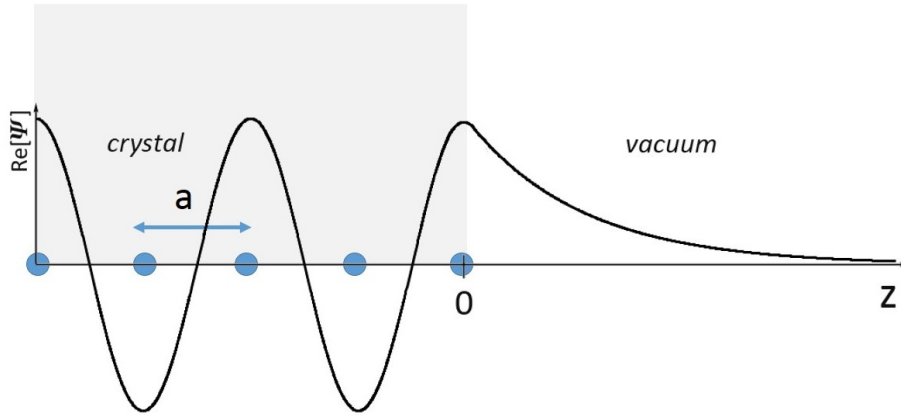


Figure 3.4: Real part of solution to the one-dimensional Schrödinger equation, which corresponds to the bulk states. These solutions are Bloch-like waves in the bulk, while decaying exponentially into the vacuum.

Surface states of a three-dimensional crystal

The solutions (surface states) obtained for an atomic linear single chain can be generalized to a three-dimensional crystal case. [73] Due to the fact that, the two-dimensional periodicity of the surface lattice Bloch's theorem applies for translations parallel to the surface. This would lead to the surface states which are written as the product of Bloch waves with $\mathbf{k}_{\parallel} = (k_x, k_y)$ parallel to the surface and a function representing a one-dimensional surface state

$$\Psi_0(\mathbf{r}) = \psi_0(z)u_{\mathbf{k}_{\parallel}}(\mathbf{r}_{\parallel})e^{-i\mathbf{r}_{\parallel}\cdot\mathbf{k}_{\parallel}}, \quad (3.10)$$

The energy of this state is increased by a term \mathbf{E}_{\parallel} , therefore, we have:

$$E_s = E_0 + \frac{\hbar^2 \mathbf{k}_{\parallel}^2}{2m^*}, \quad (3.11)$$

where m^* is the effective mass of the electron. The matching conditions at the crystal surface, i.e. at $z=0$, have to be satisfied for each \mathbf{k}_{\parallel} separately and for each \mathbf{k}_{\parallel} a single, but generally different energy level for the surface state is obtained.

Surface states of Cu(111)

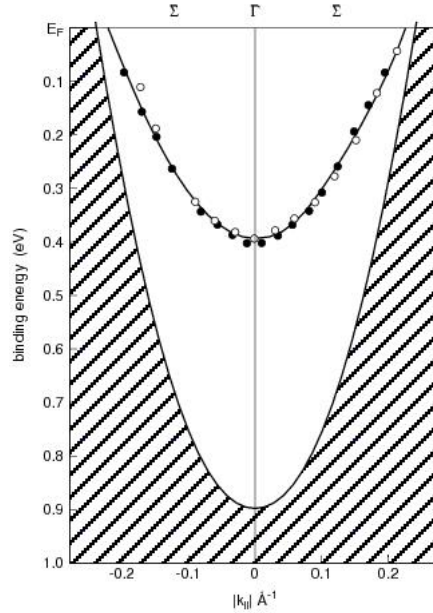


Figure 3.5: (Taken from Ref. [75]) Energy dispersion relation for the surface state. The solid curve is a parabolic least-squares fit. The shaded region is the projected bulk continuum of states. Note that the surface state enters the bulk continuum just above the Fermi level.

The experimentally measured surface state of Cu(111) residing in the projected band gap around the centre of the surface Brillouin zone is shown in Fig. 3.5. It shows the dispersion relation $E(\mathbf{k}_{\parallel})$ of the surface state along with the projected bulk continuum. The upper limit of this continuum was calculated with the assumption of a parabolic fit to Fermi surface data. The same assumption is made regarding the parabolic fitting for the VASP and Korringa–Kohn–Rostoker (KKR) method's [76, 77] projected band structure

3 Properties of the Cu substrate

calculations. To model a surface, KKR takes a semi-infinite number of layers (which represents the crystal). This is the advantage of KKR over VASP. As we will discuss in details below, an accurate description of the surface and its scattering properties can be provided by taking a semi-infinite number of layers. As already discussed, break of the crystal symmetry at a surface changes the spectrum and causes additional bands to appear in the gaps of the (111) projected bulk band structure. States described by such bands are confined at the surface in between the vacuum potential barrier on the one, and the crystal band gap on the other side. [78] The dispersion of such surface states depends on the type and the position of the gap. The surface state arising in the inverted L -gap of the bulk Cu is 2D free-electron like and is described by a parabolic dispersion relation.[79]

Two-dimensional band structures of 6, 12, 18 and 24 layer slab of Cu(111) and the projected bulk band structure are calculated using VASP. The energy bands of a 24 layer slab and corresponding projected bulk band structure are presented in Fig. (3.6). The results of 6, 12 and 18 layer slab calculations are also shown and compared with the KKR calculated spectral density map in Fig. (3.7.(d)). This is a considerable fact that only considering 18 layer slab of Cu or more (24 layer slab) produces the band structures which are comparable to experimental energy dispersion (Fig. (3.5)) or KKR spectral density map (Fig. (3.7)).

The calculated values of m^* , \mathbf{k}_{\parallel} and E_0 for Cu(111) surface, respectively for 6, 12 and 18 layers of Cu, are summarized in Tab. 3.5. Therefore, in order to obtain the surface states bands using a DFT slab model, the number of layers should be increased. There is a separation between band 1 and band 2 in the band structure, as one can see the results in the Tab. (3.5) or visually observe in Fig. (3.7.(a,b and c)), but due to increasing the number of layers, these two bands come together and the separation disappears.

Table 3.5: Calculated values of m^* , \mathbf{k}_{\parallel} and E_0 for Cu(111) surface. Refs: (a) Present work, (b) Ref. [75]

	Band 1			Band 2		
	E_0 (meV)	m^*/m_0	\mathbf{k}_{\parallel} (1/Å)	E_0 (meV)	m^*/m_0	\mathbf{k}_{\parallel} (1/Å)
6 layers ^a	772	0.528	0.336	274	0.344	0.162
12 layers ^a	519	0.385	0.235	432	0.328	0.198
18 layers ^a	455	0.339	0.207	473	0.356	0.216
KKR ^b	511	0.357	0.236	511	0.357	0.236
<i>Exp.</i> ^b	435	0.412	0.215	435	0.412	0.215

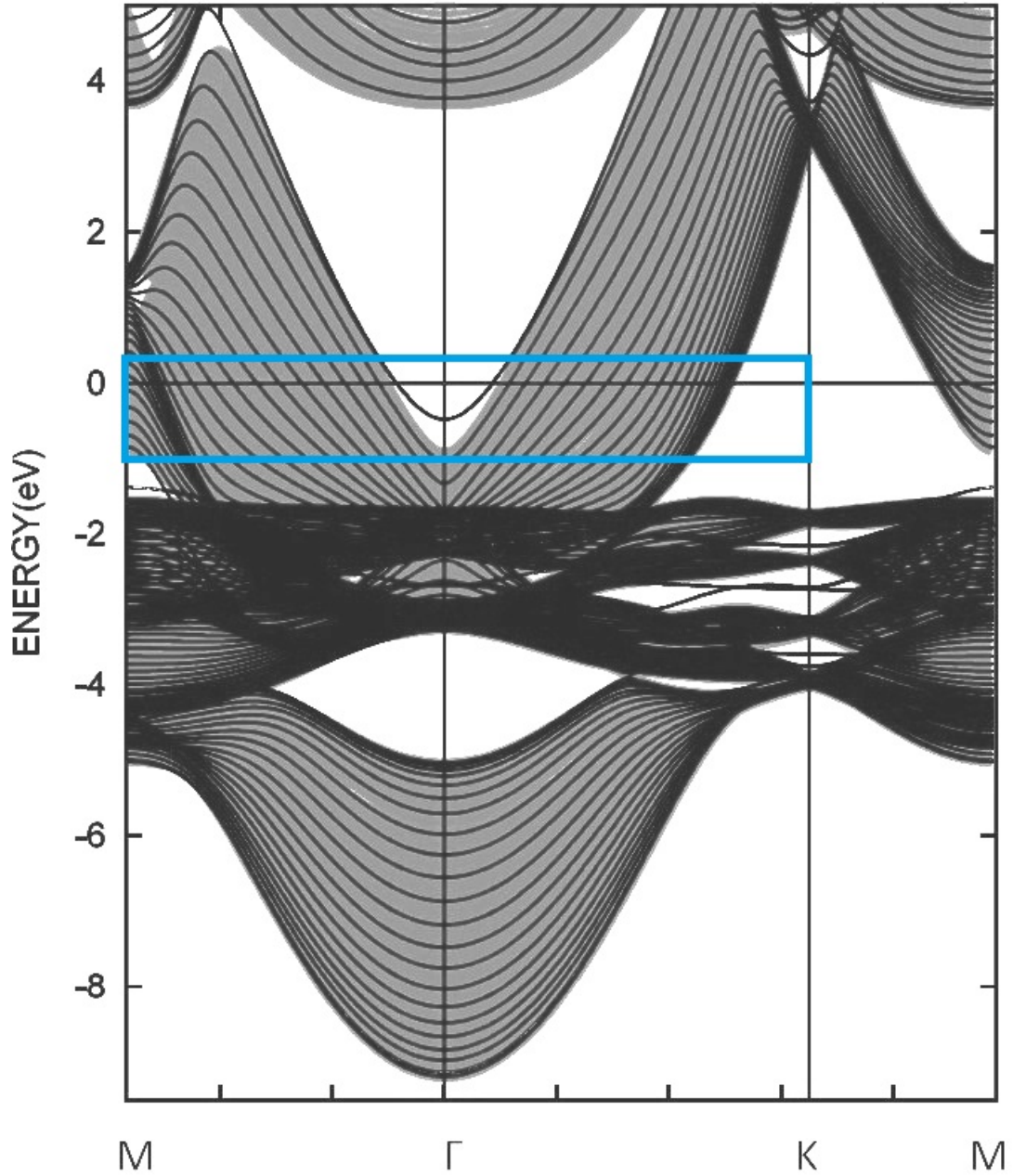


Figure 3.6: Energy bands of 24-layer slab of Cu(111). The projected bulk band structure corresponds to the shaded regions, along high symmetry directions of the surface Brillouin zone. The blue rectangular frame denotes the approximate range of the calculated projected bulk band structures, shown in Fig. 3.7.

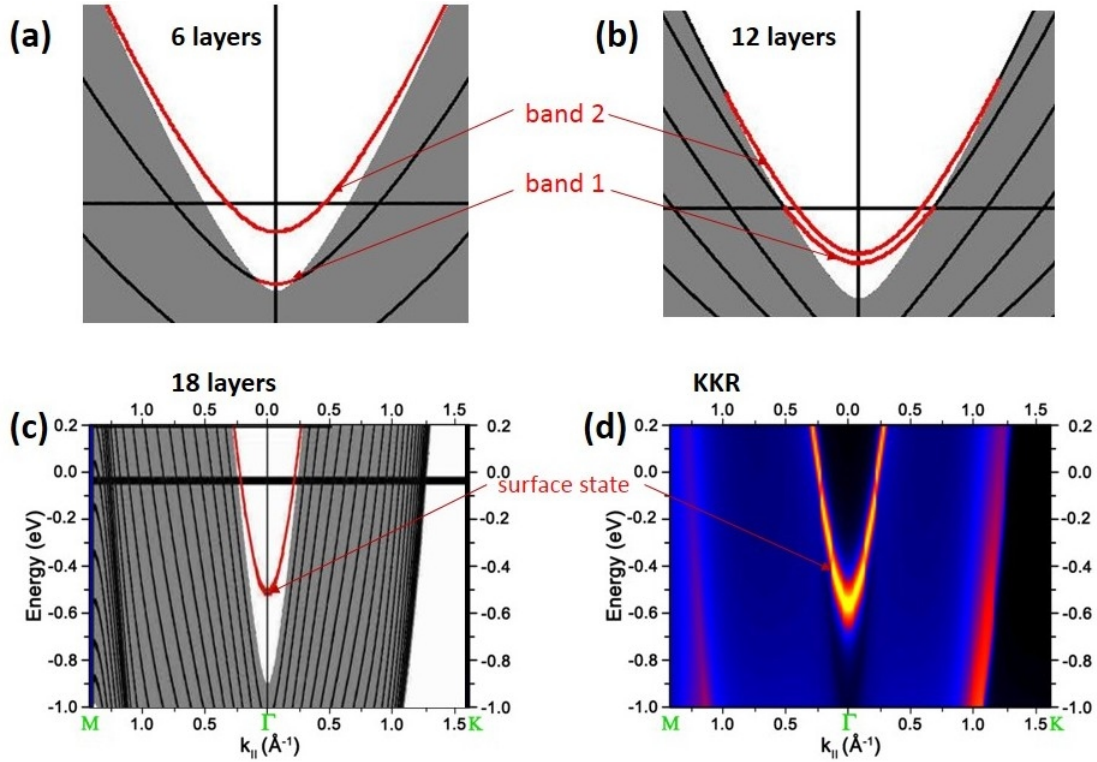


Figure 3.7: Two-dimensional band structure of the Cu(111) surface. The projected bulk band structure corresponds to the shaded regions, along high symmetry directions of the surface Brillouin zone: (a) Schematically showing the band 1 and band 2 separation for a 6-layer slab, calculated by VASP (b) the bands separation is decreased a 12-layer slab, calculated by VASP (c) the bands separation visually disappeared for a 18-layer slab, calculated by VASP (d) (Taken from Ref. H5) The energy resolved spectral density map calculated at the interface layer of the Cu(111) surface, calculated using KKR Green's function method. Blue and violet areas correspond to the projected bulk bands. Black regions are gaps of the projected band structure. The surface state band is presented as the bright parabola.

4 TM nanowires on Cu surfaces

This chapter provides a systematic discussion of one-dimensional magnetic nanostructures grown on a vicinal Cu(111) surface using the template which will be discussed in detail in the next sections (cf. Fig. 4.5 (b)). On the vicinal Cu(111) surface, an array of parallel Fe stripes was produced in the experiments of Shen *et al.*[5, 6]. Usually, nanowires or nanostripes grow on lower terraces along an ascending step edge. Surprisingly, in their observations this have been demonstrated that Fe nanostripes grow on the upper terrace of a stepped Cu(111) surface. For years, the kinetic mechanism leading to the formation of such structures has not been elucidated. An important step was made by Mo *et al.*[18], who used *ab initio* calculations within the density functional theory and showed that the growth of Fe nanowires is done in a two-stage process and subsequently, Guo *et al.*[7], have experimentally confirmed this growth process.

This study is focused on $3d$ transition metals from Sc to Ni, because they offer a wide range of complex magnetic structures in higher dimensions and contain the bulk ferromagnets. In contrast to the previous theoretical investigations we concentrate on the magnetic properties of mixed TM-Fe wires behind the step.

This chapter is organized as follows: In the next section, details of growth of $3d$ TM nanowires on Cu surface will be discussed. Then the performed *ab initio* calculations are presented. The presentation of the results and the discussion start with an explanation of the magnetic structures. Those structures are investigated for TM-Fe wires embedded in the Cu surface and for comparison for isolated free standing wires as well. A detailed compilation of the real structure data of the embedded TM-Fe wires follows. After the presentation of the ground state energies and magnetic moments a discussion follows. Special emphasis is placed on the properties of Cr-Fe and Mn-Fe wires.

4.1 Experimental and theoretical background

A stepped surface is a common template to create one-dimensional nanostructures.[80] The main idea is to exploit the 1D symmetry provided by an array of parallel steps on a vicinal surface. Along this surface the deposited material can nucleate, a procedure called step decoration. Chains or nanostripes usually grow on lower terraces along an ascending step edge. Cu surfaces can be prepared with lots of atom-high steps. Surprisingly, the observations of Shen *et al.*[5, 6] have demonstrated that Fe nanostripes (cf. Fig. 4.1(a,b)) grow on the upper terrace of a stepped Cu(111) surface.

An important investigation to elucidate the growth of linear Fe nanostructures on a stepped Cu(111) surface was made by Mo *et al.*[18] They elucidated a kinetic pathway for the formation of Fe nanowires on the upper edge of a monatomic-layer-high step on

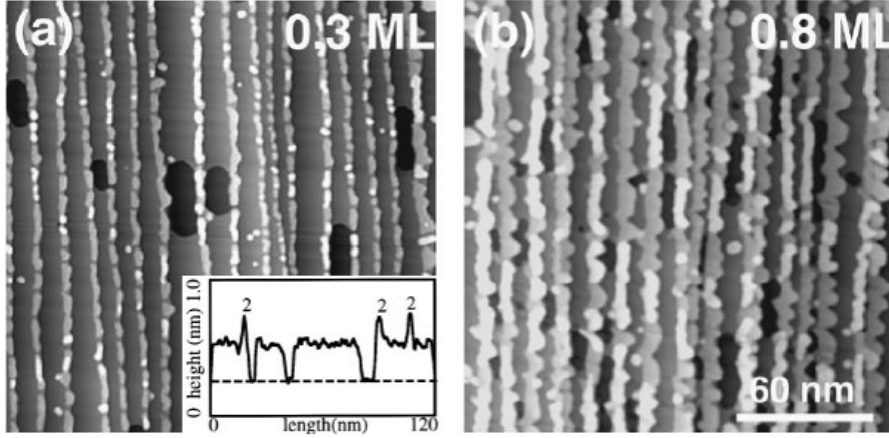


Figure 4.1: (Taken from Ref.[5]) STM topography image of 0.3-ML a and 0.8-ML b Fe stripes on Cu(111) stepped surface. The marked line profiles are shown in the upper-right corner with the dashed lines indicating the height level of the substrate.

Cu(111) using first-principles calculations. The identification of a hidden fundamental Fe basal line within the Cu steps prior to the formation of the apparent upper step edge Fe wire produces a totally different view of step-decorating wire structures.

The investigation of elementary diffusion and exchange processes of Fe atoms on a stepped Cu(111) surface by means of ab initio calculations based on density functional theory proved the existence of a special kinetic pathway of the formation of Fe nanowires on stepped Cu(111) surfaces. Kinetically the growth of linear Fe nanostructures is a two-stage process. At first, Fe adatoms form an atom chain embedded into the Cu substrate behind a row of Cu atoms at the descending step (cf. Fig. 4.2 and Fig. 4.5(a,b)). This formation of a linear 1D Fe structure makes the row of embedded Fe atoms very stable. In a following step the embedded Fe chain acts as an attractor for the Fe atoms deposited on the surface. Therefore, a secondary chain of Fe atoms is formed on top of the embedded Fe chain (cf. Fig. 4.3 and Fig. 4.5(c)), since Fe-Fe bonds are stronger than Fe-Cu bonds. As a result, a very stable atom-wide iron nanowire is formed on the Cu surface, one chain is buried in the surface behind a step, and the second chain on top of the first. Total energy calculations revealed that the position of the Fe chain at the upper edge is energetically favorable to a Fe chain located at the step edge, but only under the condition that another row of Fe atoms is incorporated underneath the exposed row.[18]

Here, a description for the formation of one-dimensional Fe nanowires of single atom width on stepped Cu(111) surfaces will be given. The interaction of a Fe adatom with the stepped surface will be discussed first. The preferred adsorption site of an Fe adatom appears to be the fcc site, whether it is located in the central region of a terrace or in the immediate vicinity of the step. In contrast, the activation energy barrier encountered by the adatom which moves on the surface is not necessarily the same in the two regions. An activation energy barrier of 0.025 eV is obtained for terrace diffusion. The preferred

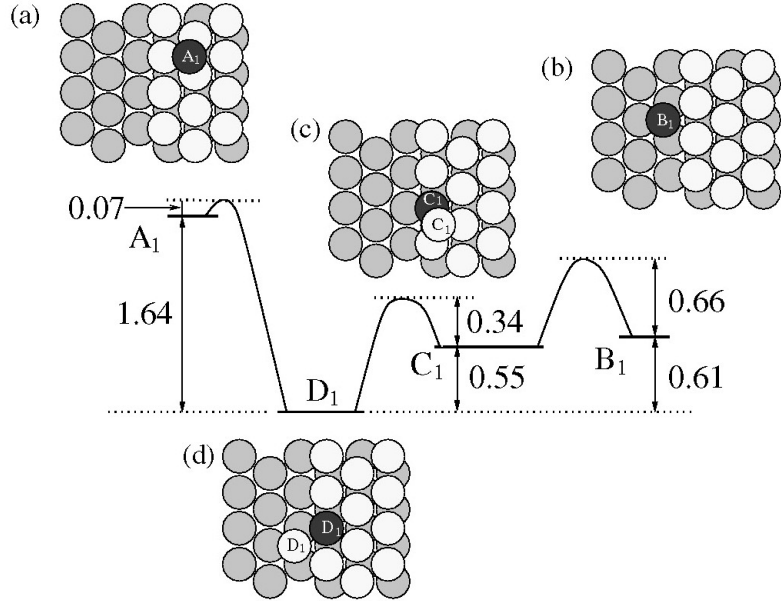


Figure 4.2: (Taken from Ref.[18]) Top view of the surface model employed in the calculations which presents the first phase of Fe wire formation. The white and gray circles represent Cu atoms in the first and second layers, respectively; the black circles represent Fe atoms. (a) Initial configuration of an Fe adatom reaching the step from the upper terrace. (b) Initial configuration of an Fe adatom reaching the step from the lower terrace. (c) Intermediate state of the Cu-Fe assisted exchange as the state B₁ converts to the final state D₁ in (d), which is also the stable final configuration from A₁ after place exchange. The relative energies and the activation barriers (in eV) connecting the different configurations are indicated next to vertical arrows.

mechanism is via direct hopping in this case. When an Fe adatom reaches a step from the upper edge (Fig. 4.2(a)), it should overcome a barrier of 1.00 eV, if it climbs down via direct hopping over the step edge (Fig. 4.2, A₁ → B₁). However, the Fe adatom can simply be embedded into the Cu layer through an exchange process (Fig. 4.2, A₁ → D₁) with an energy barrier of only 0.07 eV. Moreover, in this exchange process, the Cu atom displaced by the Fe adatom prefers to stay next to the embedded Fe atom. Because it has to avoid a high activation barrier of about 0.9 eV to reach the nearest hcp site away from the step edge.

Fe adatoms can also approach a step from the lower terrace. The Fe atom goes through an exchange process with a Cu atom at the step edge through an intermediate state C₁ in this case. The Fe atom is incorporated into the step first by displacing a Cu atom upward onto an hcp site at the upper step edge (Fig. 4.2(c)). This process has an activation barrier of 0.66 eV (Fig. 4.2, B₁ → C₁); subsequently, the displaced Cu atom jumps off the step directly to the lower terrace. The activation barrier of this process is 0.34 eV (Fig. 4.2, C₁ → D₁). Therefore, no matter in which direction the Fe adatom

approaches the step edge, there is just one stable final configuration, as shown in Fig. 4.2(d).

Now, we assume a second Fe adatom approaches the step which already has an embedded Fe atom from the upper edge. The second approaching Fe atom prefers to join the first one and form an embedded wire with two atoms in length to gain an energy as much as 2.52 eV. Additional Fe atoms which move toward the step edge will undergo the same processes. Finally, this leads to a row of Fe atoms which are embedded in the Cu step. This embedded Fe chain is one lateral lattice constant away from the step edge.

The deposition of additional Fe atoms on the stepped surface (containing an embedded Fe chain) is considered next. The most stable configurations are shown in Fig. 4.3. There are two possible ways for an Fe adatom to approach the mixed step. Either it approaches from the upper or lower terrace. From the upper terrace, the configuration A_2 is energetically stable because of the attraction of the Fe adatom to the basal Fe chain. In contrast, for an Fe adatom approaching from the lower terrace the configuration B_2 is energetically unstable. Similar to the processes shown in Fig. 4.2, the high energy configuration B_2 will convert into A_2 by two intermediate states C_2 and D_2 . There is an exchange process for the configuration C_2 to be reached. The Fe adatom takes the place of an edge Cu atom, and the Cu atom displaced up to reside on top of three Fe atoms. When the atop Cu atom climbs down the step, D_2 is the most stable configuration. The $D_2 \rightarrow A_2$ transition is finally reached via a second assisted process. The relative energies shown in Fig. 4.3 and the detailed calculations for the first phase (Fig. 4.2) suggest that the kinetic barriers encountered in the overall $B_2 \rightarrow A_2$ transition are all relatively small. Therefore, additional deposition of Fe atoms on the mixed stepped surface leads to the growth of an Fe chain on top of the embedded Fe basal chain. It is obvious that the width of this Fe chain is only one atom. Further growth of Fe atoms will just increase the width of the Fe chain. But the narrowest stable Fe chain is an atom-wide structure residing at the upper edge of the step.

Subsequently to Ref. [18], in a scanning tunnelling microscopy (STM) investigation aided by DFT calculations, Guo *et al.* [7] have confirmed the growth process. A careful study of all atomic processes in the line of Ref. [18] has been used to perform kinetic Monte Carlo calculations.[81] The simulations demonstrate the growth process as predicted by Mo *et al.* and proved experimentally.[7]

Furthermore, the Cu(111) stepped surface with the embedded Fe chain can be considered as an exemplary template for the deposition of other *3d* TM atoms to form a chain on top of the embedded Fe chain. It is the interplay between dimensionality, local environment and magnetic properties which causes the special interest in such systems. For a clear notation a single linear periodic arrangement of atoms will be called a chain in the following investigation, while a system consisting of two parallel chains, either isolated or embedded in the Cu(111) surface, will be named wire.

TM chains have been considered in previous density functional studies in different environments. Spišák and Hafner investigated metal chains at the step edge of vicinal Cu surfaces [14, 15, 16, 17]. Infinite metal chains on flat surfaces have been studied in Ref. [12] while Ataca *et al.* [11] and Tung and Guo [10] focused on isolated chains. Finite chains on flat Cu and Ni surfaces have been considered in Ref. [9, 8]. Antiferromagnetic

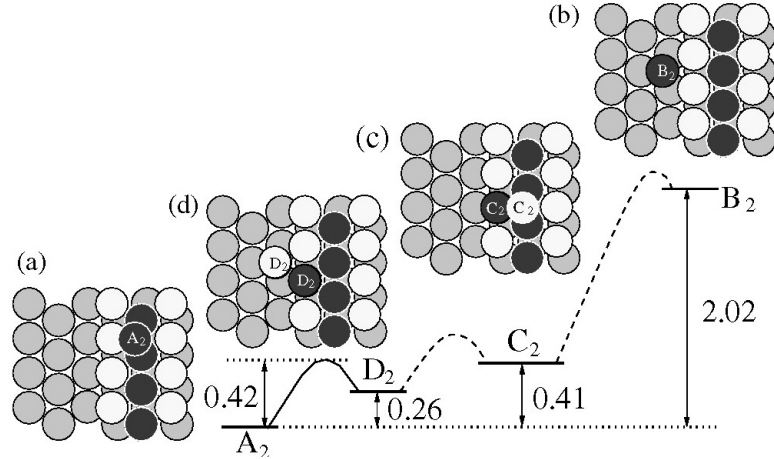


Figure 4.3: (Taken from Ref.[18]) Top view of the second phase of the two-phase kinetic pathway for Fe wire formation on the stepped Cu(111) surface, together with the energy levels and activation barriers (in eV) for different configurations. Dashed lines indicate energies not explicitly calculated. (a) and (b) show the initial configurations reached when an Fe adatom approaches the Fe-Cu mixed step from the upper and lower terrace, respectively. Configuration A_2 is energetically most stable, because of the strong attraction by the buried Fe wire. Configuration B_2 is energetically very unstable, and will convert to configuration A_2 via two intermediate configurations shown in (c) and (d).

order has been found experimentally by Hirjibehedin *et al.* [4] for linear finite Mn chains created by atom manipulation on an insulating CuN/Cu(001) surface.

4.2 Theoretical method

4.2.1 Setup

Computational details and convergence checks are the same as those in the previous chapter. Structural relaxations have been performed using the quasi-Newton algorithm, and stopped when the forces acting on all the unconstrained ions have dropped below 0.01 eV/\AA . During structural relaxations the bottom three layers of the six-layer slab are fixed at their ideal bulk positions (calculations using an eight-layer slab lead to insignificant changes in energy differences between the magnetic configurations). The convergence of the calculated properties with respect to the number of k-points and supercell size was carefully checked.

Isolated chains

The isolated chains and wires have been modeled as a two-dimensional array of infinitely long units, keeping the distance to be at least 13\AA . 12 k-points are used to sample half

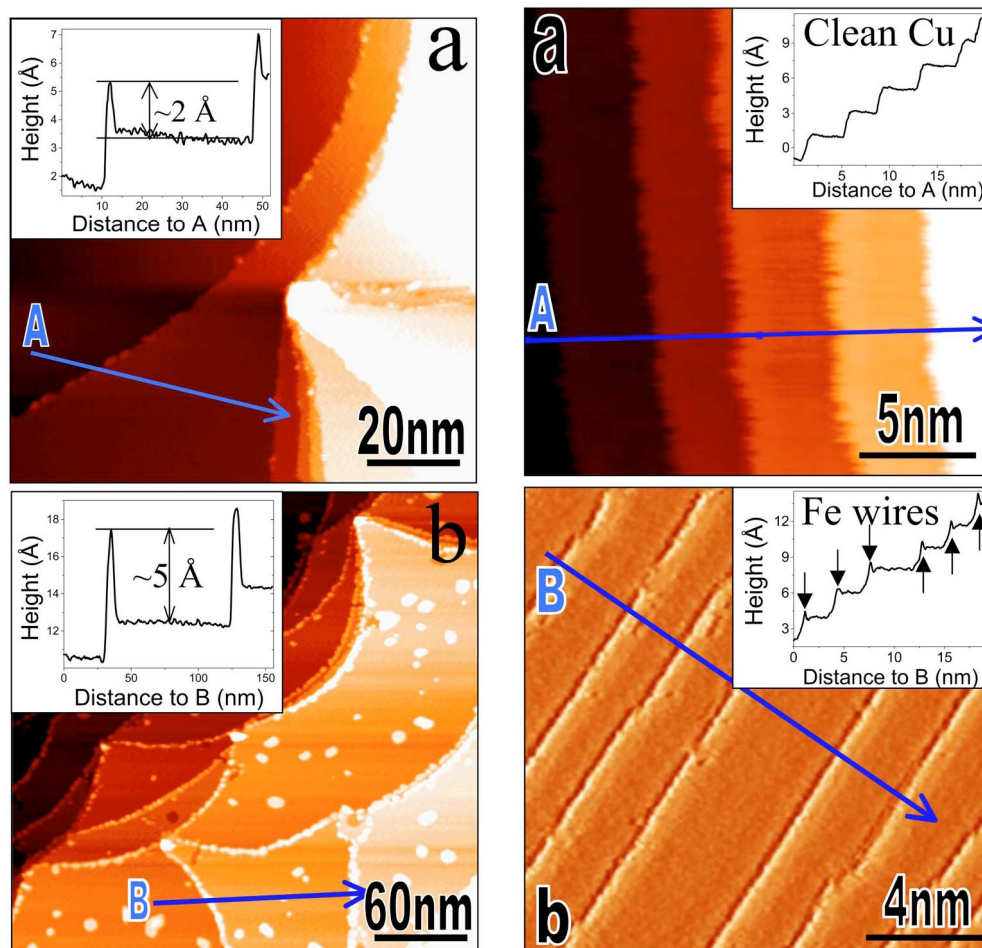


Figure 4.4: (Taken from Ref.[7]) Left: STM images of Fe on Cu(111) with different nominal coverages: (a) 0.03 and (b) 0.10 ML. The inset shows the line profiles of the nanowires across the step edges as indicated in the topographic images. Right: STM images (+30 mV/10 nA) of (a) clean vicinal Cu(111) surface at RT and (b) a Fe nanowire array on the vicinal Cu(111) surface at 60 K.

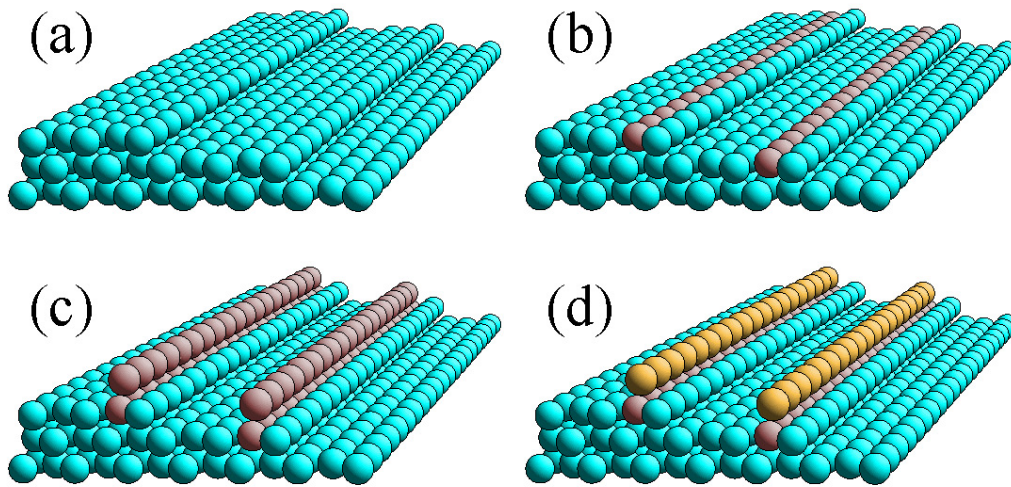


Figure 4.5: (Taken from Ref. H7) Growth of TM-Fe double chains on Cu(111): (a) clean Cu(111) stepped surface (b) deposition of Fe atoms (brown) on a stepped Cu (blue) surface. The Fe chain is embedded in the step behind a row of Cu atoms. (c) one-atom-wide Fe nanowire (brown) is formed, one chain of Fe embedded in the surface behind the step, the second Fe chain is formed on top of the first. (d) one-atom-wide TM nanowire (yellow) is formed on top of the embedded Fe chain.

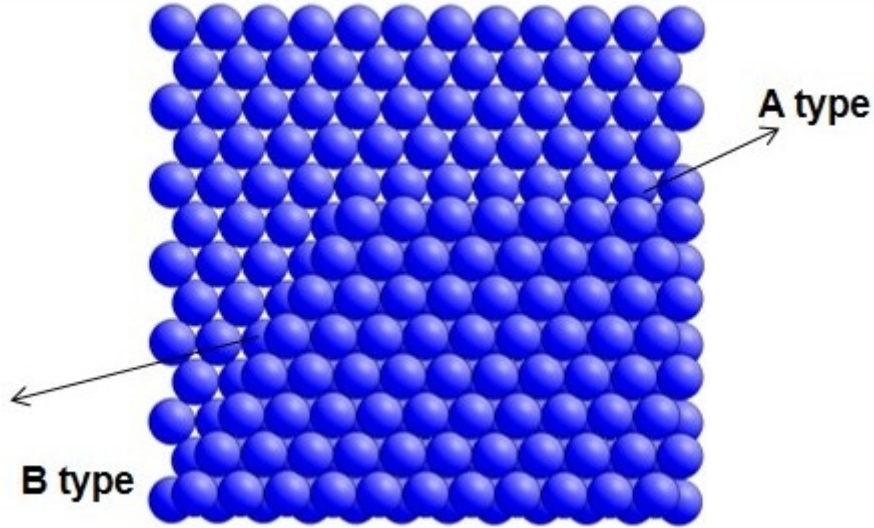


Figure 4.6: On the (111) surface of an f.c.c. packed lattice two non-equivalent types of step edges are possible, forming either $\{100\}$ facets (type A) or $\{111\}$ facets (type B).

of the one-dimensional Brillouin zone.

Construction of the surface

There are two types of steps on Cu(111), called A and B types, with the former having lower formation energy [82]. Experimentally, Fe wires have been observed to form on the upper edges of both types of steps [18]. Hence, in the present study we focus our attention on growth of Fe wires on A-type steps. We model the stepped Cu surface by a slab miscut along the (322) direction, following Ref. [83], consisting of (111) terraces of width five lateral lattice constants separated by type A steps of monatomic height.

A supercell containing six Cu layers, which corresponds to 60 Cu atoms, was constructed to model the Cu(111) stepped surface. The Cu slab was rotated in turn by a slab miscut along the (322) direction. Therefore, at the end, the system consists of (111) terraces separated by $\{100\}$ faceted steps of monatomic height. The same construction was used by Mo *et al.* [18]. The terraces are five lattice constants wide. The distance from one slab to its nearest image was equivalent to 13.5 Å. In all calculations the two-dimensional Brillouin zone was sampled using a 20×5 mesh. The template constructed in this way is shown in Fig. 4.5 and Fig. 4.8.

4.3 Isolated TM chains

As mentioned earlier, the transition metal isolated chains are constructed with the ideal Cu bond length of $d_{Cu}=2.569\text{Å}$. The calculated total energy relative to that of the NM state (i.e., the magnetization energy) of the FM and AF linear atomic chains and the

spin magnetic moments are listed in Tab. (4.1). The calculations reveal that the *3d* TM elements which are nonmagnetic in their bulk structures (Sc, Ti, V and Mn), become magnetic in the linear chain structures. Furthermore, for these *3d* TM elements, the NM state is metastable and the ground state is either FM and AF. The ground states for the Sc, Ti, V, Fe, Co and Ni chains are ferromagnetic while that for the Cr and Mn chains are antiferromagnetic.

Table 4.1: Calculated total energies (E_t) (in eV/atom) in the FM and AF states (relative to the NM state), and spin magnetic moments (m_s) (in μ_B /atom), of the *3d* transition metal linear chains. No AF solutions were found for Sc, Ti and Ni.

	E_t^{FM}	m_s^{FM}	E_t^{AF}	m_s^{AF}
Sc	-0.053	0.13	—	—
Ti	-0.331	1.99	—	—
V	-0.968	3.01	-0.810	2.62
Cr	-1.979	3.98	-2.447	3.99
Mn	-1.990	3.45	-2.508	3.99
Fe	-1.698	3.13	-1.536	3.17
Co	-0.758	2.03	-0.537	2.09
Ni	-0.190	0.96	—	—

The Cu bond length is longer than the calculated bond lengths of these *3d* TM elements in the bulk structures. For example, the calculated bond lengths for AF bcc Cr, FM bcc Fe and FM fcc Co are 2.43, 2.45 and 2.48 Å, respectively. The chemical bonding environment in a chain is not the same as that in a bulk structure. In particular, the coordination number in a linear wire is certainly lower than in a bulk structure. Further discussions concerning the bond length and spin magnetic moments can be found in Sec. 4.5.

4.4 Free-Standing TM-Fe wires

Now, the magnetic properties of free-standing double chains including Fe and TM chains with an interatomic distance corresponding to the Cu bond length have been investigated first. If a nanowire consisting of a TM and a Fe chain (TM-Fe wire) is constructed, a series of different magnetic structures is possible. We will restrict our investigation to four atoms per unit cell. In this case five different magnetic structures can be formed. All the structures are depicted schematically in Fig. 4.7. The notation of the magnetic structures throughout the thesis is such that the first letter (A - antiferromagnetic, F - ferromagnetic) characterizes the TM chain, while the second letter characterizes the embedded Fe chain. To distinguish the two possible directions of moments if both chains are ferromagnetically ordered an antiferromagnetic coupling between the chains is marked

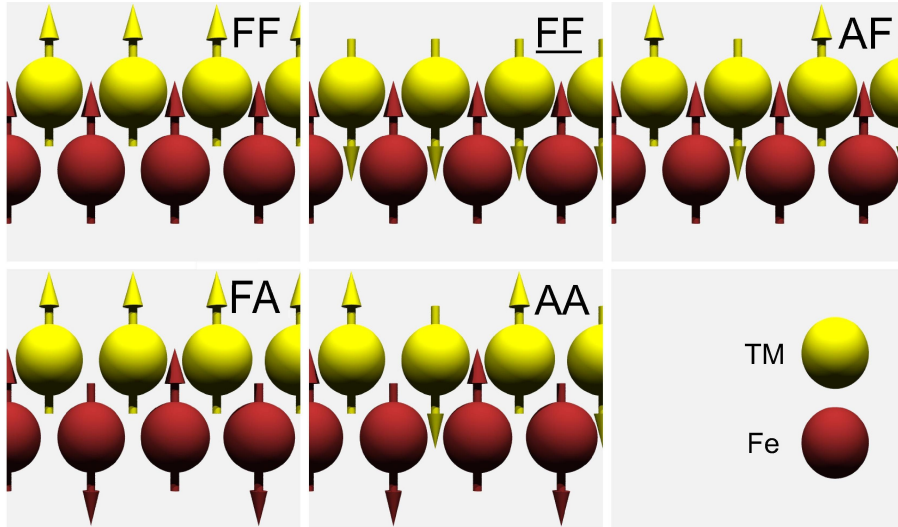


Figure 4.7: (Taken from Ref. H7) Schematic view of the five magnetic configurations considered for nanowires consisting of TM (yellow) and Fe (red) chain. FF: ferromagnetic structure, FF: ferromagnetic chains are coupled antiferromagnetically, AF: the antiferromagnetic TM chain is coupled to the ferromagnetic Fe chain, FA: the ferromagnetic TM chain couples to the antiferromagnetic Fe chain, AA: antiferromagnetic arrangement.

by an underscore FF. Three structures result from a ferromagnetically ordered Fe chain (FF,FF,AF). In principal, also the Fe chain could order antiferromagnetically. Two additional magnetic structures can be formed. Either the TM chain exhibits ferromagnetic (FA) or antiferromagnetic order (AA). The calculations reveal that configurations with the antiferromagnetic order (FA, AA) of Fe chain are energetically not favorable. Such structures are not taken into account in the following discussion.

The total energy calculations, summarized in Tab. 4.2, reveal magnetic solutions for all the TM wires. Not all magnetic configurations could be stabilized in the self-consistent electronic structure calculations.

Table 4.2: Energy differences (meV/cell) for the different magnetic configurations with respect to the ferromagnetic state for the free-standing double chains, consisting of a $3d$ transition metal chain and a Fe chain.

Configuration	Sc	Ti	V	Cr	Mn	Fe	Co	Ni
E_{FF}	-1153	-694	-710	-371	743	1225	1026	993
E_{AF}	—	—	-371	-600	161	837	716	—

Tab. 4.3 contains the magnetic moments of the free-standing TM-Fe chains. The Fe chain moment increases slightly from Sc to Ni and is enhanced with respect to the bulk

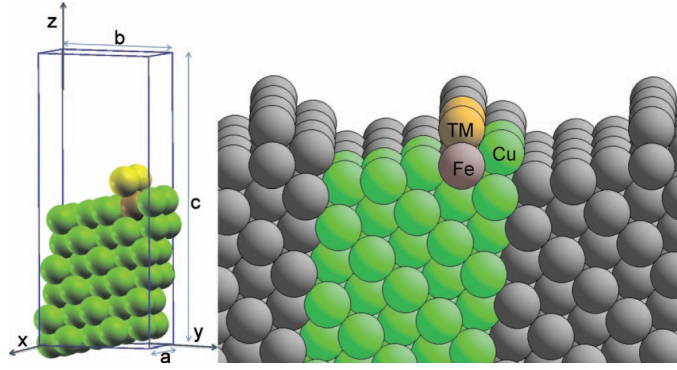


Figure 4.8: (Taken from Ref. H6) TM-Fe wires on vicinal Cu(111) surface. A one-atom wide TM chain (yellow) is formed on top of an embedded Fe chain (red). Dimensions of the supercell: $a = 5.14 \text{ \AA}$, $b = 10.59 \text{ \AA}$, and $c = 25.69 \text{ \AA}$. (Colored atoms in the structure on the right hand side represent the unit cell.)

value due to the reduced number of neighbors. The variation of the moments in the TM chain follows the usual trend known from the free atoms and other $3d$ TM nanostructures (cf. [84]) Mn shows a high local moment as it was also obtained for Mn clusters on the Ag(100) surface [85].

Table 4.3: Absolute values of magnetic moments in ground state configurations of free-standing TM-Fe double chains, given in (μ_B).

TM elements	Sc	Ti	V	Cr	Mn	Fe	Co	Ni
$ \mathbf{M}_{TM} $	0.70	1.56	2.61	3.53	4.07	3.05	2.04	0.88
$ \mathbf{M}_{Fe} $	2.69	2.77	2.85	2.97	2.90	3.05	3.14	3.17

4.5 TM-Fe wires on Cu(111)

4.5.1 Structural and magnetic properties

Information about structural relaxations are given in Table 4.4 and Table 4.5. Relaxations of the first three layers at the surface are considered. All relaxations are given for the magnetic ground state configuration. The relaxations are given in percentages of the ideal values, i.e. in-plane relaxations (Δy) are expressed in terms of the ideal Cu bond length $d_{Cu} = 2.569 \text{ \AA}$ whereas the interlayer relaxations are calculated with respect to ideal interlayer distance of $d_{12} = 2.098 \text{ \AA}$.

The relaxations of the clean Cu(111) surface are compared with relaxations in presence of an embedded Fe chain (cf. Fig. 4.10). The nomenclature used in the table is explained

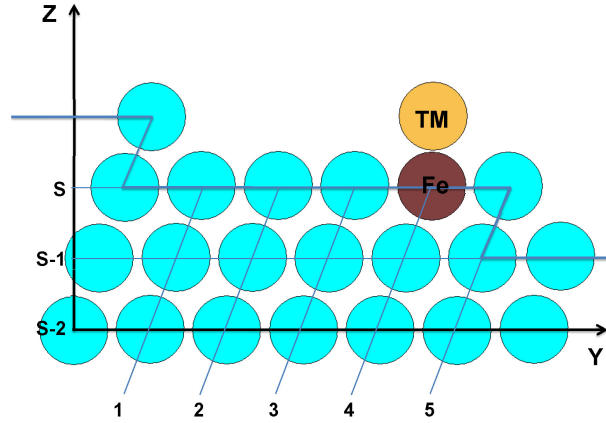


Figure 4.9: (Taken from Ref. H7) Schematic view of the stepped surface. The nomenclature of the figure is used in Table 4.4 and Table 4.5. Δy is positive if the shift is directed in-plane to the step edge. Δz is positive for an outward relaxation perpendicular to the surface.

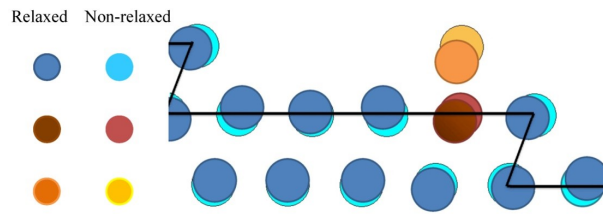


Figure 4.10: Schematic view of the Cu(111) stepped surface that exhibits the relaxation of the first and second topmost layers. The light colors depict the unrelaxed structure while the dark ones delineate the relaxed geometry.

in the schematic view given in Fig. 4.10. The relaxations in the second subsurface layer (S-2) are small in general. The relaxations in (S-1) are larger but only significant at the step edge. The relaxations of the surface layer of Cu(111) are dominated by two effects. The lateral relaxation are pointed to the center of the terrace causing a compression. The lateral relaxation Δy at site (3) in the middle of the terrace is small. In general the surface layer shows an inward relaxation. At the step edge, site (5), the inward relaxation is large. Together with the outward relaxation at site (1) the relaxations reduce the interatomic distances at the step edge.

The relaxations change significantly if one row of Cu atoms is substituted by one row of Fe behind the step edge. Larger relaxation effects can be obtained. From the structural point of view the Fe chain acts as a "center of attraction". On clean Cu(111) site (3) in (S) shows practically no lateral shift Δy whereas the Cu atom at site (3) is shifted towards the embedded Fe chain. Also the Cu atoms in the step at site (5)

Table 4.4: Lateral and vertical relaxations of the clean Cu(111) vicinal surface, the Cu(111) surface with the embedded Fe chain and the Cu(111) surface with the embedded Fe-Fe wire. Relaxations are given with respect to the ideal lattice positions. Lateral relaxations are expressed as percentage of the ideal bond length 2.569Å. Vertical relaxations along the (111) direction are given as percentages of the interlayer distance 2.098Å. The relaxations are presented for the surface (s) and two subsurface layers and all rows of atoms (1)-(5) parallel to the step in the terrace.

vicinal Cu(111)										
	(1)		(2)		(3)		(4)		(5)	
	Δy	Δz								
(s)	2.4	2.7	1.2	-0.9	0.2	-1.1	-1.2	-0.5	-3.8	-4.4
(s-1)	0.2	0.5	-0.4	0.6	0.0	-0.3	0.3	-0.4	1.7	-1.0
(s-2)	-0.1	0.2	-0.1	0.4	-0.3	0.3	-0.3	0.0	0.0	0.3
Fe chain embedded in Cu(111)										
	(1)		(2)		(3)		(4)		(5)	
	Δy	Δz								
(s)	1.4	3.1	-0.3	0.2	-1.4	0.3	-2.8 (Fe)	-0.9 (Fe)	-5.2	-2.6
(s-1)	0.2	0.6	0.1	1.1	0.2	0.2	0.4	-0.8	1.2	-0.7
(s-2)	0.2	0.1	0.2	0.6	-0.1	0.5	-0.2	-0.3	0.2	-0.1
Fe-Fe wire embedded in Cu(111)										
	(1)		(2)		(3)		(4)		(5)	
	Δy	Δz								
(s)	1.1	5.2	-0.2	1.8	-1.0	5.3	-2.7 (Fe)	-5.9 (Fe)	-6.4	-0.7
(s-1)	1.2	1.2	0.5	2.5	1.1	3.1	-0.4	-4.1	1.5	-1.2
(s-2)	0.6	0.2	0.8	1.2	0.3	2.0	-0.6	-1.5	0.9	-0.9

are strongly attracted by the Fe chain. The inward relaxation of the Fe chain is much larger than the corresponding relaxation of a Cu atom at this site. In summary, the Fe chain increases dramatically the tendency to a compression near the step. Therefore also changes in the magnetic properties of TM-Fe wires can be expected if compared to calculations based on an ideal real structure.[H8]

The relaxations after forming a TM-Fe wire (cf. Fig. 4.5(d)) are summarized in Table 4.5. The relaxations at sites (1-3,5) in the surface do not change significantly compared to the situation of an embedded Fe chain alone, therefore Table 4.5 contains relaxations of the TM and Fe chains only. The magnetic ground state of the corresponding system is also indicated in the table. Three magnetic ground states are obtained (cf. Fig. 4.7).The antiferromagnetic (AF) structure of Cr leads to special effects in the real structure. Therefore Cr will be discussed separately. The TM chains within the FF and FF magnetic structures show an inward relaxation towards the Fe chain and a

Table 4.5: Relative relaxations of the TM-Fe wires deposited on the surface. The ground state magnetic structure (MS) is also indicated.

TM	MS	TM		Fe	
		Δy	Δz	Δy	Δz
Sc	<u>FF</u>	-4.7	-19.8	-0.8	-2.1
Ti	<u>FF</u>	-5.0	-28.5	0.6	-0.2
V	<u>FF</u>	-6.3	-33.2	1.8	0.1
Cr	AF	-3.8(-0.5)	-24.2(-4.4)	-4.0	-6.2
Mn	FF	-3.0	-15.8	-4.2	-6.4
Fe	FF	-3.1	-22.5	-2.7	-5.9
Co	FF	-4.8	-25.8	-2.3	-6.1
Ni	FF	-4.6	-23.9	-5.0	-8.7

shift away from the step. Δy and Δz have the same order of magnitude for all those systems. The antiferromagnetic coupling of the ferromagnetic TM chain (Sc-V) reduces the inward relaxation of the Fe chain significantly. The TM-Fe wires formed by late TM (Mn-Ni) couple ferromagnetically (FF). The relaxation of the embedded Fe chain is nearly unchanged as it can be deduced by comparison with Table 4.5.

The detailed investigation of real structure effects of FF and FF structures proofs the strong correlation between magnetic and real structure in this quasi one-dimensional systems. Therefore especially the Cr-Fe wire, having an AF magnetic ground state structure, should show an interesting relaxation pattern. It should be noted, that magnetic frustration will lead in general to a non-collinear magnetic structure for this wire, which will reduce the relaxations compared to the strictly collinear calculations of the present paper. As schematic shown in Fig. 4.11, the Cr-Fe wire minimizes the energy by adopting a zigzag like structure in the plane perpendicular to the surface. The inward relaxations are 7.0% and 23.2% for Cr(\uparrow, \downarrow). Also the lateral relaxations show a zigzag structure of 14.3% and -35.5% for Cr(\uparrow, \downarrow) away from the step. The relaxations of the Cr atoms are connected with an inward relaxation of -2.9% of the embedded Fe chain and 7% of dimerization. The dimerization which is observed only for AF structures may be interpreted as a result of repulsive (attractive) nature of the magnetic contribution to the interaction energy of Cr (Fe) pairs in Cu.[86]

Stability of the different magnetic structures is the most interesting question in our investigation. The data are summarized in Fig. 4.12. The energy differences ΔE (in meV/supercell) are defined relative to the FF structure. Energy differences larger than zero indicate a stable FF structure, while $\Delta E < 0$ denotes the stability of FF or AF structures. The magnetic structures of the embedded wires are calculated in fully relaxed geometries.

The bulk ferromagnets Fe, Co, and Ni lead to a ferromagnetic TM-Fe wire in this low-dimensional configuration. If we assume an ideal structure for Mn (non-relaxed)

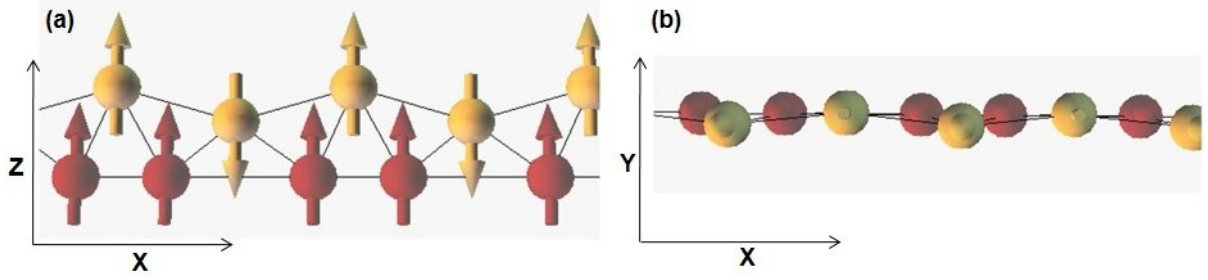


Figure 4.11: Schematic view of antiferromagnetic order of Cr chain making a zigzag deformation due to magnetic frustration on Cr-Fe: (a) side view of zigzag deformation of Cr chain (yellow) and dimerization Fe chain (brown) (b) top view of slightly zigzag deformed Cr chain in xy plane

a bistability between the FF and AF magnetic structures ($\Delta E \approx 13$ meV/supercell) is observed.[87] This bistability is lifted including relaxations and the energy difference becomes considerably larger, stabilizing the FF structure. ($\Delta E \approx 89$ meV/supercell, cf. Fig. 4.12). It was not possible to stabilize AF structures in our calculations for Sc, Ti and Ni. The Cr-Fe wire shows an antiferromagnetic (AF) structure.

Energy differences for the isolated TM-Fe wires are given in Fig.4.12 for comparison. The isolated wire is calculated in an ideal linear structure corresponding to the Cu bond length d_{Cu} . The embedding of the wires has a large effect on the FF magnetic structure of all the $3d$ TM but ΔE changes only marginal for most of the calculated AF structures. The comparison of magnetic structures of unrelaxed isolated wires with the embedded wires shows that the magnetic structures practically do not change. The most interesting system of the $3d$ series investigated here is the Cr-Fe wire. It is characterized by large local Cr(\uparrow, \downarrow) moments of 3.4 and $3.3 \mu_B$. Both, the FF and AF structures are practically not influenced by the embedding in the Cu surface. The AF structure is the ground state. It was pointed out by Mo *et al.* [7] that the adatom position on the embedded Fe chain represents a local energy minimum, independent on the type of the atom. From this point of view the formation of structurally well ordered antiferromagnetic Cr chains on top of the Fe template chain should be experimentally feasible.

The magnetic properties of the groundstate configurations will be discussed in more detail. The magnetic properties of isolated TM chains and TM-Fe wires will be used as a reference in the discussion. The ideal bond length d_{Cu} in accordance with the Cu bulk lattice constant is assumed for the calculation of those idealized structures. Although isolated TM chains show effects like dimerization and formation of a zigzag structure,(cf. [10, 11]) we do not allow such effects to have well defined reference structures.

The total energies of possible magnetic structures have been calculated to find the ground state. The calculations reveal that the ground states of the TM chains, TM-Fe wires, and the embedded structures are the same for most of the systems. Exceptions appear for Sc, V, and Mn. While the free Sc chain is nonmagnetic, the Sc-Fe wire exhibits the FF structure in the isolated and embedded case. The isolated V chain shows

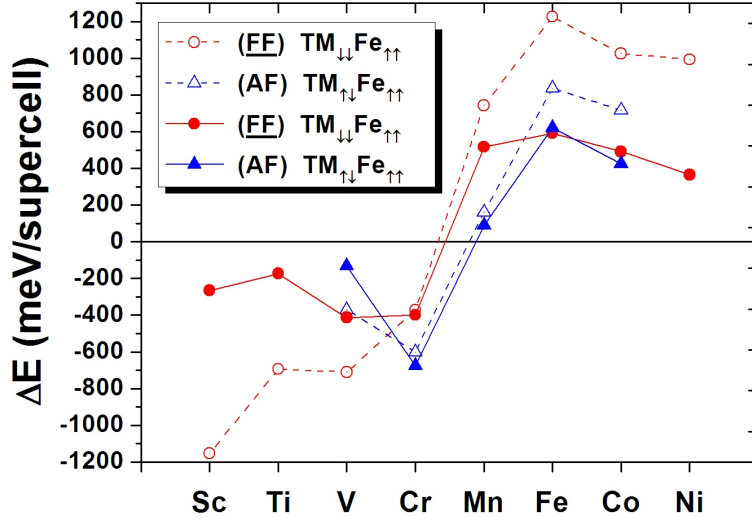


Figure 4.12: (Taken from Ref. H7) Total energy of the FF and AF states relative to the FF magnetic structure. The solid symbols are related to the embedded wires and the open symbols stand for the isolated TM-Fe wire. The energy calculations for the embedded structures are based on the relaxed structures.

ferromagnetic coupling while the isolated V-Fe wire and the corresponding embedded system exhibit an FF structure. The isolated Cr and Mn chains are antiferromagnetically coupled. The coupling to Fe in the isolated Mn-Fe wire accounts for the FF structure being the groundstate of embedded Mn-Fe as well.

Our calculations can be compared with results for fully relaxed linear chains by Tung and Guo [10]. The equilibrium bond lengths in the relaxed chains are up to 20% smaller than the Cu bond length assumed in our calculations. Only Sc shows a 10% larger bond length. The equilibrium magnetic structures in the relaxed geometry given in Ref. [10] are nevertheless the same as in our artificial structure strained to the Cu bond length, with V as an exception. It is not surprising that the V chain is ferromagnetic at the Cu bond length, because its relaxed interatomic distance is only 1.2% different from d_{Cu} in the ferromagnetic state, in contrast to a 20.2% smaller one with respect to the Cu bond length in the antiferromagnetic state. Fixing the bond length to d_{Cu} leads to the suppression of the Sc magnetic moment.

Starting from a linear chain and fixing the distance of next nearest neighbors to $2d_{\text{Cu}}$, a relaxation of the AF Cr chain leads to a zigzag deformation with an angle of 153° . This angle is 160° if the chain is deposited on top of the embedded Fe chain.

The magnetic moments of the ground states of all systems are given in Fig. 4.13. In general, the magnetic moments of the TM atoms in the TM-Fe wire are smaller than in the isolated TM chain. However, Sc is polarized and obtains a sizable moment, the Cr moment decreases and the Mn moment is practically unchanged. The Fe moment in the different wire systems is nearly constant and larger than the bulk value. Note that

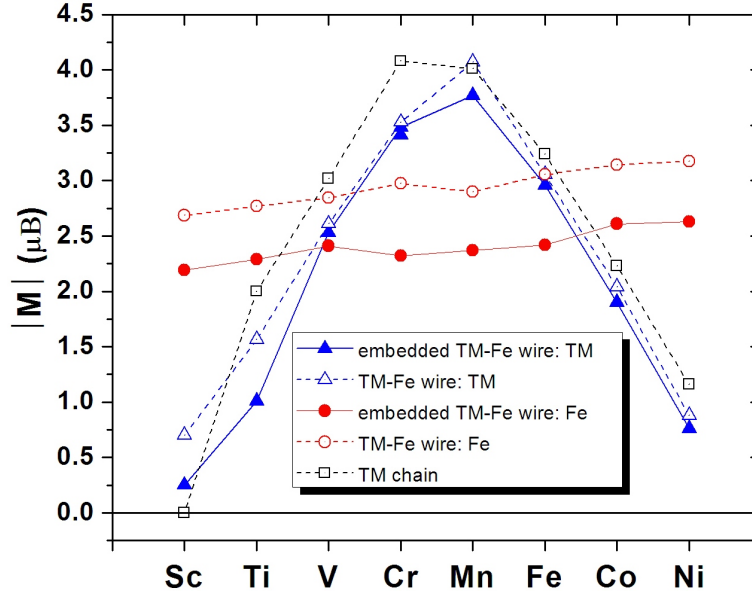


Figure 4.13: (Taken from Ref. H7) Absolute magnetic moments of the ground-state configurations. a) isolated TM chain and isolated TM-Fe wire. An ideal structure based on the Cu lattice constant is assumed. b) TM-Fe wire embedded in Cu(111) surface. The structure is relaxed.

our calculated magnetic moments for bulk ferromagnetic metals Fe, Co, and Ni are 2.23, 1.65 and $0.67 \mu_B/atom$, respectively. The combination of a TM chain with the Fe chain is connected with an increase of the coordination number of the atoms. This leads in general to a decrease of the moments. Due to the embedding each TM atom will beside the two Fe neighbors, get two additional Cu atoms as nearest neighbors. The moment of the template Fe chain is reduced by about $0.5 \mu_B$. The TM moments are only slightly reduced.

Our investigation reveals that from the $3d$ series Cr-Fe and Mn-Fe wires are the most promising systems for experimental investigations. In all configurations considered here Cr shows an antiferromagnetic coupling. Embedding has practically no effect on the stability of the AF structure. The latter is very stable with respect to the other magnetic structures. The bistability detected for the Mn-Fe system in the nonrelaxed structure was the starting point to investigate if changes in the lattice constant could force the Mn-Fe wire to switch to the AF structure. Compressive or tensile strain perpendicular to the wire does not change the magnetic structure. 5% compressive strain along the Mn-Fe wire leads to an AF ground state (see Fig. 4.14). Let's assume that the physics of the formation of the template Fe chain will not change if an appropriate substrate, i.e. a few Cu layers with a stepped (111) surface deposited on an adequate substrate which causes the strain in the Cu film, leads to a stress of some percent in direction of the Mn-Fe wire. In this case one could speculate that a switching of the magnetic state by external means might be possible.

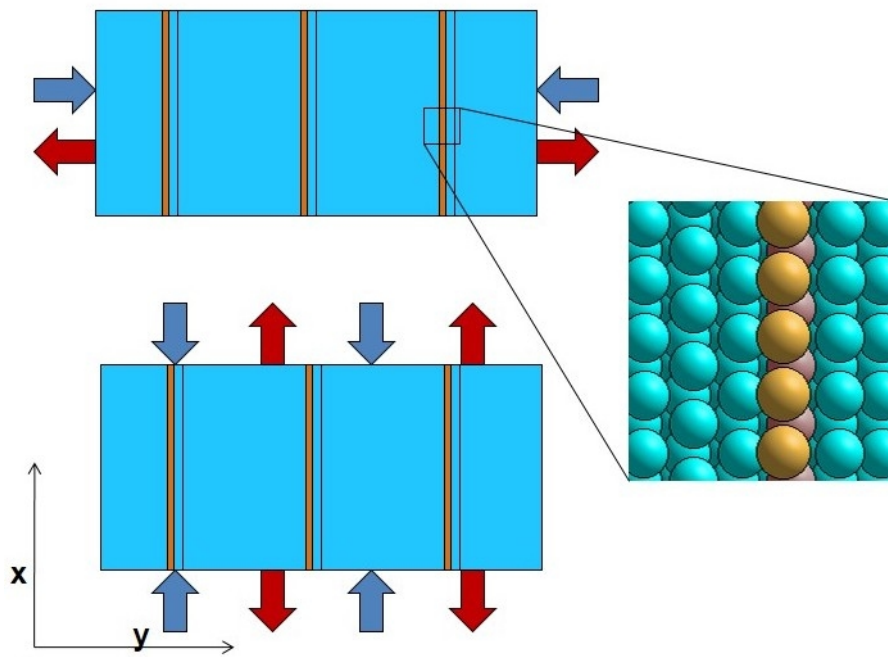


Figure 4.14: Picture on the top: Compressive or tensile strain perpendicular to the Mn-Fe wire does not change the magnetic structure . Picture on the bottom: 5% compressive strain along the Mn-Fe wire leads to an AF ground state.

In summary, we have performed first-principle calculations of magnetic states in TM-Fe wires on the vicinal Cu surface. The Fe chain near the step of the Cu(111) surface is the template for the formation of TM chains in atop position of the Fe chain.

Ferromagnetic (Mn,Fe,Co,Ni) as well as antiferromagnetic structures (Cr) might be achieved using the embedded Fe wire near the step as a template. The antiferromagnetic structure of Cr is very robust. Therefore the formation of long antiferromagnetic Cr chains on top of the Fe template chain should be experimentally feasible. Stress could be used to prepare Mn-Fe wires in ferromagnetic or antiferromagnetic structure. The systematic investigation of different magnetic states, as presented in this letter can be used as a starting point to consider the finite temperature magnetic properties of such TM-Fe wires. If the energy differences of the different magnetic states are mapped on a classical Heisenberg model the nearest neighbor exchange parameters J_{TM-TM} , J_{Fe-Fe} , J_{TM-Fe} can be determined. These values can be extracted from DFT calculations either by the comparison of total energies of several artificial collinear magnetic structures. In the next chapter, the second approach has been used. Then Monte Carlo calculations will be used to determine the magnetic properties at finite temperature.

5 First-Principles Calculation of Exchange Interactions

5.1 Introduction

Magnetic nanostructures on surfaces are of great interest for modern nanoscience due to their potential application as atomic-scale magnetic devices. Therefore, nanoscale clusters, monoatomic wires or quasi-1D stripes have been investigated from experimental [5, 6, 7] and theoretical point of view.[10, 18] The lower coordination of the magnetic atoms in such systems located on a metallic surface compared to bulk leads to an enhancement of the moments and a large magnetocrystalline anisotropy can help to stabilize the direction of the magnetic moments.

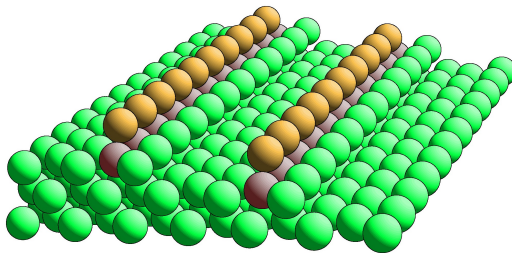


Figure 5.1: TM-Fe wires on vicinal Cu(111) surface. A one-atom wide TM chain (yellow) is formed on top of an embedded Fe chain (red).

The magnetic properties of the wires will be discussed in this chapter, by presenting a systematic investigation of the spin couplings in magnetic TM-Fe wires by analyzing the exchange interactions (interwire and intrawire couplings). Detailed information on the real structure of such systems is given in the previous section and elsewhere [H7]. The analysis of the exchange coupling and of the magneto crystalline anisotropy allows to set up a classical Heisenberg model to study finite temperature effects in the following chapters.

There are two interactions for TM-Fe system. The intrawire and interwire magnetic coupling (as shown in Fig.5.3) will be explored in this study. J_{\parallel} is named for the effective intrachain coupling constant and J_{\perp} for the interchain coupling constant (RKKY coupling).

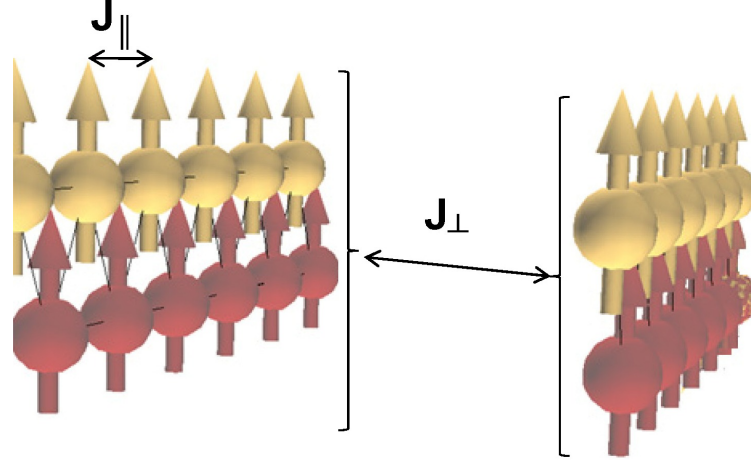


Figure 5.2: Schematic picture showing magnetic interactions of TM-Fe wires. J_{\parallel} : Direct exchange coupling, and J_{\perp} : Indirect exchange coupling (RKKY coupling).

5.2 Theoretical method

Calculation of direct exchange coupling

Computational details and convergence checks are the same as those in the previous chapter. Although, the computational details and convergence checks are different in some aspects. The detailed reason for this difference was given in the second chapter. A supercell containing twelve Cu layers, this corresponds to 72 to 192 Cu atoms (respectively for Cu($n+2,n,n$), $n=2-7$), was constructed to model the Cu(111) stepped surface. Whereas, the terraces are from three to eight lattice constants wide. The distance from one slab to its nearest image was equivalent to 13.5\AA . In all calculations the one-dimensional Brillouin zone was sampled by a $50 \times 1 \times 1$ mesh.

Nearest-neighbor exchange interaction is assumed to define the anisotropic classical Heisenberg Hamiltonian. Anisotropy effects are taken into account by taking the MAE to be 0, 0.01, 0.03, 0.10, 0.30, 1, 3, or 9 meV per site. This does not have any effect on the calculation of exchange couplings. By doing so, it is assumed that the MAE of Fe and the TM sublattices are equal. The intrachain coupling constants have been calculated exploiting supercells, doubled in same of the direction of the wires, and for parallel and antiparallel alignment of the moments in the wire. It is obvious that the second and third terms are always canceled out in the subtraction of the parallel and antiparallel alignments. Therefore,

$$H = - \sum_{i \neq j} J_{ij} \mathbf{S}_i \cdot \mathbf{S}_j - K \sum_i (S_i^z)^2 - \mu \mathbf{B} \cdot \sum_i \mathbf{S}_i \quad (5.1)$$

As mentioned above, $K \sum_i (S_i^z)^2$ and $\mu \mathbf{B} \cdot \sum_i \mathbf{S}_i$ are cancelled out and J_{ij} can be calculated with making parallel and antiparallel alignment of the moments.

Therefore,

$$J_{ij} = \frac{H_{AF} - H_{FM}}{2} \quad (5.2)$$

where J_{ij} is the exchange coupling constant between \mathbf{S}_i and \mathbf{S}_j . H_{AF} and H_{FM} are the DFT total energies calculated for antiparallel alignment of the moments and parallel alignment of the moments, respectively.

Calculation of indirect exchange coupling

The interchain coupling constants have been calculated exploiting supercells doubled in the direction perpendicular to the wires, and for parallel and antiparallel alignment of the moments on the two wires on each side of the supercell.

5.3 Calculation of direct exchange coupling

Three systems were investigated. In freestanding TM chains the atomic distance was constrained to the Cu bond length d_{Cu} of the Cu(111) substrate in order to simulate a freestanding equivalent to the TM chain in the TM-Fe wire on the substrate. A freestanding wire was studied as an equivalent to the one embedded into the Cu(111) surface (cf. Fig. 5.1). All interatomic distances correspond to the Cu bond length of the substrate in this case. The structure of the embedded TM-Fe wire was fully relaxed. The main effect of structural relaxations is an inward relaxation of the TM atoms relative to their ideal positions. For Mn-Fe the inward relaxation of Mn is 16 % (related to Cu lattice plane distance). The Fe chain shows also an inward relaxation of 7 % respectively. Details of the relaxations for all 3d TM-Fe wires are given in the previous chapter.

Central task for the mapping onto a classical Heisenberg model is the determination of exchange constants and magnetocrystalline anisotropy. The exchange constants can be extracted from DFT calculations either by the comparison of total energies of several artificial collinear magnetic structures or by applying the magnetic force theorem in the framework of the Korringa-Kohn-Rostoker (KKR) Green's function method[88, 89]. Also artificial noncollinear structures can be used. The idea is to choose such noncollinear states that exchange interactions in the Heisenberg model can be switched on or off in a controlled manner. Investigations of the freestanding TM chains by means of total energy considerations and magnetic force theorem reveal that the nearest neighbor exchange interaction is the most important one. Already the next-nearest neighbor interaction is an order of magnitude smaller. Therefore we restrict the Heisenberg model to nearest neighbor interactions only. As an example, exchange couplings of next neighbors are calculated for Fe-Fe wire (see Fig. 5.4).

Noncollinear configurations are used to calculate the exchange parameters for freestanding and embedded wires are given in Fig. 5.3. It is checked, that the magnetic moments are constant for the different noncollinear configurations used for a specific system. Noncollinear arrangements being equivalent by symmetry lead to the same exchange parameters. The exchange parameters for all systems calculated by such a procedure are given in Tab. 5.2. The discussion is restricted to V to Co because it was

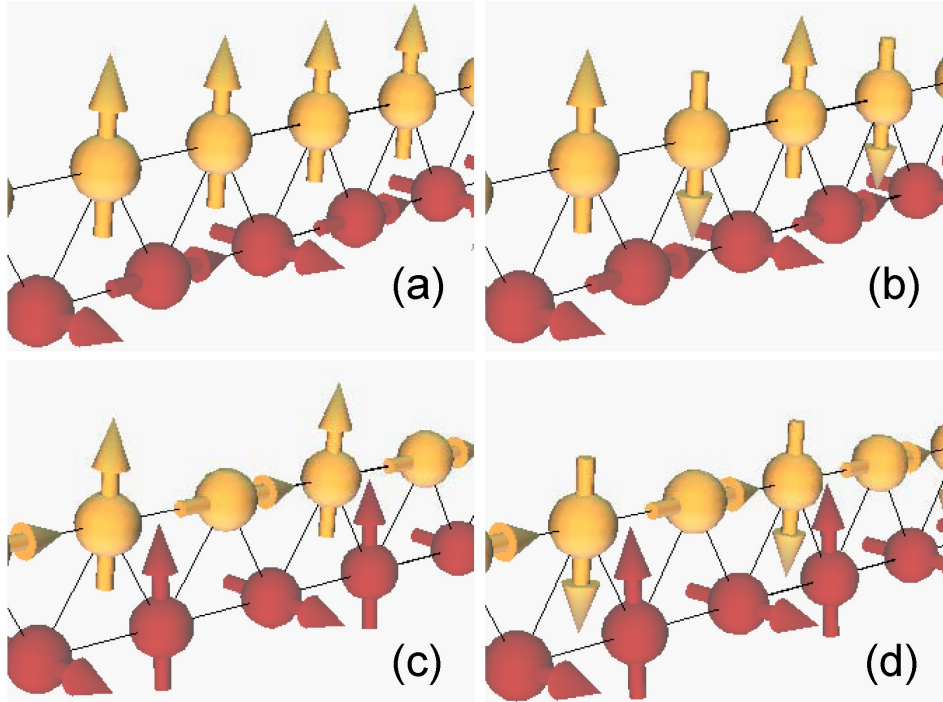


Figure 5.3: (Taken from Ref. H6) Noncollinear arrangement of spin moments to determine exchange constants: (a,b) The spins moments at the Fe atoms (red) are oriented such, that nearest-neighbor interactions in-between the Fe chain and between Fe and TM chain (yellow) cancel out in the Heisenberg Hamiltonian. J_{TM-TM} can be calculated. (c,d) Configurations that allow to calculate the interaction J_{TM-Fe} between the chains.

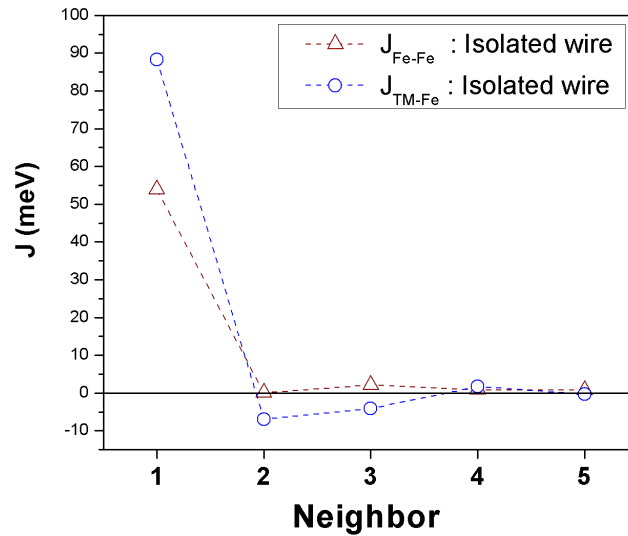


Figure 5.4: Exchange constants calculated for the freestanding Fe-Fe wires (Because the system consists of two Fe chains, there are only two exchange constants. The first, $J_{\text{Fe-Fe}}$ is the coupling between Fe atoms inside the Fe single chain. The second, $J_{\text{TM-Fe}}$ is the coupling between two Fe chains.). The second and third neighbors interactions are an order of magnitude smaller, while for the fourth and fifth neighbors, the interactions are very small and negligible.

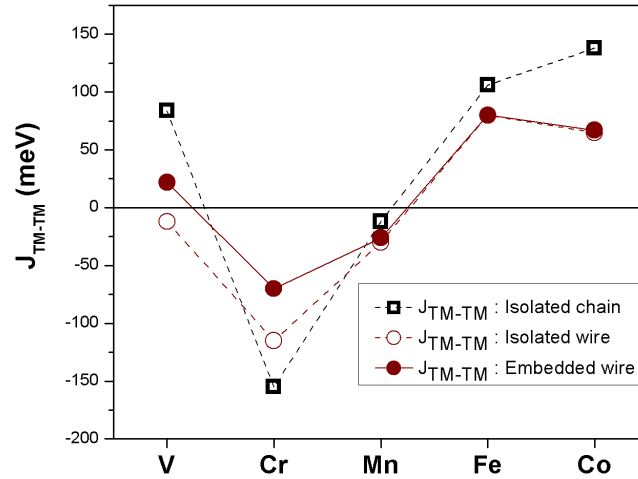


Figure 5.5: TM exchange coupling constants calculated for the freestanding TM chain and TM-Fe and embedded wires. Unfilled signs correspond to the freestanding chain and wire (black and brown, respectively), while the filled signs for the embedded wire.

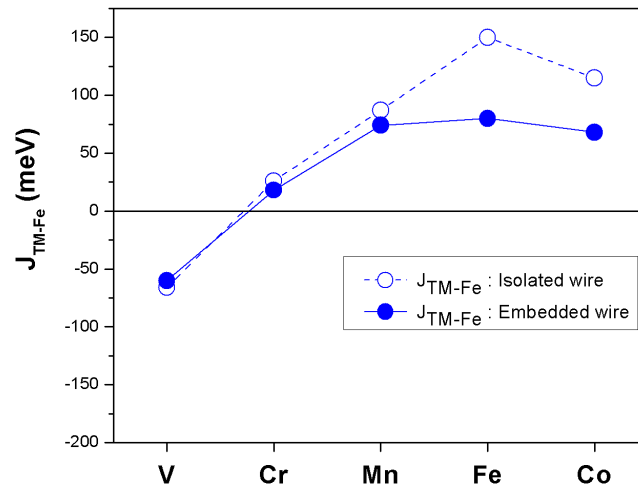


Figure 5.6: TM-Fe exchange coupling constants calculated for the freestanding and embedded TM-Fe wires. Unfilled sign corresponds to the freestanding wire and the filled one to the embedded wire.

Table 5.1: Exchange constants for the freestanding TM chain, freestanding TM-Fe wires, and the embedded TM-Fe wires. The definition of the constants in the Heisenberg model incorporates the magnetic spin moments[H5, H6]. All values are given in meV.

J (meV)	V	Cr	Mn	Fe	Co
<i>freestanding chain</i>					
J_{TM-TM}	84.18	-154.89	-11.90	114.54	138.53
<i>freestanding wire</i>					
J_{TM-TM}	-12.96	-115.83	-30.00	80.33	65.16
J_{TM-Fe}	-79.69	-26.12	86.69	150.42	115.48
J_{Fe-Fe}	48.30	77.80	82.40	80.33	54.20
<i>embedded wire</i>					
J_{TM-TM}	22.30	-69.97	-26.12	79.76	67.37
J_{TM-Fe}	-60.37	17.70	74.34	80.00	68.26
J_{Fe-Fe}	65.07	48.50	58.30	74.58	55.60

not possible to stabilize all necessary magnetic configurations for the other elements. In a previous investigation[90] the magnetic groundstates of such freestanding and embedded wires were investigated for ideal structures by means of collinear spin-polarized DFT calculations. The magnetic groundstates for the free chains are in agreement with the results of Tung and Guo[10] for the relaxed chains with V as an exception. This can be understood easily because the relaxed bond length in the ferromagnetic state is close to the Cu bond length, whereas in the antiferromagnetic ground state the bond length is 20.2% smaller than d_{Cu} . The exchange constants reflect the antiferromagnetic groundstates of Cr and Mn chains. Noncollinear calculations for such 3d-TM chains reveal that the easy axis is the chain direction, with Mn as an exception having the easy axis perpendicular to the chain. The magnetocrystalline anisotropy energy of the chains is in the order of a few meV. The anisotropy energy will be taken as a parameter in the MC calculations which will be discussed in detail in the next chapters.

Some general conclusions can be drawn from Tab. 5.2 and figures 5.5, 5.6 and 5.7. The exchange constants reflect the result that Fe-Fe and Co-Fe wires have a ferromagnetic groundstate in collinear calculations. Antiferromagnetic couplings are present at the beginning of the series. For the freestanding wires J_{Fe-Fe} , is roughly constant through the series. Cr shows a strong antiferromagnetic intrachain coupling, whereas in V-Fe a strong antiferromagnetic interchain coupling is present. Relaxation effects are reflected of course in the exchange constants of the embedded systems. The stronger hybridization due to the inward relaxation of the TM chains leads to a decrease of the interchain exchange constants.

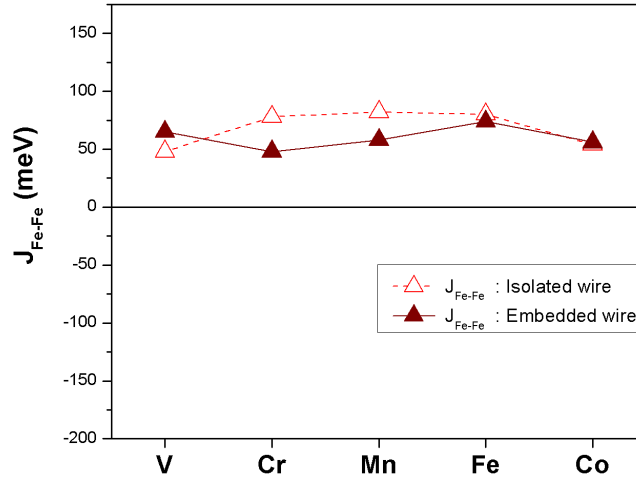


Figure 5.7: Fe-Fe exchange coupling constants calculated for the freestanding and embedded TM-Fe wires. Unfilled sign corresponds to the freestanding wire and the filled one to the embedded wire.

5.4 Calculation of exchange coupling: long range (RKKY) interactions

Bulk

Magnetic moments couple over relatively large distances. However, this coupling is indirect. In this case, the dominant exchange interaction in the metal will be indirect. In metals, the magnetic moments couple through an intermediary which are the conduction electrons (itinerant electrons). This type of exchange was first proposed by Ruderman and Kittel[91] and later extended by Kasuya [92] and Yosida [93]. They constructed a theory that now generally is known as the RKKY interaction. The interaction is characterised by a coupling coefficient, J , given by the following formula

$$J(\mathbf{R}_l - \mathbf{R}_{l'}) = 9\pi \left(\frac{J^2}{\epsilon_F} \right) F(2k_F |\mathbf{R}_l - \mathbf{R}_{l'}|) \quad (5.3)$$

where k_F is the radius of the conduction electron Fermi surface, R_l is the lattice position of the point moment, ϵ_F is the Fermi energy and

$$F(r) = \frac{r \cos r - \sin r}{r^4} \quad (5.4)$$

As one can see in Fig. 5.8, the RKKY exchange coupling oscillates from positive to negative as a function distance between the ions. It has also the damped oscillatory

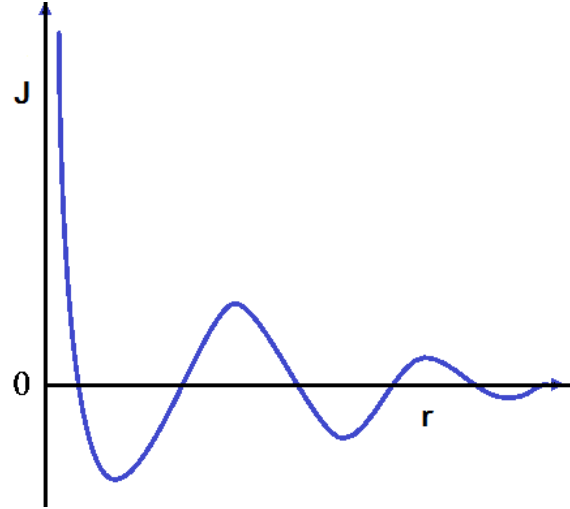


Figure 5.8: Variation of the indirect exchange coupling constant, J , of a free electron gas in the neighbourhood of a point magnetic moment at the origin $r = 0$.

nature. Therefore, depending upon the distance between a pair of ions their exchange coupling can be ferromagnetic or antiferromagnetic. A magnetic ion induces a spin polarisation in the conduction electrons in its neighbourhood. This spin polarisation in the itinerant electrons is felt by the moments of other magnetic ions within range, leading to an indirect coupling.

Fe nanowires RKKY interactions

First, surface states of clean Cu(111) vicinal surfaces have been studied, as discussed in chapter 3. Because such long range interactions have been attributed to the surface states[94, 95]. Based on the calculations presented in Sec. 3.2.4, we concluded that only considering 18 layer slab of Cu or more (i.e. 24 layer slab) produces a band structure which are comparable to experimental energy dispersion. Here, the interwire coupling constants are determined by making parallel and antiparallel alignment of the moments in the Fe wires. This means that the energy differences are calculated not the absolute value of energy itself. As one can see in Fig. 5.9, using 15 and 12 layer slab of Cu, gives a negligible difference for the interwire couplings, obtained for two interwire separations. Therefore, 12 layer slab of Cu is used to model the C(111) and simulate the surface states. A direct relaxation calculation for such a big system is very expensive. Thus, four top most relaxed layers of a 8 layer slab of Cu(111) have been taken and replaced on the corresponding geometry of 12 layer slab of Cu(111) surface, mimicking the relaxed geometry, having the eight bottom layers fixed in their ideal bulk positions. The strength of intrachain magnetic coupling can be deduced from the energy difference of the ferromagnetic and antiferromagnetic oriented wires, with supercells doubled in a direction perpendicular to the wires.

To construct a Heisenberg Hamiltonian which takes into account all the magnetic in-

teractions, the J_{\parallel} , effective intrawire couplings and J_{\perp} , the interchain couplings (RKKY coupling) are required (The anisotropies will be discussed in the next chapter in detail). The effective intrawire couplings were determined in the previous section. Now, we discuss how to estimate the interchain couplings. In principle, there are three interchain coupling constants in the cell. The first is the coupling between the embedded Fe and embedded Fe in the nearest neighboring wire. The second is between the embedded Fe and the deposited Fe at the top position in the nearest neighboring wire and finally between the deposited Fe on top and the deposited Fe at the top position in the nearest neighboring wire. Computationally, this is a demanding task to calculate the mentioned interactions. Since instead of just ferromagnetic and antiferromagnetic configurations, more possible magnetic configurations (they are necessary to make different configurations and extract the exchange couplings from subtracting the configurations energies, but, energetically, may not be favored) have to be constructed. At the end, still, the difference between the calculated interactions may be too small, keeping this question opened whether this tiny difference has any significant effect on the estimated transition temperature. Therefore the current study has been confined with the effective interwire coupling constants. The interchain coupling constants by parallel and antiparallel alignment of the moments on the two wires on each side of the supercell, keeping the moments inside the wires parallel.

The calculated exchange couplings functions of interwire separation are reflected in Fig. 5.9. The intrachain couplings are higher than the interchain couplings, in fact one order of magnitude higher for relatively large interwire separation. The RKKY exchange coupling between the Fe nanowires oscillates from $+27.23 \text{ meV}$ for Cu(422) to -4.78 meV for Cu(533) and from -2.13 meV for Cu(644) to $+1.67 \text{ meV}$ for Cu(755), -2.23 meV for Cu(866), -0.61 meV for Cu(977) and -0.49 meV for Cu(1088). These results are also summarized in Tab. 5.2.

Table 5.2: Exchange coupling constants (J_{\perp}) of Fe wires on Cu(111) stepped surfaces.

Cu(n+2,n,n)	(4,2,2)	(5,3,3)	(6,4,4)	(7,5,5)	(8,6,6)	(9,7,7)	(10,8,8)
$J_{\perp} \text{ (meV)}$	27.23	-4.78	-2.13	1.67	-2.23	-0.61	-0.49

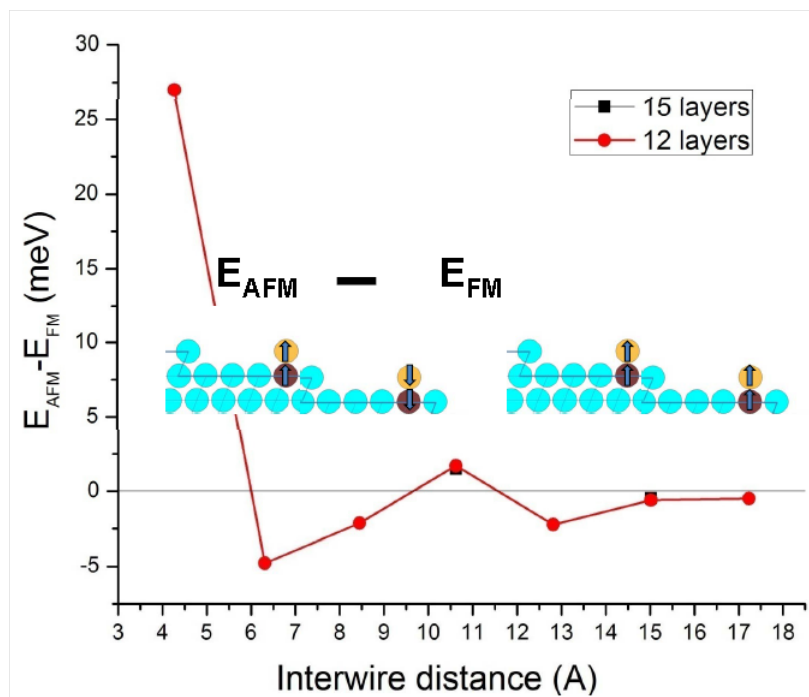


Figure 5.9: Interwire coupling constants of Fe wires as functions of interwire separation.

6 Magnetic Anisotropy Energy

Magnetism at the nanometer scale has been an exciting research areas over the past few decades. This is due to the fundamental and interesting physical properties such as magnetic anisotropy energy. It is known that in crystals, physical properties are generally anisotropic (they are different in different crystallographic directions). Some magnetic properties are also anisotropic, such as easy and hard directions of magnetization. However, there are also isotropic quantities, such as the Curie temperature and the saturation magnetization.

There are two possible reasons for the magnetic anisotropy: the coupling of the electron orbits to the crystalline electric field and the dipole interaction. The first is the magnetocrystalline anisotropy, which is caused by the simultaneous occurrence of the electron spin-orbit interaction and spin-polarization in the magnetic system. This is also known as the electronic contribution. The second one is the magnetostatic (or shape) anisotropy energy due to the magnetic dipolar interaction in the solid.

Recently, there has been great interest in the magnetic anisotropy energy (MAE) of small magnetic nanostructures supported on nonmagnetic substrates to build memory storage devices with a maximal storage density. The minimum magnetic anisotropy energy MAE of 1.2 eV/bit is required to inhibit magnetization reversal for a storage device. Therefore, a reduction of the size of the nanostructures carrying one bit of information requires an increase of the MAE per atom. In the ideal case, having an increased MAE would lead the magnetism from two dimensions (surface) to one dimension (wire) or even a single atom. For example, finite free-standing gold atomic chains were first reported in 1998[96, 97], and their structural properties, such as the actual length of the chain have been the focus of intensive experiments and theoretical studies since then. However, these free-standing atomic chains are unstable and thus can only exist at low temperatures and only on a suitably chosen substrate. Physically, stable magnetic nanowires deposited on metallic substrates are one of the most important nanostructures and a variety of techniques have been used to prepare and study them. For example, Gambardella *et al* [98, 3] succeeded in preparing a high density of parallel atomic chains along steps by growing cobalt on a high-purity Pt(997) vicinal surface (See Fig. 6.1) in a narrow temperature range of 10~20 K. The magnetism of the Co wires was also investigated by the x-ray magnetic circular dichroism.[3] A very large anisotropy energy of MAE=9.3±1.6 meV is determined for Co wires using this experiment. As mentioned above, the extreme case of a system showing magnetic anisotropy is an adatom on a nonmagnetic surface. A high magnetic anisotropy energy requires large spin and orbital magnetic moments and a strong spinorbit coupling. Cobalt has a large spin moment among the ferromagnetic 3d metals. Platinum also has a strong spinorbit coupling. In this case, Co chains supported on substrates of highly polarizable Pt are a viable route

to tune both the spin moments and the anisotropy energy. Therefore, this large MAE has to be attributed to the large spin moment of Co and reduced dimensionality of the Co atom (versus the Co bulk) and to the magnetic moments induced in the Pt substrate combined with the strong spinorbit coupling of the Pt $5d$ states.

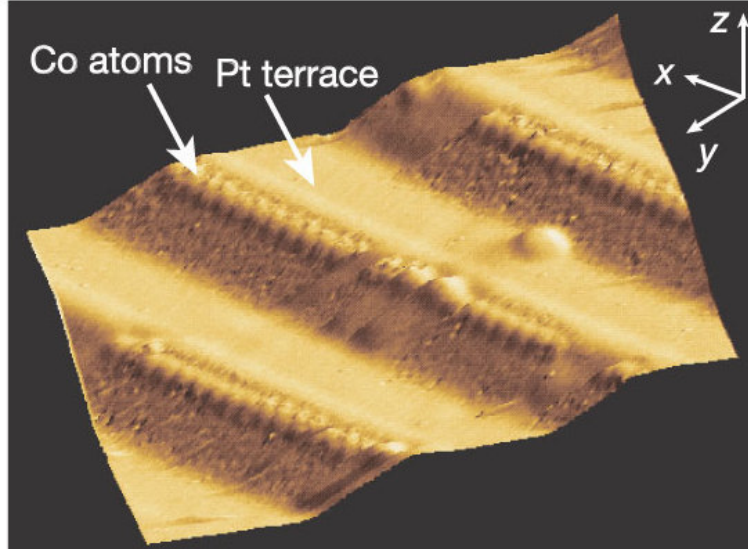


Figure 6.1: STM topographs of the Pt(997) surface (Taken from Ref.[3]): Co monatomic chains decorating the Pt step edges. The chains are linearly aligned and have a spacing equal to the terrace width.

Monoatomic wires have been investigated theoretically in a large number of studies. [99, 18, 100, 101, 102, 103, 104, 105, 106, 107, 108] The lower coordination of the magnetic atoms in such systems located on a metallic surface compared to bulk leads to an enhancement of the moments and a large magnetocrystalline anisotropy can help to stabilize the direction of the magnetic moments. In the Ref. [109, 87, 90, 110] electronic and magnetic properties of transition metal chains is investigated, but with the equilibrium bond length in each case. The presented study is focused on the transition metal chains with the bond length of Cu.

Ab initio studies of the magnetic anisotropy for all $3d$ transition metal (TM) free-standing linear chains [111] revealed that the Fe freestanding linear chains has a massive magnetic anisotropy energy MAE. In Ref. [111] the bond length of transition metal chains is not constrained to the copper bond length. Experimentally, copper and tungsten are good substrates for growth of Fe thin films.[112, 113] Also, as discussed in details in Chp. (4) TM-Fe wires can be formed on Cu(111) stepped surface. Thus, in this chapter, first principles calculations for the magnetic anisotropy energies of the M-Fe wires (M=ScNi) on vicinal Cu(111) surface have been carried out.

In this chapter, *ab initio* density-functional calculations including spinorbit coupling (SOC) have been performed to calculate the magnetic anisotropy energies, including magnetocrystalline and shape anisotropies of TM-Fe wires in both isolated and de-

posited cases. The TM-Fe structures have been optimized for different orientations of the magnetization with respect to the crystallographic axes of the systems. The magnetic anisotropy energies and the anisotropies of spin and orbital moments have been determined. Particular attention has been paid to the correlation between the geometric and magnetic structures as discussed in detail in Chp. (4). The Fe-Fe and Mn-Fe wires exhibit a large magnetic anisotropy energy, indicating that these nanowires would have applications in high density magnetic data storages. The substrate effect on the MAE of the wires are discussed in this chapter.

The rest of this chapter is organized as follows: In the next section, a brief description of the theory and computational details is given. Then, in Sec. (6.3), magnetocrystalline and shape anisotropy energies of the linear $3d$ transition metal chains are presented. The calculated magnetic anisotropy energies and moments of TM-Fe wires on Cu(111) stepped surface are presented in Sec. (6.3). Finally, the magnetic properties of TM-Fe wires at finite temperatures are discussed in Sec. (6.4).

6.1 Theoretical method

Computational details and convergence checks are the same as those in the previous chapter, although the computational details and convergence checks are different in some aspects. A large plane-wave cutoff energy of 340 eV is used for all $3d$ transition metal chains. The Methfessel-Paxton scheme [114] is employed for Brillouin zone integrations. The convergence of the calculated properties with respect to number of k -points and supercell size was carefully checked. For the linear chains, the nearest wire-wire distance between the neighboring chains is, at least, 13 Å. Because of its smallness, *ab initio* calculation of the MAE is computationally very demanding and needs to be carefully carried out. Here we use the total energy difference approach rather than the widely used force theorem to determine the MAE, i.e., the MAE is calculated as the difference in the full self-consistent total energies for the two different magnetization directions (e.g., parallel and perpendicular to the chain) concerned. Because MAE is a delicate and controversial effect, we made sure that our broad conclusions are approach-independent by performing calculations with two different software packages. What are presented here are only the results obtained with the VASP code. The total energy convergence criterion is 10^{-6} eV/atom. The MAEs calculated with a dense $32 \times 6 \times 1$ k -point mesh with $\sigma=0.001$ eV hardly differ from that obtained with the $20 \times 5 \times 1$ k -point mesh (within 0.02 meV). The same k -point mesh is used for the band structures and density of states calculations.

To verify the MAE results with another method, the all-electron full-potential linear augmented plane wave (FP-LAPW) method is also used as implemented in the WIEN2K code [115] and the generalized gradient approximation (GGA).

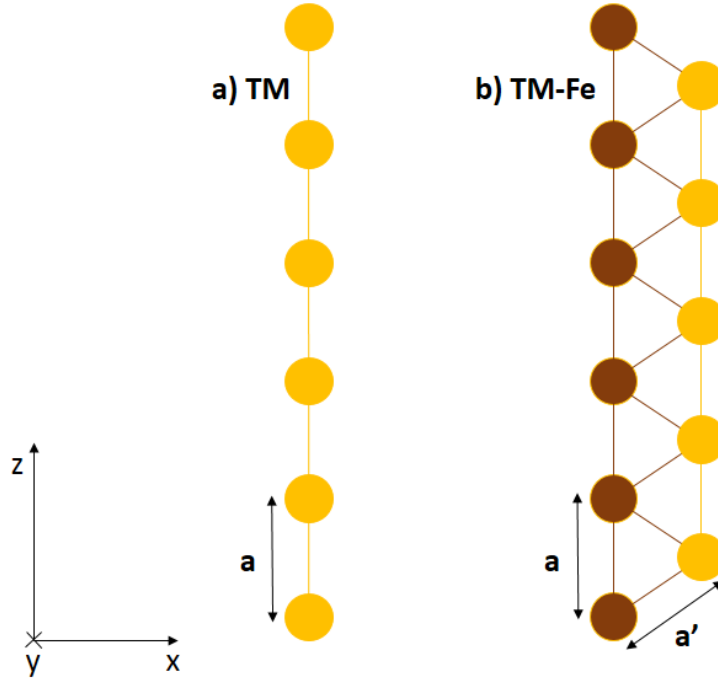


Figure 6.2: Schematic structure diagram for (a) the isolated TM chain and (b) TM-Fe wire.

6.2 Spin-orbit coupling and orbital magnetic moment

The spin-orbit coupling (SOC) is necessary for the orbital magnetization and magnetocrystalline anisotropy in solids, however it may be weak in the $3d$ transition metals. Thus, it was taken into account in the self-consistent calculations presented here.

TM chains

With taking into account the SOC, the spin moments for the isolated $3d$ transition chains become $3.02 \mu_B$ (V), $3.99 \mu_B$ (Cr), $4.01 \mu_B$ (Mn), $3.24 \mu_B$ (Fe), $2.23 \mu_B$ (Co), respectively. These values are almost identical to the corresponding ones obtained without the SOC. This is due to the weakness of the SOC in the $3d$ transition metals. However, including the SOC does give rise to a significant orbital magnetic moment in some atomic chains and, importantly, allows us to determine the easy magnetization axis for these $3d$ atomic chains. As summarized in Tab. (6.1), for the magnetization along the chain direction, the calculated orbital magnetic moments in the FM state are 0.41 and $0.55 \mu_B/\text{atom}$ for the Fe and Co chains, respectively, though they are only 0.02 , 0.01 and $0.02 \mu_B/\text{atom}$ for the V, Cr and Mn chains, respectively. The orbital moments in the Fe and Co atomic chains are, therefore, considerably enhanced, when compared with the bulk materials [116], and are also larger than the orbital moments in the Fe and Co monolayers [117].

The spin moment is found to be unaffected when the SOC is taken into account even in the $4d$ [118, 1, 119, 120] and $5d$ [107] TM linear atomic chains. Nonetheless, the SOC contributes to apparent orbital moments in all three cases. It was shown in some studies [118, 111] that the orbital moment increases significantly with the bond length and has a strong dependence on the magnetization orientation. As summarized in Tab. (6.1), the orbital moment for the magnetization along the chain is higher than that for the magnetization perpendicular to the chain for V, Fe, and Co. This is in contrast with the orbital moments estimated for the magnetization along the chain which is lower than that for the magnetization perpendicular to the chain for Cr and Mn. The orbital moments of the V, Fe, and Co chains with a perpendicular magnetization are 0.02, 0.41, and $0.55 \mu_B$, respectively. The orbital moments of the Cr and Mn with a magnetization along the chain are only 0.03 and $0.07 \mu_B$, respectively. This anisotropy in the orbital moment is especially pronounced in the Fe and Co chains. It is well known that in general, the magnetization direction with a larger orbital moment, would be lower in total energy. Therefore, the easy magnetization direction in the V, Fe, and Co chains is expected to be along the chain, as will be reported in Sec. (6.3). It is noticeable that the presented results for the spin and orbital moments are in good agreement with previous calculations for the $3d$ atomic chains [118, 111].

Table 6.1: Spin (m_s) and orbital (m_o) magnetic moments (in μ_B/atom) of the magnetic $3d$ transition metal linear chains at the Cu bond lengths with magnetization parallel ($\mathbf{M} \parallel \hat{z}$) and perpendicular ($\mathbf{M} \perp \hat{z}$) to the chain axis.

		$\mathbf{M} \parallel \hat{z}$		$\mathbf{M} \perp \hat{z}$	
		m_s	m_o	m_s	m_o
V	(FM)	3.02	0.02	3.01	0.01
Cr	(AF)	3.99	0.01	4.00	0.03
Mn	(AF)	4.01	0.02	4.07	0.07
Fe	(FM)	3.24	0.41	3.15	0.19
Co	(FM)	2.23	0.55	2.18	0.47

TM-Fe wires

As discussed in Chp. (4), all the isolated TM-Fe wires have magnetic solutions and as summarized in Tab. (6.2), the V-Fe wire is most stable in the FF state, whilst the ground state of the Cr-Fe wire is the AF state and the Mn-Fe, Fe-Fe and Co-Fe wires have the FF ground state (See Fig. (4.7)).

The spin magnetic moments in the isolated TM-Fe wires are generally smaller than in the corresponding TM single chains. This is due to the increase in the coordination number in the TM-Fe wires. When the SOC is taken into account, the spin magnetic moments of the TM-Fe wires slightly change, as for the linear chain cases. The orbital magnetic moments of the TM-Fe wires with the magnetization along the z-axis (easy

Table 6.2: Spin (m_s) and orbital (m_o) magnetic moments (in μ_B/atom) of the TM-Fe wires with magnetization \mathbf{M} in \hat{x} , \hat{y} and \hat{z} directions.

		\hat{x}		\hat{y}		\hat{z}	
		m_s	m_o	m_s	m_o	m_s	m_o
V-Fe	(FF)	2.59	0.00	2.59	0.01	2.61	0.02
Cr-Fe	(AF)	3.49	0.01	3.50	0.00	3.53	0.03
Mn-Fe	(FF)	4.06	0.01	4.07	0.01	4.07	0.02
Fe-Fe	(FF)	3.04	0.01	3.04	0.09	3.05	0.14
Co-Fe	(FF)	2.03	0.03	2.04	0.11	2.04	0.17

magnetization axis) are 0.02 (V), 0.03 (Cr), 0.02 (Mn), 0.14 (Fe) and 0.17 (Co) μ_B which are significantly smaller than that of the corresponding linear single chains.

6.3 Magnetic anisotropy energy (MAE)

The total energy of the orientation dependent magnetization $\mathbf{M}(\phi, \theta)$ of a TM wires (see Fig. (6.3)) in the lowest non-vanishing terms can be written [111] as

$$E_t = E_0 + \sin^2\theta(E_1 - E_2\cos^2\phi) \quad (6.1)$$

where θ is the polar angle of the magnetization \mathbf{M} from the wire axis (z -axis) and ϕ is the azimuthal angle in the $x - y$ plane perpendicular to the wire, measured from the x axis. For the isolated chain, the azimuthal anisotropy energy constant E_2 is zero, because of the rotational invariance. The axial anisotropy energy E_1 is calculated by the total energy difference between the magnetization along the $y(x)$ and z axes, i.e., $E_1 = E^y - E^z$ ($E^x = E^y$). If E_1 is positive, it would mean that the chain (z) axis is the easy magnetization axis. For the TM-Fe wires which are in the $x - z$ plane, E_2 is not zero and can be calculated as the total energy difference between the magnetization along the x and y axes, i.e., $E_2 = E^y - E^x$.

As mentioned earlier, the magnetic anisotropy energy for a magnetic solid has two contributions, which are the magnetocrystalline and shape anisotropy energies. It is known that the shape anisotropy energy is zero for the cubic systems such as bcc Fe and fcc Ni, and also very small for the solids such as hcp Co. However, the shape anisotropy energy is comparable to the magnetocrystalline energy for the anisotropic structures such as magnetic Fe and Co monolayers [117, 121]. The shape anisotropy is calculated by a sum over classical dipole-dipole energies in the system. Each of the individual terms may not sound to have a significant contribution to the MAE. However, the dipole-dipole interactions are long-ranged and a sum over the whole magnetic material, makes the dipolar interactions non-negligible for anisotropic structures.

Furthermore, as will be discussed in detail later, the shape anisotropy energy of the $3d$

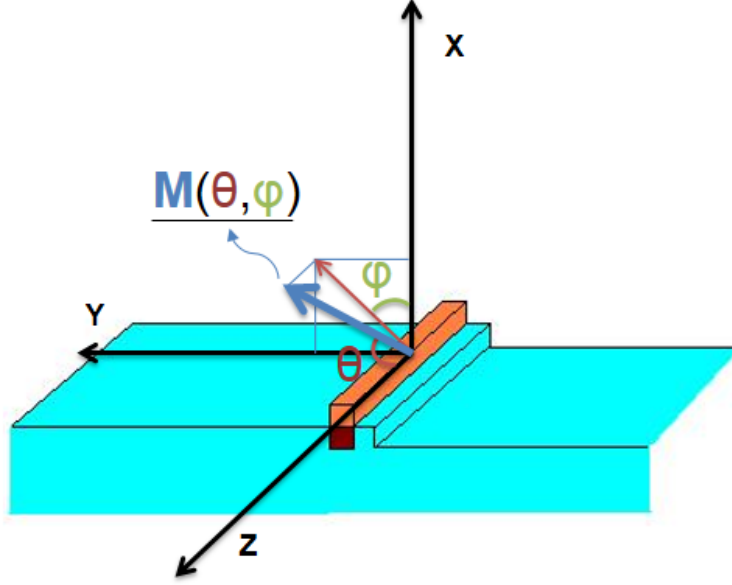


Figure 6.3: Schematic representation of the magnetization orientation (θ, ϕ) of a TM-Fe wire on the vicinal surface.

TM chains and TM-Fe wires are also non-negligible. Therefore, their magnetic dipole-dipole interaction energies are calculated.

In order to check possible collinearity between the Fe and TM magnetic moments ($\mathbf{M}_{TM} \parallel \mathbf{M}_{Fe}$), using the all-electron full-potential linear augmented plane wave (FP-LAPW), fully relaxed magnetic structures have been calculated. The ground state calculations estimated collinear magnetic structure for TM-Fe wires on Cu(111) stepped surface. However, there is a negligible angle between the Fe and TM magnetic moments. This angle does not reach to 2° for any of TM-Fe wires. Therefore, the magnetic anisotropy energy calculations are restricted to the collinear cases in the present chapter.

For the collinear magnetic systems, this magnetic dipolar energy (E^d) is given by (in atomic Rydberg units)

$$E^d = \sum_{qq'} \frac{m_q m_{q'}}{c^2} M_{qq'} \quad (6.2)$$

and

$$M_{qq'} = \sum_{\mathbf{R}}' \frac{1}{|\mathbf{R} + \mathbf{q} + \mathbf{q}'|^3} \left\{ 1 - 3 \frac{[(\mathbf{R} + \mathbf{q} + \mathbf{q}') \cdot \hat{\mathbf{m}}_{\mathbf{q}}]^2}{|\mathbf{R} + \mathbf{q} + \mathbf{q}'|^2} \right\} \quad (6.3)$$

where $M_{qq'}$ is called the magnetic dipolar Madelung constant. The speed of light $c = 274.072$. \mathbf{R} are the lattice vectors, \mathbf{q} are the atomic position vectors in the unit cell and m_q is the atomic magnetic moment on site q . Note that in atomic Rydberg units, one Bohr magneton (μ_B) is $\sqrt{2}$.

The dipolar energy convergence criterion of 10^{-6} eV/atom was reached by taking 300 terms (300 neighboring magnetic moments) of Eq. (6.3).

Free-standing TM chains

Table 6.3: Total (E_1^t), electronic (E_1^e) and dipolar (E_1^d) magnetic anisotropy energies (in meV/atom) of the $3d$ transition metal linear chains for the ground state magnetic structure (MS). If E_1^t is positive, the easy magnetization axis is along the chain; otherwise, the easy magnetization axis is perpendicular to the chain.

	MS	E_1^t	E_1^e	E_1^d
V	(FM)	1.62	0.88	0.74
Cr	(AF)	-1.29	-0.32	-0.97
Mn	(FM)	1.04	-0.27	1.31
Fe	(FM)	5.69	4.83	0.86
Co	(FM)	2.72	2.31	0.41

The calculated electronic (E_1^e) and shape anisotropy (E^d) energies for the free-standing TM chains, free-standing TM-Fe wires and TM-Fe wires on Cu(111) stepped surface are listed in Tables (6.3), (6.4) and (6.5), respectively. Table (6.3) shows MAEs for the single $3d$ TM chains of their ground states. It is noticeable that the shape anisotropy energies can be comparable to the electronic contributions. Furthermore, V, Mn, Fe and Co ($3d$ elements with FM ground state) prefer the chain direction ($\mathbf{M} \parallel \hat{z}$) as the easy magnetization axis. For the FM chains, this may be expected since the shape anisotropy energy always favors the direction of the longest dimension. Therefore, any perpendicular magnetic anisotropy should originate from the electronic magnetocrystalline anisotropy when it is sufficiently large to overcome the shape anisotropy. Cr chain (AF state) prefers the perpendicular magnetic anisotropy ($\mathbf{M} \perp \hat{z}$) as the easy magnetization axis. This conclusion can be drawn that for an AF chain the shape anisotropy energy favors the perpendicular direction to the longest dimension.

Interestingly, Table (6.3) exhibits that in the FM linear chains, the electronic anisotropy energy would favor a perpendicular anisotropy in the Cr and Mn chains but prefer the chain axis in the V, Fe and Co chains. Nevertheless, the easy magnetization direction is predicted to be the chain axis in all the $3d$ FM chains except Mn. But the perpendicular electronic anisotropy in the Mn chain is not sufficiently large to overcome the axial shape anisotropy. In the AF state, Cr chains would have the easy axis perpendicular to the chain. Remarkably, the Fe chain with MAE of 5.69 meV has a large axial anisotropy energy, being in the same order of magnitude of that in the $4d$ transition metal linear chains [118, 122]. In the $4d$ transition metals, the SOC splittings are large, being about ten times larger than the $3d$ transition metals, and thus the large MAE in the $4d$ transition metal linear chains may be expected. The axial anisotropy energy for the V, Cr, Fe and Co chains are also generally larger than the corresponding monolayers. [117, 121]

TM-Fe wires

Table 6.4: The total (E_1^t , E_2^t), electronic (E_1^e , E_2^e) and dipolar (E_1^d , E_2^d) magnetic anisotropy energies (in meV/atom) as well as the easy magnetization axis (\mathbf{M}) of the Free-standing TM-Fe wires for the ground state magnetic structure (MS). $E_1 = E^y - E^z$; $E_2 = E^y - E^x$.

	MS	E_1^e	E_2^e	E_1^d	E_2^d	E_1^t	E_2^t	\mathbf{M}
V-Fe	(FF)	4.42	-0.08	0.27	-0.11	4.69	-0.19	z
Cr-Fe	(AF)	3.33	-0.77	-0.04	-0.14	3.29	-0.91	z
Mn-Fe	(FF)	2.37	-0.74	0.65	0.18	3.02	-0.56	z
Fe-Fe	(FF)	1.39	0.07	0.51	0.14	1.90	0.21	z
Co-Fe	(FF)	1.92	0.55	0.38	0.09	2.30	0.64	z

The axial magnetic anisotropy energy E_1 of the free-standing TM-Fe wires with the magnetization along the z -axis (easy magnetization axis) are 4.42 (V), 3.33 (Cr), 2.37 (Mn), 1.39 (Fe) and 1.92 (Co) meV. E_1 in the Fe and Co chains becomes smaller as the structures change from the chains to the wires. The magnetic anisotropy energies in the V-Fe, Cr-Fe and Mn-Fe are considerably enhanced compared with those in the linear V, Cr and Mn chains, respectively. The most dramatic reduction in the magnetic anisotropy occurs in the Fe chain. The axial anisotropy constant E_1 in the Fe-Fe wire is almost three times smaller than that in the linear Fe chain. In contrast, the most noticeable increase happens in the V chain. E_1 in the V-Fe wire is about three times larger than that in the V chain. The shape anisotropy energy (E_1^d) energies become generally smaller as the structure changes from the $3d$ TM chain to the TM-Fe wire. However due to this structure change the sign of E_1^d does not alter.

There is also a significant magnetic anisotropy energy (E_2) in the $x - y$ plane perpendicular to the z axis (wire). E_2^d (however relatively smaller than E_1^d) also appears in the $x - y$ plane. For the Fe-Fe and Co-Fe wires, the x axis is favored, i.e., the y axis would be the hard magnetization axis. In contrast, for the V-Fe, Cr-Fe and Mn-Fe wires the x axis would be the hard axis (see Table (6.4)).

An isolated transition metal atoms have large spin and orbital magnetic moments according to Hund's rules. However, electron delocalization and crystal field effects compete with the intra-atomic Coulomb interactions causing an overall decrease of spin moment and quenching of orbital moment in TM impurities dissolved in nonmagnetic metal hosts. Theoretical calculations also predict such effects to be strongly reduced at surfaces owing to the decreased coordination of TM impurities[123].

The substrate has expectedly a significant effect on the MAEs in this study as well, as reflected in the calculations. For the deposited V-Fe, Cr-Fe, Mn-Fe and Fe-Fe wires, the x axis is favored. This makes the y axis to be the hard magnetization axis. In contrast, only for the Co-Fe wire the x axis is the hard axis (see Table (6.5)). In other words, the V-Fe, Cr-Fe, Mn-Fe and Fe-Fe wires have an out-of-plane magnetic

Table 6.5: The total (E_1^t, E_2^t), electronic (E_1^e, E_2^e) and dipolar (E_1^d, E_2^d) magnetic anisotropy energy constants (in meV/atom) as well as the easy magnetization axis (\mathbf{M}) of the TM-Fe wires on Cu(111) stepped surface for the ground state magnetic structure (MS). $E_1 = E^y - E^z$; $E_2 = E^y - E^x$, see Eq. (2).

	MS	E_1^e	E_2^e	E_1^d	E_2^d	E_1^t	E_2^t	\mathbf{M}
V-Fe	(FF)	1.03	0.90	0.16	-0.19	1.19	0.71	x
Cr-Fe	(AF)	1.09	0.44	-0.08	-0.11	1.01	0.33	x
Mn-Fe	(FF)	5.15	0.31	0.57	0.17	5.72	0.48	x
Fe-Fe	(FF)	4.32	0.89	0.44	0.15	4.76	1.04	x
Co-Fe	(FF)	0.88	-1.61	0.33	0.11	1.21	-1.50	z

anisotropy whilst the Co-Fe has an in-plane anisotropy. Experimentally, Shen *et al.*[5, 6] also demonstrated that Fe nanostripes on Cu(111) vicinal surface were characterized by a perpendicular anisotropy. Similarly, Tung *et al.*[124] also found that the Fe wire presents a perpendicular magnetic anisotropy while the Co wire shows an in-plane anisotropy on Cu(001) surface.

6.4 Magnetism at Finite Temperatures

It is necessary to calculate some well-defined macroscopic property which ensures the correct implementation of interactions in a system. The Curie temperature T_c of a nanowire is primarily determined by the strength of the exchange interaction between spins and the magnetic anisotropy energies. For the Monte Carlo simulations, lattices with 5200 sites representing the atoms of the single wire were used. Nearest-neighbour exchange interaction is assumed to define the classical Heisenberg Hamiltonian. Anisotropy is also taken into account by taking the MAE to be 0, 0.01, 0.03, 0.10, 0.30, 1, 3, or 9meV. By doing so it is assumed that the MAE of Fe and the TM sublattices are equal. Periodic boundary conditions in direction of the wire are applied. To find the critical temperature the system is first relaxed into thermodynamical equilibrium using 20,000 MC steps per temperature step. Then averaging is done over 30,000 measurements, between each of which three MC steps were performed in order to reduce correlation effects. To improve the statistics averaging over at least ten of such temperature loops is performed. Importance sampling is done using the Metropolis algorithm. Critical temperatures are determined using the specific heat and, in case of a ferromagnetic system, the susceptibility χ and 4th-order-cumulant U_4 .

Figure 6.4 shows the susceptibility for an embedded Mn-Fe wire calculated for different magnetocrystalline anisotropy. In increasing anisotropy stabilizes the moments against thermal fluctuation and leads to an increase of the critical temperature. The calculated critical temperatures are well below room temperature for all systems. A summary of the critical temperatures T_c 's of all systems for MAE = 1.00meV can be found in Table 6.6.

Table 6.6: Critical temperatures for the freestanding and embedded TM-Fe chains for MAE = 1.00meV. The error is approximately $\pm 10\%$.

T_c [K]	V	Cr	Mn	Fe	Co
freestanding wire	100	20	132	68	75
embedded wire	88	41	63	122	94

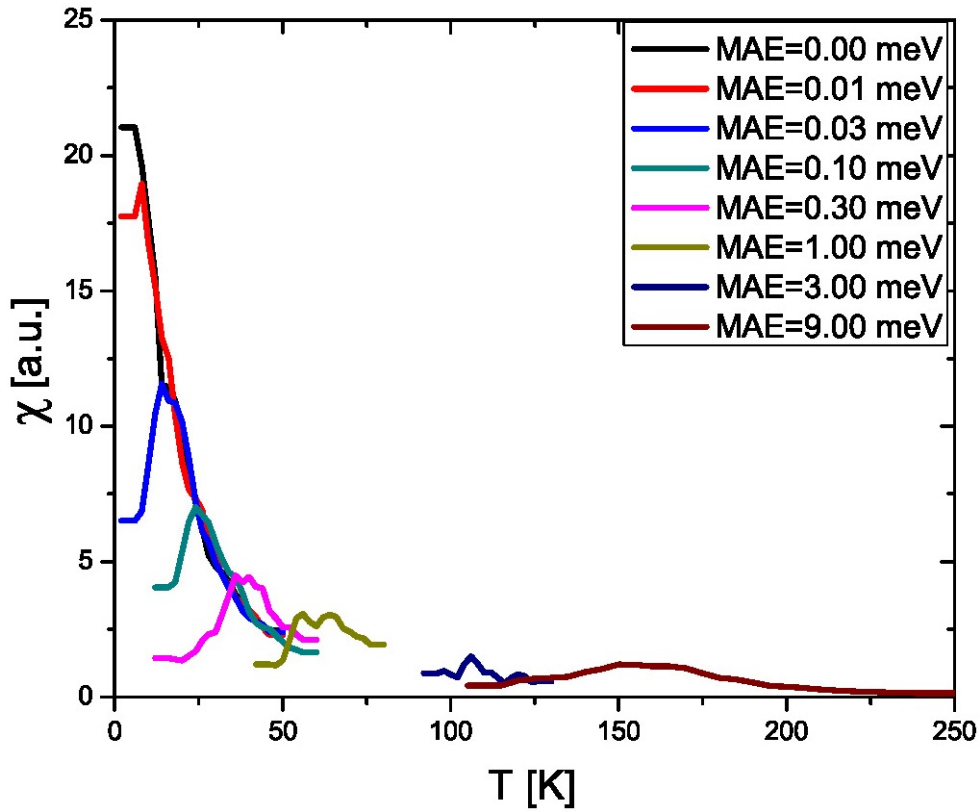


Figure 6.4: (Taken from Ref. H6) Magnetic susceptibility of the embedded Mn-Fe wire for different values of MAE.

Conclusions

The physical properties such as surface energies, structural relaxations, work functions, and surface states of the Cu(111) surface are studied within the framework of DFT. The results obtained for the surface energies, structural relaxations, and work functions using a 6-layer slab are comparable with experimental values. This is not the case for the surface states calculations. The number of layers should be increased to at least 18 in order to obtain surface states. 18-layer slab produces the band structures which are comparable with the experimentally measured energy dispersion.

First-principles calculations are performed in order to study the magnetic states of TM-Fe wires on the vicinal Cu surface. The Fe chain near the step of the Cu(111) surface is the template for the formation of TM chains in atop position of the Fe chain. Ferromagnetic Mn, Fe, Co, and Ni as well as antiferromagnetic structures Cr are achieved using the embedded Fe wire near the step as a template. The antiferromagnetic structure of Cr is very robust. Therefore, the formation of long antiferromagnetic Cr chains on top of the Fe template chain should be experimentally feasible. Stress could be used to prepare Mn-Fe wires in ferromagnetic or antiferromagnetic structure.

The intrawire and interwire magnetic coupling are explored in this study. The effective intrawire coupling constants are extracted from the non-collinear DFT calculations, while the interwire coupling constants are obtained from the regular DFT calculations. The intrawire coupling constants show that Fe-Fe and Co-Fe wires have a ferromagnetic groundstate. Antiferromagnetic couplings are present at the beginning of the series. Cr shows a strong antiferromagnetic intrachain coupling, whereas in V-Fe a strong antiferromagnetic interchain coupling is present. Relaxation effects are discussed. The stronger hybridization due to the inward relaxation of the TM chains leads to a decrease of the interchain exchange constants. The interwire exchange couplings, as functions of interwire separation, are calculated. The intrawire couplings are at least one order of magnitude higher than the interwire couplings.

Non-collinear spin-polarized DFT is employed to calculate magnetocrystalline and shape anisotropy energies of TM-Fe wires in both isolated and deposited cases. The TM-Fe structures are optimized for different orientations of the magnetization with respect to the crystallographic axes of the systems. The magnetic anisotropy energies and the anisotropies of spin and orbital moments are determined. The Fe-Fe and Mn-Fe wires exhibit a large magnetic anisotropy energy, indicating that these nanowires would have applications in high density magnetic data storages.

Ab initio DFT calculations are used to set up classical Heisenberg model to study finite temperature properties of TM-Fe wires embedded on Cu(111). The critical temperatures of the systems are well below room temperature.

Bibliography

- [1] A. Delin, E. Tosatti, and R. Weht. Magnetism in atomic-size palladium contacts and nanowires. *Phys. Rev. Lett.*, 92:057201, Feb 2004.
- [2] A. Smogunov, A. Dal Corso, A. Delin, R. Weht, and E. Tosatti. Colossal magnetic anisotropy of monatomic free and deposited platinum nanowires. *Nat. Nanotechnol.*, 3(1):22–25, Jan 2008.
- [3] P. Gambardella, A. Dallmeyer, K. Maiti, M. C. Malagoli, W. Eberhardt, K. Kern, and C. Carbone. Ferromagnetism in one-dimensional monatomic metal chains. *Nature*, 416(21):301, 2002.
- [4] Cyrus F. Hirjibehedin, Christopher P. Lutz, and Andreas J. Heinrich. Spin Coupling in Engineered Atomic Structures. *Science*, 312(5776):1021–1024, 2006.
- [5] J. Shen, R. Skomski, M. Klaua, H. Jenniches, S. Sundar Manoharan, and J. Kirschner. Magnetism in one dimension: Fe on Cu(111). *Phys. Rev. B*, 56(5):2340–2343, Aug 1997.
- [6] J. Shen, M. Klaua, P. Ohresser, H. Jenniches, J. Barthel, Ch. V. Mohan, and J. Kirschner. Structural and magnetic phase transitions of Fe on stepped Cu(111). *Phys. Rev. B*, 56(17):11134–11143, Nov 1997.
- [7] Jiandong Guo, Yina Mo, Efthimios Kaxiras, Zhenyu Zhang, and H. H. Weitering. Formation of monatomic Fe chains on vicinal Cu(111) surfaces: An atomistic view. *Phys. Rev. B*, 73(19):193405, 2006.
- [8] Samir Lounis, Peter H. Dederichs, and Stefan Blügel. Magnetism of nanowires driven by novel even-odd effects. *Phys. Rev. Lett.*, 101(10):107204, 2008.
- [9] B. Lazarovits, L. Szunyogh, P. Weinberger, and B. Újfalussy. Magnetic properties of finite Fe chains at fcc Cu(001) and Cu(111) surfaces. *Phys. Rev. B*, 68(2):024433, 2003.
- [10] J. C. Tung and G. Y. Guo. Systematic ab initio study of the magnetic and electronic properties of all 3d transition metal linear and zigzag nanowires. *Phys. Rev. B*, 76(9):094413, 2007.
- [11] C. Ataca, S. Cahangirov, E. Durgun, Y.-R. Jang, and S. Ciraci. Structural, electronic, and magnetic properties of 3d transition metal monatomic chains: First-principles calculations. *Phys. Rev. B*, 77(21):214413, 2008.

Bibliography

- [12] Y. Mokrousov, G. Bihlmayer, S. Blügel, and S. Heinze. Magnetic order and exchange interactions in monoatomic 3d transition-metal chains. *Phys. Rev. B*, 75(10):104413, 2007.
- [13] Yina Mo, Wenguang Zhu, Efthimios Kaxiras, and Zhenyu Zhang. Electronic nature of step-edge barriers against adatom descent on transition-metal surfaces. *Phys. Rev. Lett.*, 101(21):216101, 2008.
- [14] D. Spišák and J. Hafner. Fe nanowires on vicinal Cu surfaces: Ab initio study. *Phys. Rev. B*, 65(23):235405, 2002.
- [15] D. Spišák and J. Hafner. Magnetism of ultrathin wires suspended in free space and adsorbed on vicinal surfaces. *Phys. Rev. B*, 67(21):214416, 2003.
- [16] D. Spišák and J. Hafner. Magnetism of monoatomic wires on vicinal surfaces. *Comput. Mater. Sci.*, 27(1-2):138–150, 2003.
- [17] D. Spišák and J. Hafner. Magnetism of ultrathin nanowires: ab initio study. *Comput. Mater. Sci.*, 30(3-4):278–282, 2004.
- [18] Yina Mo, Kalman Varga, Efthimios Kaxiras, and Zhenyu Zhang. Kinetic pathway for the formation of Fe nanowires on stepped Cu(111) surfaces. *Phys. Rev. Lett.*, 94(15):155503, 2005.
- [19] L. Hammer, W. Meier, A. Schmidt, and K. Heinz. Submonolayer iron film growth on reconstructed Ir(100)–(5 × 1). *Phys. Rev. B*, 67(12):125422, Mar 2003.
- [20] P. Segovia, D. Purdie, M. Hengsberger, and Y. Baer. Observation of spin and charge collective modes in one-dimensional metallic chains. *Nature (London)*, 402(19):504–507, May 1999.
- [21] David Serrate, Paolo Ferriani, Yasuo Yoshida, Saw-Wai Hla, Matthias Menzel, Kirsten von Bergmann, Stefan Heinze, Andre Kubetzka, and Roland Wiesendanger. Imaging and manipulating the spin direction of individual atoms. *Nat. Nanotechnol.*, 5(5):350–353, May 2010.
- [22] X. Tan, G. Ouyang, and G. W. Yang. Ordering Fe nanowire on stepped Cu(111) surface. *Appl. Phys. Lett.*, 88(26):–, 2006.
- [23] P. Hohenberg and W. Kohn. Inhomogeneous electron gas. *Phys. Rev.*, 136(3B):B864–B871, Nov 1964.
- [24] W. Kohn and L. J. Sham. Self-consistent equations including exchange and correlation effects. *Phys. Rev.*, 140(4A):A1133–A1138, Nov 1965.
- [25] V. Fock. Näherungsmethode zur Lösung des quantenmechanischen Mehrkörperproblems. *Zeitschrift für Physik A Hadrons and Nuclei*, 61(1):126–148, Jan 1930.

Bibliography

- [26] J. C. Slater. A simplification of the Hartree-Fock method. *Phys. Rev.*, 81(3):385–390, Feb 1951.
- [27] L. H. Thomas. The calculation of atomic fields. *Math. Proc. Cambridge*, 23:542–548, 0 1927.
- [28] E. Fermi. Eine statistische Methode zur Bestimmung einiger Eigenschaften des Atoms und ihre Anwendung auf die Theorie des periodischen Systems der Elemente. *Zeitschrift für Physik*, 48(1-2):73–79, 1928.
- [29] L. I. Schiff. *Quantum Mechanics*. McGraw-Hill, 1986.
- [30] JP Perdew, A Ruzsinszky, JM Tao, VN Staroverov, GE Scuseria, and GI Csonka. Prescription for the design and selection of density functional approximations: More constraint satisfaction with fewer fits. *J. Chem. Phys*, 123(6), Aug 8 2005.
- [31] David C. Langreth and John P. Perdew. Theory of nonuniform electronic systems. i. analysis of the gradient approximation and a generalization that works. *Phys. Rev. B*, 21:5469–5493, Jun 1980.
- [32] David C. Langreth and M. J. Mehl. Beyond the local-density approximation in calculations of ground-state electronic properties. *Phys. Rev. B*, 28:1809–1834, Aug 1983.
- [33] John P. Perdew and Wang Yue. Accurate and simple density functional for the electronic exchange energy: Generalized gradient approximation. *Phys. Rev. B*, 33:8800–8802, Jun 1986.
- [34] John P. Perdew. Density-functional approximation for the correlation energy of the inhomogeneous electron gas. *Phys. Rev. B*, 33:8822–8824, Jun 1986.
- [35] A. Baldereschi. Mean-value point in the Brillouin zone. *Phys. Rev. B*, 7(12):5212–5215, Jun 1973.
- [36] Sverre Froyen. Brillouin-zone integration by fourier quadrature: Special points for superlattice and supercell calculations. *Phys. Rev. B*, 39(5):3168–3172, Feb 1989.
- [37] Juana Moreno and José M. Soler. Optimal meshes for integrals in real- and reciprocal-space unit cells. *Phys. Rev. B*, 45(24):13891–13898, Jun 1992.
- [38] Hendrik J. Monkhorst and James D. Pack. Special points for Brillouin-zone integrations. *Phys. Rev. B*, 13(12):5188–5192, Jun 1976.
- [39] James C. Phillips. Energy-band interpolation scheme based on a pseudopotential. *Phys. Rev.*, 112(3):685–695, Nov 1958.
- [40] James C. Phillips and Leonard Kleinman. New method for calculating wave functions in crystals and molecules. *Phys. Rev.*, 116(2):287–294, Oct 1959.

Bibliography

- [41] Philip Peter Rushton. *Towards a Non-Local Density Functional Description of Exchange and Correlation*. PhD thesis, University of Durham, 2002.
- [42] David Vanderbilt. Soft self-consistent pseudopotentials in a generalized eigenvalue formalism. *Phys. Rev. B*, 41:7892–7895, Apr 1990.
- [43] P. E. Blöchl. Projector augmented-wave method. *Phys. Rev. B*, 50(24):17953–17979, Dec 1994.
- [44] G. Kresse and D. Joubert. From ultrasoft pseudopotentials to the projector augmented-wave method. *Phys. Rev. B*, 59:1758–1775, Jan 1999.
- [45] G. Kresse and J. Hafner. Ab initio molecular dynamics for open-shell transition metals. *Phys. Rev. B*, 48(17):13115–13118, Nov 1993.
- [46] G. Kresse and J. Furthmüller. Efficient iterative schemes for ab initio total-energy calculations using a plane-wave basis set. *Phys. Rev. B*, 54(16):11169–11186, Oct 1996.
- [47] J. C. Slater. Wave functions in a periodic potential. *Phys. Rev.*, 51(10):846–851, May 1937.
- [48] O. Krogh Andersen. Linear methods in band theory. *Phys. Rev. B*, 12(8):3060–3083, Oct 1975.
- [49] U von Barth and L Hedin. A local exchange-correlation potential for the spin polarized case. i. *J. Phys. C*, 5(13):1629, 1972.
- [50] L. M. Sandratskii. Noncollinear magnetism in itinerant-electron systems: theory and applications. *Adv. Phys.*, 47(1):91 – 160, January 1998.
- [51] J. J. Sakurai. *Modern Quantum Mechanics*. Revised Edition, Addison-Wesley, revised edition edition, 1994.
- [52] Nicholas Metropolis, Arianna W. Rosenbluth, Marshall N. Rosenbluth, Augusta H. Teller, and Edward Teller. Equation of state calculations by fast computing machines. *J. Chem. Phys.*, 21(6):1087–1092, 1953.
- [53] M. E. J. Newman and G. T. Barkema. *Monte Carlo Methods in Statistical Physics*. Oxford University Press, revised edition edition, 1999.
- [54] John A. Rice. *Mathematical Statistics and Data Analysis*. Duxbury Press, 2nd edn edition, 1995.
- [55] L. D. Landau and E. M. Lifshitz. *Statistical Physics*. Butterworth-Heinemann, 3rd ed edition, 1980.

Bibliography

- [56] Georg Heimel, Lorenz Romaner, Jean-Luc Brédas, and Egbert Zojer. Interface energetics and level alignment at covalent metal-molecule junctions conjugated thiols on gold. *Phys. Rev. Lett.*, 96:196806, May 2006.
- [57] John P. Perdew and Yue Wang. Accurate and simple analytic representation of the electron-gas correlation energy. *Phys. Rev. B*, 45:13244–13249, Jun 1992.
- [58] F. D. Murnaghan. The Compressibility of Media under Extreme Pressures. *Proceedings of the National Academy of Sciences of the United States of America*, 30(9):244–247, 1944.
- [59] Neil W. Ashcroft and David N. Mermin. *Solid State Physics*. Thomson Learning, Toronto, 1 edition, January 1976.
- [60] C. Kittel. *Introduction to Solid State Physics*. John Wiley and Sons, seventh ed. edition, 1996.
- [61] K Doll and NM Harrison. Chlorine adsorption on the Cu(111) surface. *Chem. Phys. Lett.*, 317(3-5):282–289, Feb 4 2000.
- [62] O. Jepsen, D. Glötzel, and A. R. Mackintosh. Potentials, band structures, and Fermi surfaces in the noble metals. *Phys. Rev. B*, 23:2684–2696, Mar 1981.
- [63] D. L. Adams, H. B. Nielsen, and M. A. Van Hove. Quantitative analysis of low-energy-electron diffraction: Application to Pt(111). *Phys. Rev. B*, 20(12):4789–4806, Dec 1979.
- [64] S. Å. Lindgren, L. Walldén, J. Rundgren, and P. Westrin. Low-energy electron diffraction from Cu(111): Subthreshold effect and energy-dependent inner potential; surface relaxation and metric distances between spectra. *Phys. Rev. B*, 29(2):576–588, Jan 1984.
- [65] M. Methfessel, D. Hennig, and M. Scheffler. Trends of the surface relaxations, surface energies, and work functions of the 4d transition metals. *Phys. Rev. B*, 46(8):4816–4829, Aug 1992.
- [66] Th. Rodach, K.-P. Bohnen, and K.M. Ho. First principles calculations of lattice relaxation at low index surfaces of Cu. *Surf. Sci.*, 286(1-2):66 – 72, 1993.
- [67] H. M. Polatoglou, M. Methfessel, and M. Scheffler. Vacancy-formation energies at the (111) surface and in bulk Al, Cu, Ag, and Rh. *Phys. Rev. B*, 48(3):1877–1883, Jul 1993.
- [68] Peter J. Feibelman. Disagreement between experimental and theoretical metal surface relaxations. *Surf. Sci.*, 360(1-3):297 – 301, 1996.

Bibliography

- [69] S. Å. Lindgren, L. Walldén, J. Rundgren, and P. Westrin. Low-energy electron diffraction from Cu(111): Subthreshold effect and energy-dependent inner potential; surface relaxation and metric distances between spectra. *Phys. Rev. B*, 29(2):576–588, Jan 1984.
- [70] W.R. Tyson and W.A. Miller. Surface free energies of solid metals: Estimation from liquid surface tension measurements. *Surf. Sci.*, 62(1):267 – 276, 1977.
- [71] JC Boettger, JR Smith, U Birkenheuer, N Rosch, SB Trickey, JR Sabin, and SP Apell. Extracting convergent surface formation energies from slab calculations. *J. Phys.: Condens. Matter*, 10(4):893–894, Feb 2 1998.
- [72] Juarez L.F. Da Silva, Catherine Stampfl, and Matthias Scheffler. Converged properties of clean metal surfaces by all-electron first-principles calculations. *Surf. Sci.*, 600(3):703 – 715, 2006.
- [73] Maria Steslicka Sidney G. Davison. *Basic Theory of Surface States*. Clarendon Press, 1992.
- [74] William Shockley. On the surface states associated with a periodic potential. *Phys. Rev.*, 56:317–323, Aug 1939.
- [75] S. D. Kevan. Evidence for a new broadening mechanism in angle-resolved photoemission from Cu(111). *Phys. Rev. Lett.*, 50:526–529, Feb 1983.
- [76] J Koringa. On the calculation of the energy of a Bloch wave in a metal. *Physica*, 13(67):392 – 400, 1947.
- [77] W. Kohn and N. Rostoker. Solution of the Schrödinger equation in periodic lattices with an application to metallic lithium. *Phys. Rev.*, 94:1111–1120, Jun 1954.
- [78] N Memmel. Monitoring and modifying properties of metal surfaces by electronic surface states. *Surf. Sci. Rep.*, 32(3-4):93–163, 1998.
- [79] F. Reinert, G. Nicolay, S. Schmidt, D. Ehm, and S. Hüfner. Direct measurements of the L -gap surface states on the (111) face of noble metals by photoelectron spectroscopy. *Phys. Rev. B*, 63:115415, Mar 2001.
- [80] Chr. Tegenkamp. Vicinal surfaces for functional nanostructures. *J. Phys.: Condens. Matter*, 21:1013002, 2009.
- [81] N. N. Negulyaev, V. S. Stepanyuk, W. Hergert, P. Bruno, and J. Kirschner. Atomic-scale self-organization of Fe nanostripes on stepped Cu(111) surfaces: Molecular dynamics and kinetic Monte Carlo simulations. *Phy. Rev. B*, 77(8):085430, 2008.
- [82] Dietmar C. Schlöber, Laurens K. Verheij, Georg Rosenfeld, and George Comsa. Determination of step free energies from island shape fluctuations on metal surfaces. *Phys. Rev. Lett.*, 82(19):3843–3846, May 1999.

Bibliography

- [83] Roland Stumpf and Matthias Scheffler. Ab initio calculations of energies and self-diffusion on flat and stepped surfaces of Al and their implications on crystal growth. *Phys. Rev. B*, 53(8):4958–4973, Feb 1996.
- [84] V.S. Stepanyuk, W. Hergert, P. Rennert, K. Wildberger, R. Zeller, and P.H. Dederichs. Transition metal magnetic nanostructures on metal surfaces. *Surf. Sci.*, 377-379:495 – 498, 1997.
- [85] V.S. Stepanyuk, W. Hergert, K. Wildberger, S.K. Nayak, and P. Jena. Magnetic bistability of supported Mn clusters. *Surf. Sci.*, 384(1-3):L892 – L895, 1997.
- [86] T. Hoshino, W. Schweika, R. Zeller, and P.H. Dederichs. Impurity-impurity interactions in Cu, Ni, Ag, and Pd. *Phys. Rev. B*, 47:5106, 1993.
- [87] H. Hashemi, W. Hergert, and V. S. Stepanyuk. Magnetic properties of 3d transition metal chains on vicinal Cu(111) surface. *J. Magn. Magn. Mater.*, 322(9-12):1296–1299, May-Jun 2010.
- [88] A. I. Liechtenstein, M. I. Katsnelson, V. P. Antropov, and V. A. Gubanov. Local spin density functional approach to the theory of exchange interactions in ferromagnetic metals and alloys. *J. Magn. Magn. Mater.*, 67(1):65 – 74, 1987.
- [89] Guntram Fischer, Markus Däne, Arthur Ernst, Patrick Bruno, Martin Lüders, Zdzisława Szotek, Walter Temmerman, and Wolfram Hergert. Exchange coupling in transition metal monoxides: Electronic structure calculations. *Phys. Rev. B*, 80(1):014408, Jul 2009.
- [90] H. Hashemi, W. Hergert, and V. S. Stepanyuk. Magnetic states of M-Fe wires (M=Sc-Ni) on vicinal Cu(111) from first principles. *Phys. Rev. B*, 81(10), Mar 2010.
- [91] M. A. Ruderman and C. Kittel. Indirect exchange coupling of nuclear magnetic moments by conduction electrons. *Phys. Rev.*, 96(1):99, Oct 1954.
- [92] Tadao Kasuya. A theory of metallic ferro- and antiferromagnetism on Zener’s model. *Prog. Theor. Phys.*, 16(1):45–57, 1956.
- [93] Kei Yosida. Magnetic properties of Cu-Mn alloys. *Phys. Rev.*, 106(5):893–898, Jun 1957.
- [94] P. Wahl, P. Simon, L. Diekhöner, V. S. Stepanyuk, P. Bruno, M. A. Schneider, and K. Kern. Exchange interaction between single magnetic adatoms. *Phys. Rev. Lett.*, 98(5):056601, Jan 2007.
- [95] V.S. Stepanyuk, L. Niebergall, A.N. Baranov, W. Hergert, and P. Bruno. Long-range electronic interactions between adatoms on transition metal surfaces. *Comput. Mater. Sci.*, 35(3):272 – 274, 2006. Proceedings of the 4th International Conference on the Theory of Atomic and Molecular Clusters (TAMC-IV).

Bibliography

- [96] H Ohnishi, Y Kondo, and K Takayanagi. Quantized conductance through individual rows of suspended gold atoms. *Nature*, 395(6704):780–783, Oct 22 1998.
- [97] AI Yanson, GR Bollinger, HE van den Brom, N Agrait, and JM van Ruitenbeek. Formation and manipulation of a metallic wire of single gold atoms. *Nature*, 395(6704):783–785, Oct 22 1998.
- [98] P Gambardella, M Blanc, L Burgi, K Kuhnke, and K Kern. Co growth on Pt(997): from monatomic chains to monolayer completion. *Surf. Sci.*, 449(1-3):93–103, Mar 20 2000.
- [99] D. Spišák and J. Hafner. Fe nanowires on vicinal Cu surfaces: Ab initio study. *Phys. Rev. B*, 65(23):235405, May 2002.
- [100] A. Dallmeyer, C. Carbone, W. Eberhardt, C. Pampuch, O. Rader, W. Gudat, P. Gambardella, and K. Kern. Electronic states and magnetism of monatomic Co and Cu wires. *Phys. Rev. B*, 61:R5133–R5136, Feb 2000.
- [101] Claude Ederer, Matej Komelj, and Manfred Fähnle. Magnetism in systems with various dimensionalities: A comparison between Fe and Co. *Phys. Rev. B*, 68:052402, Aug 2003.
- [102] Jisang Hong and R. Q. Wu. First principles calculations of magnetic anisotropy energy of Co monatomic wires. *Phys. Rev. B*, 67:020406, Jan 2003.
- [103] Matej Komelj, Claude Ederer, James W. Davenport, and Manfred Fähnle. From the bulk to monatomic wires: an *ab initio* study of magnetism in Co systems with various dimensionality. *Phys. Rev. B*, 66:140407, Oct 2002.
- [104] Filipe J. Ribeiro and Marvin L. Cohen. *Ab initio* pseudopotential calculations of infinite monatomic chains of Au, Al, Ag, Pd, Rh, and Ru. *Phys. Rev. B*, 68:035423, Jul 2003.
- [105] Tashi Nautiyal, Suk Joo Youn, and Kwang S. Kim. Effect of dimensionality on the electronic structure of Cu, Ag, and Au. *Phys. Rev. B*, 68:033407, Jul 2003.
- [106] Sune R. Bahn and Karsten W. Jacobsen. Chain formation of metal atoms. *Phys. Rev. Lett.*, 87:266101, Dec 2001.
- [107] A. Delin and E. Tosatti. Magnetic phenomena in 5d transition metal nanowires. *Phys. Rev. B*, 68:144434, Oct 2003.
- [108] Prasenjit Sen, S. Ciraci, A. Buldum, and Inder P. Batra. Structure of aluminum atomic chains. *Phys. Rev. B*, 64:195420, Oct 2001.
- [109] H. Hashemi, G. Fischer, W. Hergert, and V. S. Stepanyuk. Magnetic properties of 3d transition metal wires on vicinal Cu(111) surfaces at finite temperature. *J. Appl. Phys.*, 107(9), May 1 2010.

Bibliography

- [110] P. A. Ignatiev, N. N. Negulyaev, L. Niebergall, H. Hashemi, W. Hergert, and V. S. Stepanyuk. Electronic structure and magnetism of monatomic one-dimensional metal nanostructures on metal surfaces. *Phys. Status Solidi B*, 247(10):2537–2549, Oct 2010.
- [111] J. C. Tung and G. Y. Guo. Systematic *ab initio* study of the magnetic and electronic properties of all 3d transition metal linear and zigzag nanowires. *Phys. Rev. B*, 76:094413, Sep 2007.
- [112] J. Hauschild, H. J. Elmers, and U. Gradmann. Dipolar superferromagnetism in monolayer nanostripes of Fe(110) on vicinal W(110) surfaces. *Phys. Rev. B*, 57:R677–R680, Jan 1998.
- [113] D. Tian, F. Jona, and P. M. Marcus. Structure of ultrathin films of Fe on Cu(111) and Cu(110). *Phys. Rev. B*, 45:11216–11221, May 1992.
- [114] M. Methfessel and A. T. Paxton. High-precision sampling for Brillouin-zone integration in metals. *Phys. Rev. B*, 40(6):3616–3621, Aug 1989.
- [115] Blaha P. Schwarz K. Madsen G. K. H. Kvasnicka D. and Luitz J. An augmented plane wave plus local orbitals program for calculating crystal properties. *WIEN2k*, 2001.
- [116] G. Y. Guo. Spin- and orbital-polarized multiple-scattering theory of magneto-x-ray effects in Fe, Co, and Ni. *Phys. Rev. B*, 55:11619–11628, May 1997.
- [117] G Y Guo, W M Temmerman, and H Ebert. First-principles determination of the magnetization direction of Fe monolayer in noble metals. *J. Phys. Condens. Matter*, 3(42):8205, 1991.
- [118] Y. Mokrousov, G. Bihlmayer, S. Heinze, and S. Blügel. Giant magnetocrystalline anisotropies of 4d transition-metal monowires. *Phys. Rev. Lett.*, 96:147201, Apr 2006.
- [119] A. Delin, E. Tosatti, and Ruben Weht. Delin, Tosatti, and Weht reply:. *Phys. Rev. Lett.*, 96:079702, Feb 2006.
- [120] Simone S. Alexandre, Maurizio Mattesini, José M. Soler, and Félix Yndurain. Comment on “magnetism in atomic-size palladium contacts and nanowires”. *Phys. Rev. Lett.*, 96:079701, Feb 2006.
- [121] G.Y. Guo. Strain, interdiffusion, magnetism and magnetic anisotropy in Cu/Ni/Cu (001) sandwiches. *J. Magn. Magn. Mater.*, 176(23):97 – 110, 1997.
- [122] J. C. Tung and G. Y. Guo. Magnetic moment and magnetic anisotropy of linear and zigzag 4d and 5d transition metal nanowires: First-principles calculations. *Phys. Rev. B*, 81:094422, Mar 2010.

- [123] B. Nonas, K. Wildberger, R. Zeller, and P. H. Dederichs. Energetics of 3d impurities on the (001) surface of iron. *Phys. Rev. Lett.*, 80:4574–4577, May 1998.
- [124] J.C. Tung and G.Y. Guo. An ab initio study of the magnetic and electronic properties of Fe, Co, and Ni nanowires on Cu(001) surface. *Comput. Phys. Commun.*, 182(1):84 – 86, 2011. Computer Physics Communications Special Edition for Conference on Computational Physics Kaohsiung, Taiwan, Dec 15-19, 2009.

Acknowledgements

I would like to express my gratitude to my supervisor Prof. Dr. Wolfram Hergert for his guidance and advice. His deep knowledge in Physics and numerous helpful discussions have been very motivating. In fact, without his support this thesis could not be completed. I was so fortunate to have him as my supervisor.

I would like to appreciate Dr. Valeriy Stepanyuk for his constructive criticism I received during our discussions.

I would like to greatly acknowledge Prof. Dr. Jürgen Kirschner and his coworkers for the performed experiments on nanowires.

I am very thankful for the support by the cluster of excellence Nanostructured Materials of the state Saxony-Anhalt and the International Max Planck Research School for Science and Technology of Nanostructures.

I would like to thank Dr. Nikolay Negulyaev and Dr. Pavel Ignatiev for fruitful discussions.

I want to thank all Prof. Hergert's group (including current and former) members for their support over the years. Many warm and kind thanks are going to Dr. Guntram Fischer, Dr. Waheed Adeagbo, Dr. Christian Matyssek, Dr. Oleksiy Kiriyyenko, Dr. Sanjeev Kumar Nayak, Dr. Markus Däne and Martin Hoffmann.

I gratefully acknowledge all the colleagues from the Martin Luther University and MPI Halle: scientists, technicians and staff of administration, for the stimulating atmosphere.

I would also like to express my thanks to my parents and my daughter.

Finally, I thank my dear wife for her support and love.

Halle, 18.6.2014

Hossein Hashemi

Curriculum Vitae

Personal details

- Name: Hossein Hashemi
- Date of Birth: 31.08.1976
- Place of Birth: Arak, Iran

Education and Work Experience

- 1998-2002: Bachelor of Science (Physics), Shahid Rajaei University, Tehran, Iran
- 2002-2005: Master of Science (Physics), K.N.Toosi University of Technology, Tehran, Iran
- 2007-2011: Research fellow, Martin-Luther-University, Halle, Germany
- 2007-2011: PhD student, International Max Planck Research School (IMPRS), Halle, Germany
- 2011-2014: Visiting Research Associate, University of Michigan, Ann Arbor, USA

Publications

- H1 D. Lee, X. Ma, E. J. Jeong, H. Hashemi, J. Kieffer, and J. Kim. Photophysical study of organic phosphorescence depending on extended conjugation length. Submitted to *J. Phys. Chem. C*
- H2 E. Morris, D. Bilby, M. E. Sykes, H. Hashemi, M. J. Waters, J. Kieffer, J. Kim, M. Shtein. Effect of axial halogen substitution on the performance of subphthalocyanine based organic photovoltaic cells. *Org. Electron.*, **15**(12):3660–3665, Dec 2014
- H3 M. Bahrami, H. Hashemi, X. Ma, J. Kieffer, R. Laine. Why do the $[PhSiO_{1.5}]_{8,10,12}$ cages self-brominate primarily in the ortho position? Modeling reveals a strong cage influence on the mechanism., (*Communication*) *Phys. Chem. Chem. Phys.*, **16**(47):25760-25764, Oct 2014
- H4 Bong-Gi Kim, Xiao Ma, Chelsea Chen, Yutaka Ie, Elizabeth W. Coir, Hossein Hashemi, Yoshio Aso, Peter F. Green, John Kieffer, and Jinsang Kim. Energy Level Modulation of HOMO, LUMO, and Band-Gap in Conjugated Polymers for Organic Photovoltaic Applications. *Adv. Funct. Mater.*, **23**(4):439–445, Jan 28 2013
- H5 P. A. Ignatiev, N. N. Negulyaev, L. Niebergall, H. Hashemi, W. Hergert, and V. S. Stepanyuk. Electronic structure and magnetism of monatomic one-dimensional metal nanostructures on metal surfaces. *Phys. Status Solidi (b)*, **247**(10):2537–2549, Oct 2010
- H6 H. Hashemi, G. Fischer, W. Hergert, and V. S. Stepanyuk. Magnetic properties of 3d transition metal wires on vicinal Cu(111) surfaces at finite temperature. *J. Appl. Phys.*, **107**(9):09E311, May 2010
- H7 H. Hashemi, W. Hergert, and V. S. Stepanyuk. Magnetic states of M-Fe wires (M=Sc-Ni) on vicinal Cu(111) from first principles. *Phys. Rev. B*, **81**(10):104418, Mar 2010
- H8 H. Hashemi, W. Hergert, and V. S. Stepanyuk. Magnetic properties of 3d transition metal chains on vicinal Cu(111) surface. *J. Magn. Magn. Mater.*, **322**(9-12):1296–1299, May-Jun 2010
- H9 M. Heidari Saani, H. Hashemi, A. Ranjbar, M. A. Vesaghi, and A. Shafiekhani. Explanation of atomic displacement around lattice vacancies in diamond based on electron delocalization. *Eur. Phys. J. B*, **65**(2):219–223, Sep 2008
- H10 MH Saani, K Esfarjani, H Hashemi, MA Vesaghi, and AR Basiri. Relationship between lattice relaxation and electron delocalization in diamond vacancies. *Physica B-Condens. Matter.*, **376**:324–326, Apr 2006

H11 MH Saani, MA Vesaghi, K Esfarjani, TG Elahi, M Sayari, H Hashemi, and N Gorjizadeh. Lattice relaxation in many-electron states of the diamond vacancy. *Phys. Rev. B*, **71**(3):035202, Jan 2005

Erklärung

Hiermit erkläre ich, dass ich diese Arbeit selbständig und ohne fremde Hilfe verfaßt, andere als die von mir angegebenen Quellen und Hilfsmittel nicht benutzt und die den benutzten Werken wörtlich oder inhaltlich entnommenen Stellen als solche kenntlich gemacht habe.

Eine Anmeldung der Promotionsabsicht habe ich an keiner anderen Fakultät einer Universität oder Hochschule beantragt.

Halle, 18.6.2014

Hossein Hashemi